

# **Fatigue Failure Analysis of the Bimetallic Work Roll in Four-High Rolling Mill**

**4 段式圧延機用複合ワークロールにおける圧延応力解析と疲労強度  
評価**

**Mohd Radzi BIN ARIDI**

**Supervisor: Prof. Nao-Aki Noda**

**Thesis Submitted to the Graduate School of Engineering, Kyushu Institute  
of Technology, in Fulfilment of the Requirements for the degree of Doctor of  
Philosophy**

**September 2021**

## **Abstract**

In hot rolling of steel, high-speed bimetallic work rolls consisting of high-carbon high-speed steel (HSS) for the outer layer and ductile casting iron (DCI) for the inner layer are widely used. To extend the life of the roll, as the roll usage conditions become stricter, such as high-load rolling due to the increased strength of the rolled material, measures against fatigue fracture starting from the inside of the roll such as the HSS/DCI boundary and inner layer are becoming important. Therefore, in this study, the rolling stress during the use of the bimetallic work roll in a 4-high rolling mill is clarified. In particular, based on the fatigue fracture cases that occurred inside the work roll, the risk of fatigue fracture is considered by focusing on some dangerous areas. The risk of fatigue failure in consideration of the residual stress introduced into the rolls is also considered. This paper consists of 6 chapters and is organized as follows.

Chapter 1 introduced the bimetallic work roll used in the 4-high rolling mill. Previous research on the development of HSS bimetallic work rolls by improving wear and surface resistance is explained. The manufacturing method, residual stress, and past roll breakage accidents are also summarized. Then, the necessity to clarify the rolling stress when this roll is used in a 4-high rolling mill is explained and the evaluation of the fatigue risk in consideration of the residual stress is also studied.

In Chapter 2, an appropriate quenching process is discussed to improve the bimetallic roll quality and increase their strength reliability since the heat treatment can control the residual stress. The data of material properties required for the analysis are clarified, and it is shown that the compressive stress is generated on the roll surface and tensile stress is generated on the roll center after quenching. On the other hand, the residual stress of non-uniform heating quenching is also discussed, in which the rolls are heated uniformly and then rapidly cooled. As a result, the maximum tensile stress of non-uniform heat quenching can be reduced by 20% to 30% from the maximum tensile stress of uniform heat quenching. In addition, the effects of roll diameter and area ratio on residual stress

have been clarified.

In Chapter 3, the effect of additional heat treatment called tempering after quenching is explained to reduce internal stress. Similar thermo-elasto-plastic finite element simulation is performed in consideration of creep, and the residual stress distribution after the two tempering processes is compared for both uniform heating quenching and non-uniform heating quenching. Reduction of tensile residual stress at the center of the inner layer can be clarified by tempering after uniform heating quenching and non-uniform heating quenching. In this tempering process, the residual stress inside the roll is reduced by stress relaxation due to the creep effect.

Chapter 4 focuses on clarifying the rolling stress distribution that fluctuates in response to roll rotation inside the bimetallic work rolls, which has not been studied so far. Normally, bimetallic work rolls are used for rolling by introducing appropriate residual stress by pre-heating, quenching, and tempering heat treatment, but it is considered that the heat treatment conditions differ depending on each roll manufacturer. Therefore, in this chapter, rolling analysis with no residual stress is considered to clarify the mechanical stress. The relationship between the stress amplitude and the fatigue limit under the compressive mean stress, which has not been studied in fatigue so far, is studied and a new fatigue limit line for the compressive stress field as a durability diagram is proposed. Then, concerning past roll fatigue damage cases, fatigue fracture is discussed focusing on three dangerous points in the work roll. Since the maximum stress amplitude is caused by the rolled steel, it can be concluded that the most dangerous point is at the center of the roll axis inside the HSS / DCI boundary.

In Chapter 5, in order to evaluate the fatigue fracture risk according to the actual roll, the rolling analysis is generated under the initial condition of having roll residual stress. The risk of internal fatigue fracture is discussed using a similar approach in Chapter 4. In addition, since the consecutive FEM analysis for each roll rotation requires a great deal of time and effort, it is clarified that the accuracy when the residual stress and rolling stress are simply superposed as a simple evaluation method. As a result, it is shown that

---

the superposition method can evaluate the risk of fatigue fracture more safely than the consecutive FEM analysis. It is also shown that when the defect size at the center point of the roll is 5 mm or more, there is a risk of fatigue fracture at the center.

Chapter 6 summarizes the main conclusions of this study.

---

# List of Contents

<b>1</b>	<b>Introduction</b>	<b>1</b>
1.1	Work roll development . . . . .	1
1.2	Bimetallic work roll manufacturing process . . . . .	2
1.3	Roll failures in previous study . . . . .	4
1.3.1	Roll failures pattern . . . . .	4
1.3.2	Residual stress inside the work roll . . . . .	6
1.4	Motivation and Objectives . . . . .	7
<b>2</b>	<b>Residual stress after the heating quenching treatment of the bimetallic work roll</b>	<b>10</b>
2.1	Introduction . . . . .	10
2.2	Mechanical properties of the bimetallic work roll . . . . .	10
2.3	Analysis method . . . . .	13
2.4	Influence on Residual Stress by Non-Uniform Heating . . . . .	16
2.5	Comparison between uniform and non-uniform heating quenching treatment	17
2.5.1	Stress generation mechanism of uniform and non-uniform heating quenching . . . . .	17
2.5.2	Effect of diameter on uniform and non-uniform heating quenching .	20
2.5.3	Effect of area ratio on uniform and non-uniform heating quenching	21
2.6	Conclusion for Chapter 2 . . . . .	21
<b>3</b>	<b>Residual stress after the heating, quenching, and tempering treatment of the bimetallic work roll</b>	<b>24</b>
3.1	Introduction . . . . .	24
3.2	Analysis method . . . . .	24
3.3	Effect of creep behaviour on residual stress . . . . .	24
3.4	Residual stress distribution . . . . .	27

---

**List of Contents**

---

3.5	Stress generation mechanism during tempering . . . . .	28
3.6	Conclusion for Chapter 3 . . . . .	29
<b>4</b>	<b>Rolling stress and fatigue failure during rolling analysis</b>	<b>32</b>
4.1	Introduction . . . . .	32
4.2	Problem background . . . . .	32
4.3	FEM modelling and fundamental dimension and condition of the work roll and backup roll . . . . .	34
4.4	Stress variation in the work roll during a roll rotation . . . . .	37
4.4.1	Surface stress variation in the $\theta$ -direction the work roll . . . . .	38
4.4.2	Internal stress variation in the z-direction of the work roll . . . . .	40
4.4.3	Stress variation $\sigma_r$ in the vicinity of HSS/DCI boundary at $\theta = \pm 90^\circ$ of the work roll . . . . .	42
4.5	Effect of chamfer geometry in backup roll and effect of wear profile in work roll . . . . .	45
4.5.1	Effect of chamfer geometry in backup roll on the surface shear stress	45
4.5.2	Effect of wear profile in work roll on the line force $p_B(z)$ . . . . .	47
4.6	Fatigue risk evaluation of rolls assuming actual rolling . . . . .	51
4.6.1	Analysis of roll' s internal stress . . . . .	52
4.7	Fatigue damage under repeated compressive stress . . . . .	55
4.8	Stress amplitude vs mean stress diagram for compressive mean stress . . .	57
4.9	Conclusion for Chapter 4 . . . . .	59
<b>5</b>	<b>Actual stress and fatigue failure during consecutive rolling analysis</b>	<b>62</b>
5.1	Introduction . . . . .	62
5.2	FEM modelling and fundamental dimension and condition of the work roll and backup roll . . . . .	62
5.3	Residual stress as the initial condition to the rolling stress analysis . . . .	67

---

**List of Figures**

5.4	Rolling stress generated in the bimetallic work roll obtained by the consecutive FEM analysis . . . . .	69
5.4.1	Rolling stress variation due to the contact of the rolled steel . . . .	70
5.4.2	Rolling stress variation due to the contact of the backup roll . . . .	71
5.4.3	Rolling stress variation at the roll center . . . . .	72
5.5	Fatigue risk evaluation for three critical points . . . . .	73
5.6	Rolling stress estimation by superposing the residual stress and the rolling stress . . . . .	77
5.7	Conclusion . . . . .	79
<b>6</b>	<b>Main Conclusion</b>	<b>80</b>
6.1	Conclusion for present study . . . . .	80
6.2	Future work . . . . .	84
	<b>Acknowledgment</b>	<b>85</b>
	<b>References</b>	<b>86</b>
<b>A</b>	<b>Appendix</b>	<b>93</b>
A.1	Effect of material data on the residual stress . . . . .	93
A.2	Stress reduction effect due to the transformation effect . . . . .	96
A.3	Effect of Manufacturing Process on Residual Stress in Bimetallic Solid Roll and Bimetallic Sleeve Roll . . . . .	97
<b>B</b>	<b>List of publication</b>	<b>99</b>

**List of Figures**

(1–1)	(a) Hot strip mill finishing train; (b) Four-High rolling mill model . . . .	1
(1–2)	Conventional centrifugal casting method . . . . .	2

---

**List of Figures**

---

(1–3) New continuous pouring method . . . . .	3
(1–4) A rotational ESR bimetallic method . . . . .	4
(1–5) Schematic pattern of failure in a roll . . . . .	5
(1–6) Relation between breakage pattern and its source . . . . .	5
(1–7) Failure at HSS/DCI boundary in bimetallic work roll . . . . .	8
(2–1) Model of the bimetallic roll (mm) . . . . .	11
(2–2) View of microstructure for a HSS roll with a DCI core . . . . .	12
(2–3) Material properties under various temperatures obtained experimentally to clarify quenching analysis . . . . .	13
(2–4) Finite element model for bimetallic roll . . . . .	14
(2–5) Work roll surface temperature during pre-heating and quenching . . . . .	15
(2–6) Comparison of residual stress distribution, $\sigma_z$ for both heating treatments	17
(2–7) Uniform heating process and corresponding stress $\sigma_z$ . . . . .	18
(2–8) Non-uniform heating process and corresponding stress $\sigma_z$ . . . . .	19
(2–9) Residual stress distribution $\sigma_z$ for different diameters . . . . .	21
(2–10) Residual stress distribution $\sigma_z$ for different area ratios . . . . .	22
(3–1) Work roll surface temperature during pre-heating, quenching and tempering	25
(3–2) Specimen of creep test and stress relaxation test . . . . .	26
(3–3) Effect of tempering after uniform heating, quenching and tempering . . .	27
(3–4) Effect of tempering after non-uniform heating, quenching and tempering	28
(3–5) Histories of temperature and stress $\sigma_z$ during tempering process after uniform heating . . . . .	30
(3–6) Histories of temperature and stress $\sigma_z$ during tempering process after non-uniform heating . . . . .	30
(4–1) Failure at HSS/DCI boundary in bimetallic work roll . . . . .	33
(4–2) Three-dimensional FEM model of four-high rolling mill . . . . .	35
(4–3) Stress-strain relations for HSS and DCI . . . . .	36
(4–4) FEM mesh for backup roll and work roll . . . . .	37



---

**List of Figures**


---

(4–5) Definition of $p_B(z)$ and $p_S^{ave}$ due to contact between backup roll and work roll . . . . .	38
(4–6) Stress distribution $\sigma_r$ along the roll surface in the $\theta$ -direction at $z = 0$ .	39
(4–7) Stress distribution $\sigma_\theta$ along the roll surface in the $\theta$ -direction at $z = 0$ .	39
(4–8) Stress distribution $\sigma_z$ along the roll surface in the $\theta$ -direction at $z = 0$ .	40
(4–9) Surface and boundary layers in the work roll . . . . .	40
(4–10) Stress $\sigma_r$ at $r = 330$ mm and the HSS/DCI boundary $r = 270$ mm in the $z$ -direction . . . . .	42
(4–11) Stress $\sigma_\theta$ at $r = 330$ mm and the HSS/DCI boundary $r = 270$ mm in the $z$ -direction . . . . .	43
(4–12) Stress $\sigma_z$ at $r = 330$ mm and the HSS/DCI boundary $r = 270$ mm in the $z$ -direction . . . . .	43
(4–13) Stress $\sigma_r$ for the contact region between work roll and backup roll . . . .	44
(4–14) Stress $\sigma_r$ for the contact region between work roll and rolled steel . . . .	45
(4–15) Chamfer geometry at the edge of the backup roll when chamfer length $l_c = 30, 60, 90,$ and $120$ mm . . . . .	46
(4–16) Surface shear stress to determine the chamfer geometry on backup roll in Figure (4–15) when the chamfer lengths $l_c = 30, 60, 90,$ and $120$ mm .	47
(4–17) Crown profile with height $h_c$ at the backup roll and wear profile with depth $h_w$ at the work roll . . . . .	48
(4–18) Crown profile with fixed $h_c = 0.5$ mm at the backup roll and wear profile with depth $h_w = 0 \sim 0.3$ mm at the work roll . . . . .	49
(4–19) Line force $p_B(z)$ from backup roll when $h_c$ changes . . . . .	50
(4–20) Maximum line force $p_B(z)$ applied from backup roll vs. the position of the maximum line force . . . . .	51
(4–21) Critical position caused by the variation of $\sigma_r$ in the work roll . . . . .	52
(4–22) Rolling stress $\sigma_r$ at $\theta = 0^\circ$ , $\theta = 90^\circ$ and $\theta = -90^\circ$ along $z$ -direction on the boundary $r = 270$ mm of the work roll . . . . .	53

---

**List of Figures**


---

(4–23) Stress distribution $\sigma_r$ at the boundary along $\theta$ -direction . . . . .	54
(4–24) Rolling stress $\sigma_r$ at $\theta = 0^\circ$ and $\theta = 90^\circ$ along $z$ -direction at the work roll center $r = 0$ . . . . .	55
(4–25) Illustration of three critical points denoted by $B_0^{270}  _{\text{Rolled steel}}, B_{750}^{270}  _{\text{Backup roll}}$ and $C_0^0$ . . . . .	55
(4–26) Three types of compressive alternative loading where the mean stress $\sigma_m < 0$ . . . . .	56
(4–27) Fatigue limit diagram to evaluate three critical points . . . . .	59
(5–1) 3D FEM model of four-high rolling mill and the roll dimensions used for the consecutive FEM analysis . . . . .	63
(5–2) Definition of $p_B(z)$ and $p_S^{ave}$ due to contact between backup roll and work roll . . . . .	64
(5–3) Crown profile with fixed $h_c = 0.5$ mm at the backup roll and wear profile with depth $h_w = 0 \sim 0.3$ mm at the work roll . . . . .	65
(5–4) Stress-strain relations for HSS and DCI . . . . .	66
(5–5) FEM mesh for backup roll and work roll . . . . .	67
(5–6) Heating, quenching, and tempering treatment of the bimetallic work roll . . . . .	68
(5–7) The generated residual stresses $\sigma_r, \sigma_\theta$ and $\sigma_z$ at the boundary $r = 270$ mm after tempering . . . . .	69
(5–8) Failure at HSS/DCI boundary in bimetallic work roll . . . . .	69
(5–9) Critical position caused by the variation of $\sigma_r$ in the work roll . . . . .	70
(5–10) Variation of the stress distribution $\sigma_r$ at the boundary $r = 270$ mm due to the contact of the rolled steel from $\theta = -90^\circ$ . . . . .	71
(5–11) Variation of the stress distribution $\sigma_r$ at the boundary $r = 270$ mm due to the contact of the backup roll from $\theta = 90^\circ$ . . . . .	72
(5–12) Variation of the stress distribution $\sigma_r$ at the roll center at $r = 0$ due to the contact of the rolled steel and the backup roll . . . . .	73

---

## List of Tables

---

(5–13) Illustration of three critical points denoted by $B_0^{270}$   <i>Rolled steel</i> , $B_{750}^{270}$   <i>Backup roll</i> and $C_0^0$ where fatigue risk should be evaluated based on the analysis and experience . . . . .	74
(5–14) Stress amplitude versus mean stress diagram to evaluate the fatigue fail- ure at three critical points . . . . .	75
(5–15) Fatigue limit at point $C_0^0$ when the spheroidal defect diameter $2a =$ 0,5000, 10000 $\mu\text{m}$ is assumed through $\sqrt{area} = \sqrt{\pi a^2}$ . . . . .	76
(5–16) Comparison between two different methods of the rolling stress . . . . .	77
(5–17) Stress amplitude versus mean stress diagram to evaluate the fatigue fail- ure at three critical points based on consecutive FEM analysis and su- perposition method . . . . .	78
(A–1) Material properties under various temperatures obtained experimentally to clarify quenching analysis . . . . .	93
(A–2) Results of residual stress based on Figure (3–3) . . . . .	94
(A–3) Results of residual stress based on the corrected material data . . . . .	94
(A–4) Results of residual stress based on Figure (3–4) . . . . .	95
(A–5) Results of residual stress based on the corrected material data . . . . .	95
(A–6) Effect of transformation during tempering process after uniform heating quenching . . . . .	96
(A–7) Bimetallic sleeve roll having shrink-fitted shaft manufactured by solid heat treatment and sleeve heat treatment . . . . .	98

## List of Tables

(1-1) Chemical composition of new bimetallic roll and conventional roll (mass,%)	3
(2-1) Chemical composition of the work roll(mass,%) . . . . .	11
(2-1) cont. . . . .	12
(2-2) Mechanical properties of the shell and core at room temperature . . . . .	12

---

**List of Tables**

---

(4-1)	Rolling size and condition (Base value) . . . . .	35
(4-2)	Mechanical properties of the shell and core at room temperature . . . . .	36
(4-4)	Fundamental roll profile and rolling force considered in Section 4.4 . . . . .	37
(4-5)	General roll profile and rolling force considered in Section 4.5 . . . . .	46
(4-6)	Standard roll profile and rolling force considered in Section 4.6 . . . . .	51
(4-7)	Mean stress, stress amplitude and safety factor evaluation at $B_0^{270}$ , $B_{750}^{270}$ and $C_0^0$ . . . . .	60
(5-1)	Rolling size and condition (Base value) . . . . .	63
(5-2)	Mechanical properties of the shell and core at room temperature . . . . .	66
(5-4)	Maximum stress, minimum stress, mean stress, and stress amplitude at three critical points . . . . .	74
(5-5)	Safety factor defined as $SF = \overline{OB'}/\overline{OB}$ for three critical points by ap- plying the consecutive FEM analysis . . . . .	74
(5-6)	Safety factor defined as $SF = \overline{OB'}/\overline{OB}$ at center point $C_0^0$ when the spheroidal defect diameter $2a = 0,5000, 10000 \mu\text{m}$ is assumed through $\sqrt{area} = \sqrt{\pi a^2}$ . . . . .	76
(5-7)	Comparison of safety factor for both methods in Figure (5–16) at three critical points . . . . .	78
(A-1)	Stress reduction in tempering . . . . .	97

**Nomenclature**

HSS	High speed steel
DCI	Ductile casting iron
$D$	Outer diameter of work roll in 2D
$d$	Inner diameter of work roll in 2D
$D_W$	Diameter of work roll
$D_B$	Diameter of backup roll
$r$	Radius
$L$	Roll length
$W$	Rolled steel width
$H_s$	Shore hardness
$T_{Start}$	Quenching starting temperature
$T_{Heat}$	Non uniform pre heating starting temperature
$T_{Q,Keep}$	Keeping temperature during quenching
$T_{Q,Finish}$	Quenching ending temperature
$T_{T,Keep}$	Keeping temperature during tempering
$T_{T,Finish}$	Tempering ending temperature
$T_{Austenite}$	Austenitization temperature
$T_{Pearlite}$	Pearlitization temperature
$T_{Bainite}$	Bainitization temperature
$\varepsilon_c$	Transient strain for creep equation
$\sigma_r$	Radial stress
$\sigma_\theta$	Tangential stress
$\sigma_z$	Axial stress
$\sigma_m$	Mean stress
$\sigma_a$	Stress amplitude

### Nomenclature

$\sigma_B$	Ultimate tensile strength
$\sigma_{w0}$	Material ultimate strength
$\theta_1$	Angle on $\theta$ -direction of contact between backup roll and work roll
$z_1$	Axial position on $z$ -direction
$\tau_{rz}$	Shear stress
$l_a$	Length of curved wear on the work roll
$l_b$	Length of curved crown on the backup roll
$l_c$	Length of chamfer for backup roll
$h_c$	Crown profile on the backup roll
$h_w$	Wear profile on the work roll
$P$	Rolling force
$P_{total}$	Standard fixed value of rolling force
$P/P_{total}$	Rolling force ratio
$p_B^{ave}$	Average force from backup roll contact direction
$p_B(z)$	Line force equation from backup roll side
$p_S^{ave}$	Constant line force from rolled steel side
$B_0^{270}$	Evaluation point in the work roll when $r = 270$ mm and $z = 0$ mm
$B_{750}^{270}$	Evaluation point in the work roll when $r = 270$ mm and $z = 750$ mm
$C_0^0$	Evaluation point in the work roll when $r = 0$ mm and $z = 0$ mm
$B_{0\sim 900}^{270}$	Evaluation point in the work roll when $r = 750$ mm and $0 \leq z \leq 900$ mm
SF	Safety factor

# 1 Introduction

## 1.1 Work roll development

Hot rolling processes are more tonnage than any other manufacturing process in metalworking. The demands are not only for the high quality of metal sheet but also high productivity, energy-saving, and cost-effective operation. Hot strip mill finishing train for the metal forming process can be described in Figure (1–1)a [1]. The metal/steel stock is passed through the roughing stand to reduced the desired thickness. Among a typical seven-stand hot strip finishing mill in steel industry, this study considers No.4 finishing stand where the roll is used under the most severe conditions causing relatively larger wear appears and fatigue failure may happen. Figure (1–1)b shows the layout of a 4-high rolling mill for the rolling process. The work roll is subjected to the contact between the backup roll and the rolled steel. Therefore, such kind of severe condition of the cyclic sequence of heating and cooling occurs during the rolling process [2].

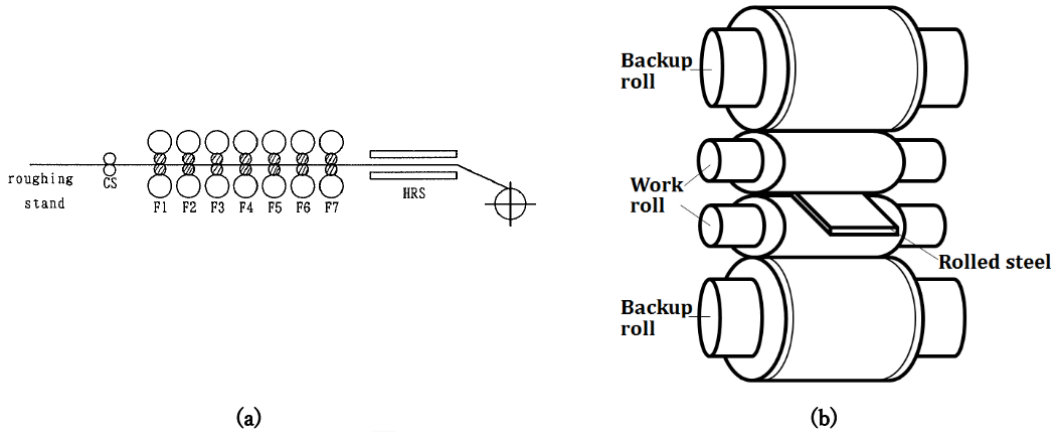


Figure (1–1): (a) Hot strip mill finishing train; (b) Four-High rolling mill model

Requirement for higher wear resistance and lower damage of rolls in the roll accident have been increasing more and more. Many studies have been conducted to improve wear resistance, surface resistance, and heat crack resistance of the work rolls [3] [4] [5]. Fracture toughness is required at the roll center of the work roll while wear resistance and

## 1. Introduction

---

heat resistance are required at the roll surface [6]. Since the conventional single material roll do not seem satisfy many properties at the same time, it is necessary to develop a new type composite roll [7] [8].

To replace the single conventional roll, a new composite or bimetallic work roll consists of high speed steel at the outer layer and cast iron at the inner layer is manufactured [9]. The manufacturing process will be discussed in the next section. Compared with conventional rolls, HSS roll has a high wear resistance and surface roughening resistance, and the core layer consisted of cast iron or forged steel with a high hard toughness [10].

### 1.2 Bimetallic work roll manufacturing process

The conventional manufacturing method of the bimetallic roll is the centrifugal casting method [11] shown in Figure (1–2). For the work roll, indefinite chilled iron roll or high chromium iron roll are used for the material. However, when indefinite chilled iron roll and high chromium iron roll are used as hot strip mill finishing train work roll, rolls are changed due to the increasing of wear and roughness of roll surface with short hours frequently. Therefore, the new bimetallic roll is composed of high-carbon speed steel outer shell and forged steel core. This new bimetallic roll is produced with the continuous casting for cladding method, pouring the molten metal of outer shell around the strong forged steel core continuously as shown in Figure (1–3).

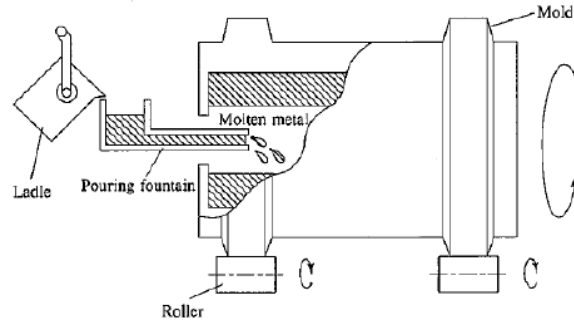


Figure (1–2): Conventional centrifugal casting method



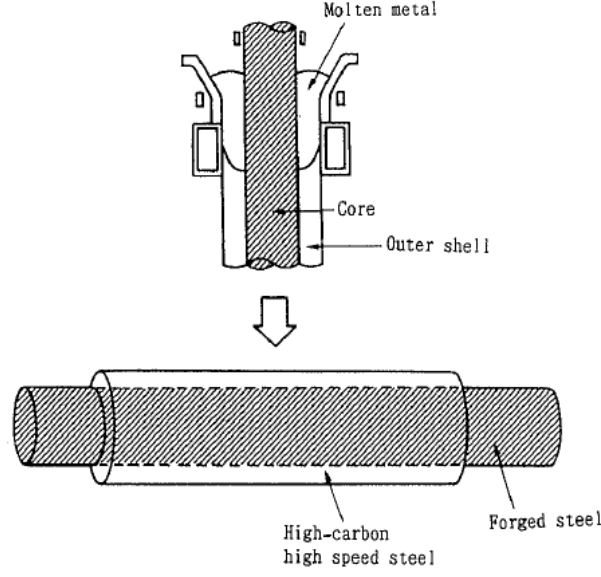


Figure (1–3): New continuous pouring method [1]

Table (1-1) shows the chemical composition of the high-carbon speed steel roll, compared with the indefinite chilled iron roll and high chromium iron roll [1].

Table (1-1): Chemical composition of new bimetallic roll and conventional roll (mass,%)

Composition	C	Cr	Mo	W	V
High-carbon speed steel roll	1.5/3.5	2~7	$\leq 9$	$\leq 20$	3~15
Indefinite chilled iron roll	2.5/3.5	$\leq 2.5$	$\leq 1$	-	-
High chromium iron roll	1.0/3.0	8/25	$\leq 3$	-	$\leq 3$

On the other hand, a rotational electroslag remelting (ESR) bimetallic method is also developed to achieve remarkable high roll performance [7]. Figure (1–4) shows the ESR method where it has high potential to process high alloy steel with good metallurgical quality.

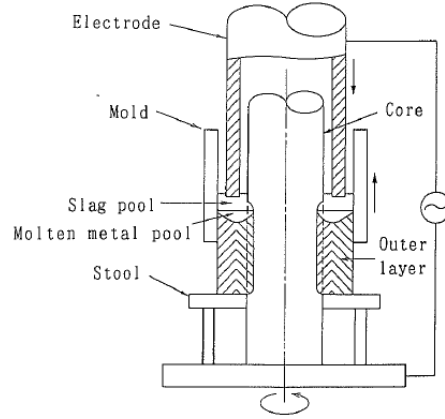


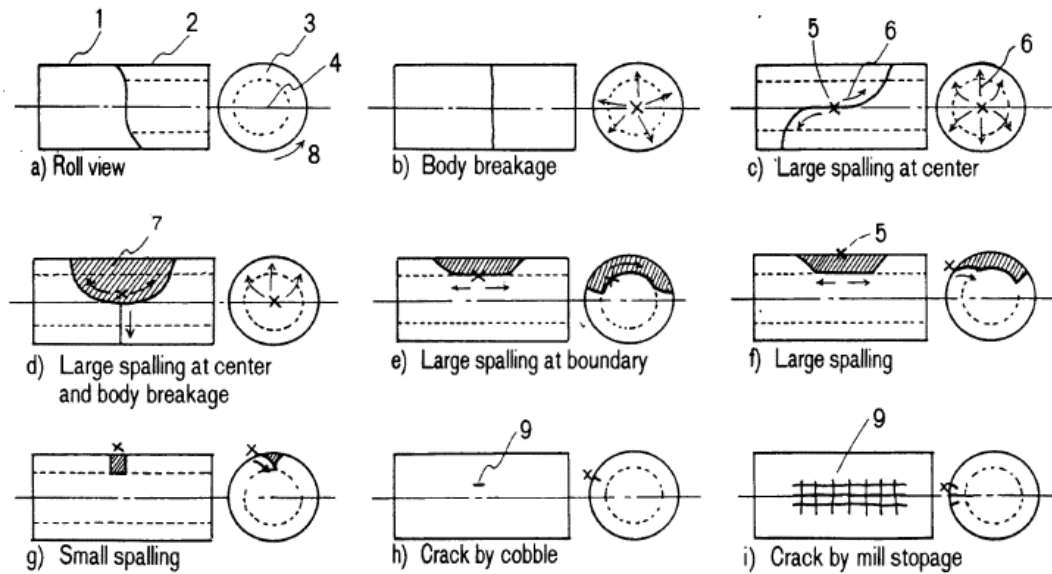
Figure (1–4): A rotational ESR bimetallic method [6]

### 1.3 Roll failures in previous study

#### 1.3.1 Roll failures pattern

Figure (1–5) shows the failure illustration in a roll [12]. Various accident patterns that occur in a roll body are shown in this figure. Figure (1–6) shows the relationship between each fracture accident, roll properties, and rolling conditions [13]. Of the fracture accidents shown in Figure (1–5), the fracture accident starting from the inside of the roll has operational abnormalities such as insufficient roll cooling. Except in some cases, the cause is often a casting defect of the roll, insufficient strength, and excessive residual stress [14].

## 1. Introduction



1 Outer view, 2 Sectional view, 3 Shell, 4 Core, 5 Crack origin,  
6 Crack propagation, 7 Spalled part, 8 Roll rotation, 9 Surface crack

Figure (1–5): Schematic pattern of failure in a roll

Rolling condition	Breakage	Source of breakage				
		Roll material			Rolling condition	
		Defect	Strength	Residual stress	Thermal stress	Rolling stress
Normal	Body breakage	○	○	○	○	---
	Large spalling at center	○	○	○	△	○
	Large spalling at boundary	○	○	○	△	○
	Large spalling from surface	○	---	---	---	△
	Small spalling from surface	○	---	---	---	△
Abnormal	Large spalling*	---	---	---	○	○
	Small spalling	---	---	---	○	○
	Crack by cobble	---	---	---	○	○
	Crack by mill stoppage	---	---	---	○	---

Figure (1–6): Relation between breakage pattern and its source

### 1.3.2 Residual stress inside the work roll

During hot rolling process, the cyclic sequence of heating and cooling caused the thermal stresses to initiate firecracks at the roll surface [15]. Then, the combined action of thermal stress and residual stress may breakage the roll since the thermal breakage originates near the roll center and breaks out to the barrel surface [16] [2].

Since the residual stress after heating treatment has significant effect to improve the roll performance, it is necessary to control the residual stress inside the roll. Based on the efficient heating treatment technology, the continuous progressive heating with subsequent tempering after quenching is greatly suggested [17].

The heating treatment is a continuous process of pre-heating, quenching, and tempering. During pre-heating, some studies showed that by using non-uniform heating treatment, the different temperatures between the roll surface and roll center can be expected. Therefore, the failure risk from the roll center can be reduced since the roll center temperature can be greatly reduced. [18]. This non-uniform heating treatment type is also applied to the other steel material study [19].

Quenching heat treatment produces compressive residual stress to prevent fatigue crack at the roll outer layer [20] [21] [22]. However, to balance the compressive stress, tensile residual stress always appears at the roll center, which may cause the roll fracture. Decreasing the center tensile stress is therefore desirable to reduce the risk of fracture from the roll center. Since the residual stress can be controlled by the heat treatment, an appropriate quenching and tempering processes are required to improve bimetallic roll quality [23] [24].

Previous study investigated quenching and tempering treatment on the microstructure, mechanical properties, and abrasion resistance [25]. As the result, the optimum heat treatment methods are determined for the high-carbon HSS roll.

### 1.4 Motivation and Objectives

The work roll surface layer is frequently ground with a smaller rolling amount than the backup roll in order to remove surface roughness and wear due to surface roughness. For this reason, surface spalling where the rolling fatigue cracks generated from the roll surface are generated usually at the backup rolls. Unlike the outer layer of the work roll, which is grinding during use, the inner boundary and inner layer of the roll are subject to repeated loads exceeding  $10^7$  times, which corresponds to the total life of the roll. Small defects and abnormal micro-structures appearing during the casting process may cause delamination of the boundary layer due to the repeated rolling loads. In this way, in addition to extend the life of the roll, the conditions for using the roll are becoming stricter, such as high-load rolling due to the increased strength of the rolled material, and there is insufficient knowledge about fatigue fracture starting from the inside of the roll.

Figure (1–7) illustrates a proof of internal fatigue failure considered in this thesis [12]. In this high alloy grain roll, as shown in Figure (1–7), a semi-elliptical beach mark can be clearly seen near the HSS/DCI boundary at point B proving that the fatigue crack initiates at the inner boundary point A and propagates to the surface. Roll maker companies also identified that sometimes similar failure can be seen near the end of the roll body. Such peeling shown in Figure (1–7) is caused by the variation of radial stress  $\sigma_r$  during the roll rotation. In this way, the internal failure focused in this study is totally different from the surface spalling causing surface layer peeling observed in the backup rolls [26]. This is because the spalling is mainly controlled by the shear stress amplitude due to the rolling contact fatigue at several mm depth from the roll surface. Considering those situations, the authors have been keenly aware of the necessity for fatigue failure analysis. In other words, it is important to evaluate and clarify the fatigue risk over the entire roll based on the factors related to the strength of the roll itself and the stress caused by the rolling.

Therefore, in this study, a three-dimensional finite element method is applied to investigate the residual stress and the rolling stress of the bimetallic work roll in the four-high

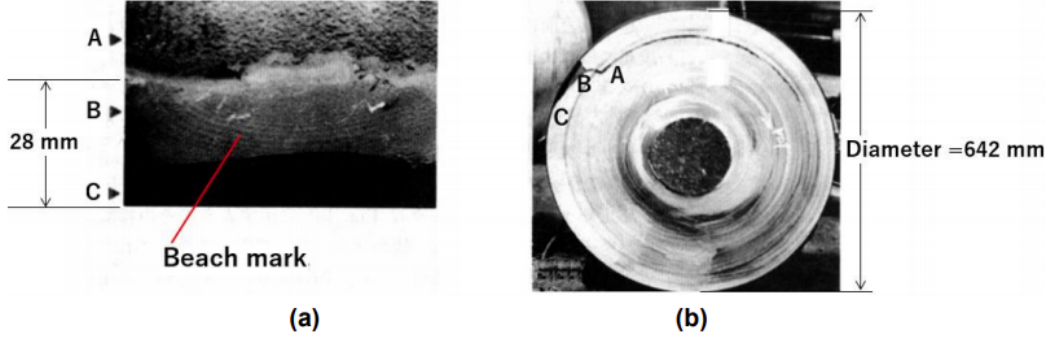


Figure (1-7): Failure at HSS/DCI boundary in bimetallic work roll (a) Fractured surface; A: Near boundary, B: Beach mark in shell, C: Roll surface, (b) Cross-section view of spalling crack

rolling mill. The residual stress is analyzed by considering pre-heating, quenching, and tempering. By using the results as an initial condition, the rolling stress analysis is performed consecutively. Then, the fatigue failure risk is discussed focusing on several critical points subjected to the largest stress amplitude inside of the work roll. The accuracy of the simple superposition method is also discussed to evaluate the risk conveniently. The thesis outline is composed of 6 chapters as following:

Chapter 1 gives a brief introduction of the bimetallic work roll used in 4-high rolling mill including the previous studies on the development of the bimetallic work roll to replace the single material roll. The characteristics of the bimetallic work roll are also discussed to improve the wear resistance, surface resistance, and heat-crack resistance. Then, the research problem, focusing on the failure of the HSS/DCI boundary due to the residual stress and the rolling stress are also explained.

Chapter 2 analyzes the residual stress distribution of the bimetallic work roll after completing heating and quenching treatment. A thermo-elastic-plastic finite element simulation is performed by using MSC Marc 2012 to investigate the residual stress during the quenching process. Uniform and non-uniform heating methods are considered to study the difference to the residual stress distribution.

In Chapter 3, by using similar simulation approach in previous chapter, the heating treatment is continued for tempering process. Residual stress distribution after two tem-

pering process is investigated for both uniform and non-uniform heating methods. Then, the usefulness of non-uniform heating method decreasing the center tensile stress is discussed.

After complete the pre-heating quenching and tempering treatment, the residual stress distribution will be used as the initial condition for the rolling analysis in the next chapter. However, since the heat treatment conditions may differ depending on each roll manufacturer, Chapter 4 considers zero residual stress in order to clarify only the mechanical stress. This assumed actual rolling analysis considers elastoplastic contact analysis of the half model of the 4-high rolling mill. The safety risk evaluation under compressive mean stress is newly prescribed under large compressive stress, evaluates the fatigue failure risk at the certain positions inside the bimetallic work roll.

Chapter 5 uses the residual stress distribution as the initial condition in the consecutive FEM analysis. The safety risk evaluation under compressive mean stress is also evaluated at the certain positions inside the bimetallic work roll. Since the consecutive FEM analysis considering each roll rotation is time-consuming, the simple evaluation method will be discussed by superposing the residual stress and the rolling stress.

Chapter 6 provides the main conclusions for the fatigue failure risk inside the bimetallic work roll during the rolling process of 4-high rolling mill.

## **2 Residual stress after the heating quenching treatment of the bimetallic work roll**

### **2.1 Introduction**

Previous study shows that the heat treatment produces compressive residual stress to prevent fatigue crack at the roll outer layer [27]. However, to balance the compressive stress, tensile residual stress always appears at the roll center, which may cause roll fracture. Decreasing the center tensile stress is therefore desirable to reduce the risk of fracture from the roll center. Since the residual stress can be controlled by the heat treatment, an appropriate quenching process is required to improve bimetallic roll quality [17].

In other studies [28] [29], the heating quenching treatments was discussed, although the material data were not indicated at the request of the company with which we collaborated. Since the material data could not be indicated, the detailed effect of the material on the residual stress has not yet been clarified.

Therefore, in this chapter, the simulation will be performed under specific provided material data where the new materials and new roll are considered. Then, the effect of the heat treatment will be discussed clearly by applying the finite element method (FEM) to the quenching process after uniform heating and non-uniform heating. Moreover, the effects of the roll diameter and the area ratio on the residual stresses will be discussed.

### **2.2 Mechanical properties of the bimetallic work roll**

Figure (2–1) shows the bimetallic rolls model used in this heating quenching analysis. This work roll is manufactured by the centrifugal casting method, in which high-speed steel (HSS) is used as the shell and ductile casting iron (DCI) is used as the core (see Figure (2–1)) [6–8].



## 2. Residual stress after the heating quenching treatment of the bimetallic work roll

As shown in Figure (2–1), the roll diameter  $D$  is 660 mm, HSS outer layer thickness is 60 mm, and the body length is 1800 mm. In order to remove the internal stress caused by the transformation in the cooling process after casting, the roll is annealed and gradually cooled to room temperature. As a result, the residual stress is considered negligible before the heating treatment, which is held at a temperature exceeding 1000°C. Even in the case of non-uniform heating, since the whole work roll is heated and then maintained at 600°C or higher, stress-free conditions were set as the initial conditions of the analysis.

Figure (2–2) shows the microstructure of the outer and inner layers around the boundary layer. In the outer layer of HSS, the carbides are fine and homogeneously distributed but coarsened at the boundary. In the inner layer of DCI, the spherical graphite is surrounded by ferrite. In Figure (2–2), a good diffusion state is maintained at the boundary and good composite structures are seen. Table (2-1) shows the chemical compositions and Table (2-2) shows the material properties for the outer layer of HSS and the inner layer of DCI.

Table (2-1): Chemical composition of the work roll(mass,%)

Element	C	Si	Mn	P	S	Ni
HSS	1~3	<2	<1.5	<1	<1	<5
DCI	2.5~4	1.5~3.1	<1	<0.1	<0.1	0.4~5

In our previous study [28], the material data were not indicated in detail since they

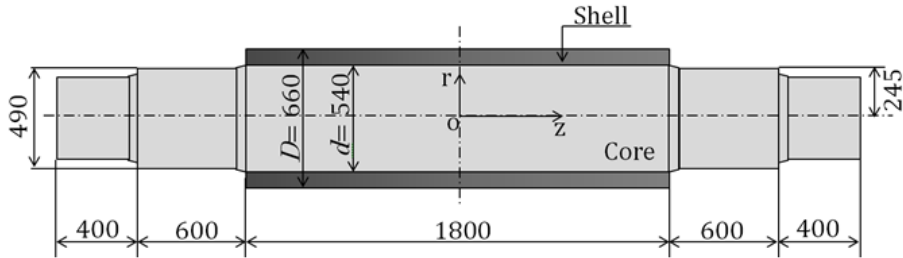


Figure (2–1): Model of the bimetallic roll (mm)

## 2. Residual stress after the heating quenching treatment of the bimetallic work roll

Table (2-1): cont.

Element	Cr	Mo	Co	V	W	Ag
HSS	2~7	<10	<10	3~10	<20	<10
DCI	0.01~1.5	0.1~1	<1	<1	<1	0.02~0.08

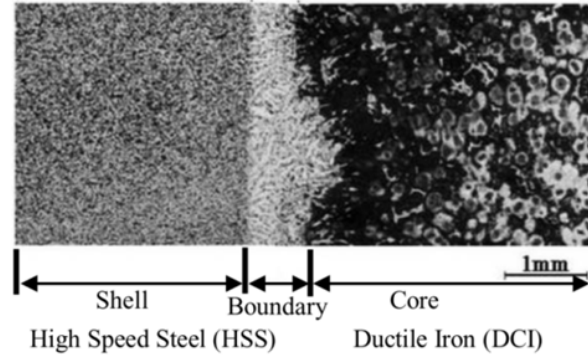


Figure (2-2): View of microstructure for a HSS roll with a DCI core

Table (2-2): Mechanical properties of the shell and core at room temperature

Property	Shell	Core
0.2% proof stress (MPa)	1270	410
Young' s modulus (GPa)	228	168
Poisson' s ratio	0.3	0.28
Density (kg/m <sup>3</sup> )	7600	7300
Thermal expansion coefficient (K <sup>-1</sup> )	$12.6 \times 10^{-6}$	$13 \times 10^{-6}$
Thermal conductivity (W/m·K)	20.2	23.4 kcal
Specific heat (J/(kg·K))	0.46	0.42
Shore hardness (Hs)	85	50

constituted confidential information of the roll manufacturing company. Since the purpose of this study is to clarify the residual stress during the quenching process, all material data are provided, as shown in Figure (2-3). This figure shows the Young' s modulus,

## 2. Residual stress after the heating quenching treatment of the bimetallic work roll

specific heat, thermal conductivity, thermal expansion coefficient, Poisson's ratio, and stress-strain characteristic for both HSS and DCI during the quenching process.

### 2.3 Analysis method

For the FEM analysis, the software MSC Software's Marc and Mentat 2012 is used to perform the simulation of the quenching process of the bimetallic roll, while the Newton-

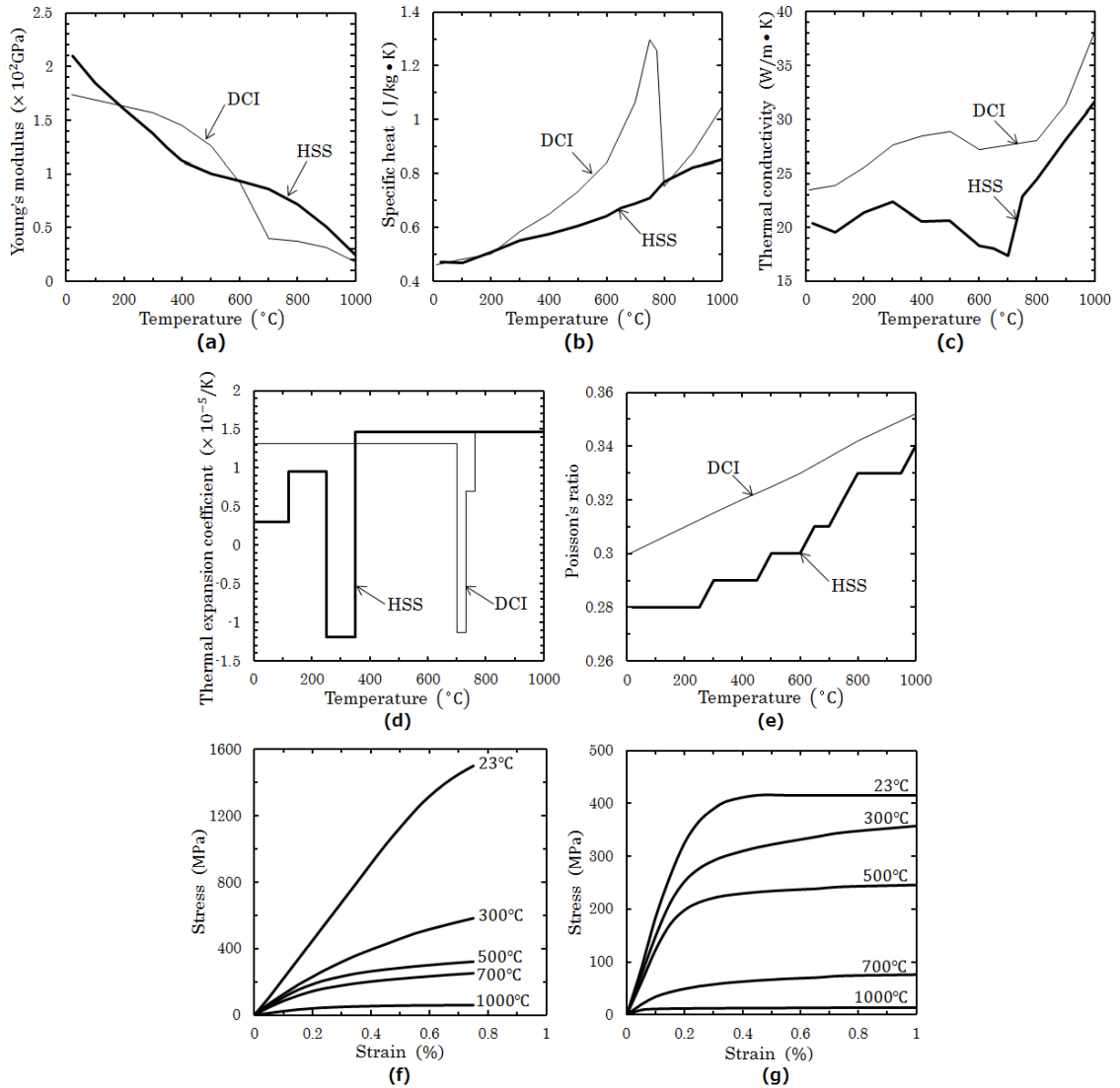


Figure (2-3): (a) Young's modulus; (b) specific heat; (c) thermal conductivity; (d) thermal expansion coefficient during quenching; (e) Poisson's ratio; (f) stress-strain for HSS; (g) stress-strain for DCI

## 2. Residual stress after the heating quenching treatment of the bimetallic work roll

---

Raphson strategy is used to solve non-linear equations in an implicit scheme. Figure (2–4) shows the transient-static simulation model of a half-length of the roll by using a four-node linear axisymmetric quad element with a mesh size of  $5 \times 5$  mm. Due to the symmetry, the thermal isolation conditions and displacement boundary conditions are applied as  $z = 0$ . This thermo-elastic plastic material model consists of 17,785 elements with 18,150 nodes and considered the Von Mises yield criterion and isotropic strain hardening rule.

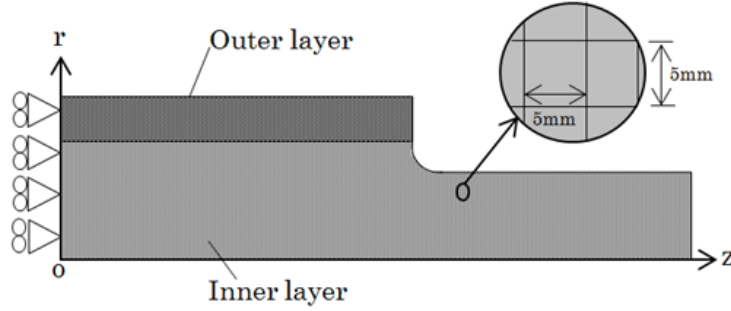


Figure (2–4): Finite element model for bimetallic roll

Figure (2–5) shows the temperature of the roll surface for (a) uniform heating; (b) non-uniform heating. All the material properties were measured experimentally from the initial quenching temperature,  $T_{Start}$ , to the end hardening temperature,  $T_{Finish}$ . These temperature histories are used as the thermal loading to create the residual stress field. Therefore, the thermal strains and stresses for each increment can be calculated.

For uniform heating in Figure (2–5)a, the entire work roll was heated up to the quenching start temperature,  $T_{Start}$ . Due to the uniform heating treatment, no residual stress appeared before the quenching process. For non-uniform heating in Figure (2–5)b, the entire roll was heated up initially to the pre-quenching temperature,  $T_{Heat}$ . After maintaining this temperature,  $T_{Heat}$ , for a certain time, the roll was rapidly heated up to a higher temperature. Due to this kind of treatment, small residual stress that is less than 30 MPa was found at the early stage of the quenching process. When the surface temperature reached the starting temperature  $T_{Start}$ , a mixed of water and air was discharged from the furnace to start the cooling process. During the cooling, the surface tempera-

## 2. Residual stress after the heating quenching treatment of the bimetallic work roll

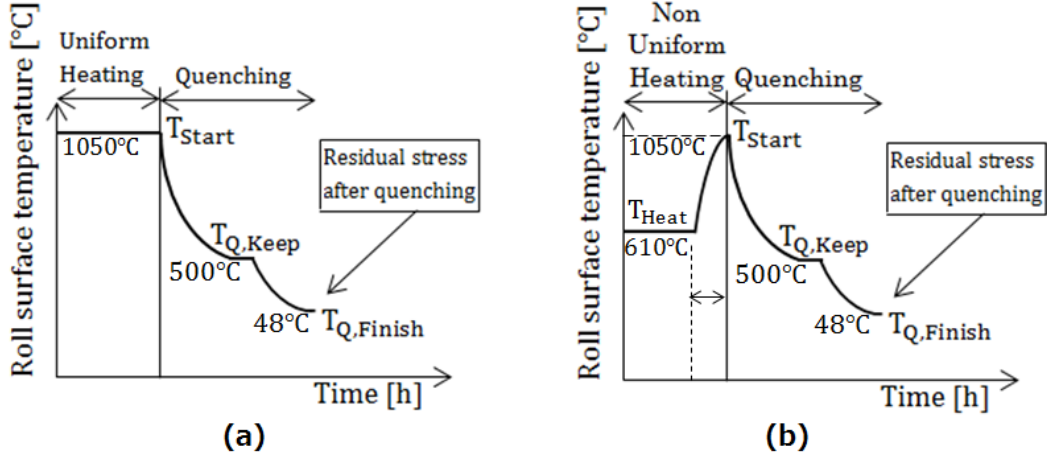


Figure (2–5): Work roll surface temperature during pre-heating and quenching (a) Uniform heating quenching; (b) Non-uniform heating quenching

ture of the roll was maintained at the keep temperature,  $T_{Q,Keep}$ , to alleviate the thermal stress accompanying the rapid decrease of the surface temperature. Then, the roll was cooled down slowly to the end temperature,  $T_{Finish}$ . The stress at this point was treated as the residual stress in this study, although the tempering was not completed. In the tempering treatment, the roll was tempered in the furnace after being heated up to the keeping temperature,  $T_{T,Keep}$ , and maintained for a certain time. Then, it was gradually cooled in the furnace to complete the heat treatment.

In the creep analysis, the transient creep strain was considered where the time hardening law was used to express the core material due to its low strength under high temperature. The core creep equation is given as:

$$\varepsilon_c = A\sigma^m t^n \quad (2-1)$$

where  $\varepsilon_c$  is the transient strain,  $\sigma$  is the stress,  $t$  is the time, and  $A$ ,  $m$ , and  $n$  are temperature-dependent material constants. All these unknown constants are determined by performing experimental creep tests [30]. Details on this creep analysis will be discussed in Chapter 3.

## **2.4 Influence on Residual Stress by Non-Uniform Heating**

By performing non-uniform heating, the surface and center temperatures will be different. As a result, the risk of roll failure can be reduced by decreasing the center tensile residual stress. The other advantages of non-uniform heating quenching are listed as follows:

1. The internal temperature is lower than  $900^{\circ}\text{C}$ , which contributes to the avoidance of overheating and prevents material deterioration.
2. Due to the rapid cooling of the quenching, a hard shell is obtained, improving the impact strength of the roll. Energy consumption can be reduced because the heating time is shortened.
3. The time and cost of the operation can be also reduced since the time required for heating is shortened.

Figure (2–6) shows the distribution of the residual stress  $\sigma_z$  in the central cross-section of the roll. In this thermal analysis, a total of 905 load steps, corresponding to  $t = 1140\text{s}$ , were required to complete the heating cycles.

As shown in Figure (2–6), the maximum tensile stress for non-uniform heating appearing at the roll center decreased to 141 MPa. The compressive residual stress at the surface decreased, but remained sufficiently large enough to guard against thermal crack. Meanwhile, the maximum tensile stress for non-uniform heating was 24% less than that for uniform heating. From Figure (2–6), it may be considered that non-uniform heating is efficient in reducing the fracture risk at the roll center without losing the crack prevention ability of the roll surface.

## 2. Residual stress after the heating quenching treatment of the bimetallic work roll

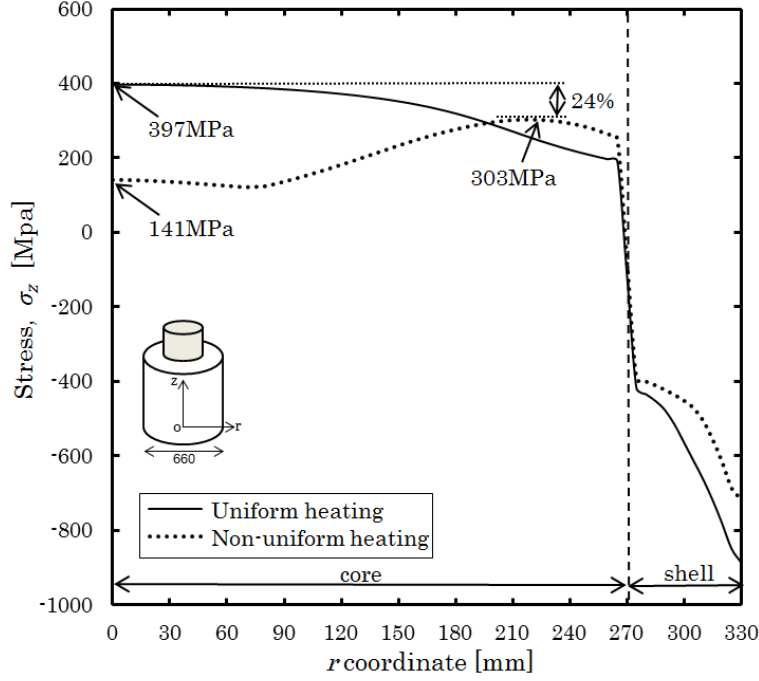


Figure (2-6): Comparison of residual stress distribution,  $\sigma_z$  for both heating treatments.

## 2.5 Comparison between uniform and non-uniform heating quenching treatment

### 2.5.1 Stress generation mechanism of uniform and non-uniform heating quenching

Figure (2-7) and Figure (2-8) show the results for (a) temperature versus time and (b) corresponding stress,  $\sigma_z$  versus time for uniform and non-uniform heating processes. As shown in Figure (2-7), the period A is a heating process while the periods B, C, D, and E are the quenching processes. During process A, no difference can be seen between the center and surface since the roll is heated up uniformly and no stress occurs. During the rapid surface cooling process B the tensile stress of the outer layer increases initially due to the cooling shrinkage of the outer layer. However, the tensile stress suddenly changes to compressive stress because the thermal shrinkage at the central part becomes larger. Pearlite transformation appears at the inner layer at the pearlitization tempera-

## 2. Residual stress after the heating quenching treatment of the bimetallic work roll

ture,  $T_{Pearlite}$ , which expands from the inner layer boundary toward the roll center. During this process, B, the center compressive stress decreases until reaching  $T_{Pearlite}$ . During process C, the pearlite transformation causes the formation of compressive stress at the roll center. Then, the tensile stress at the center with a high cooling rate increases and eventually the stress at the center and the stress at the surface intersect. The compressive stress at the surface and the tensile stress at the center maintain until the temperature  $T_{Q,Keep}$  is reached. During the initial temperature keeping period, D, since the heating is applied to adjust the overcooling at the roll surface, both the surface compressive stress and the center tensile stress increase slightly. After heating, the temperature difference becomes smaller between the surface and the center. During period E, the surface cooling starts outside the furnace, and the surface temperature decreases. Then, the center tensile stress and the surface compressive stress both increase. During period E, Bainite expansion transformation occurs at the inner layer at the bainitization temperature,  $T_{Bainite}$ , promoting the surface compressive stress and the center tensile stress.

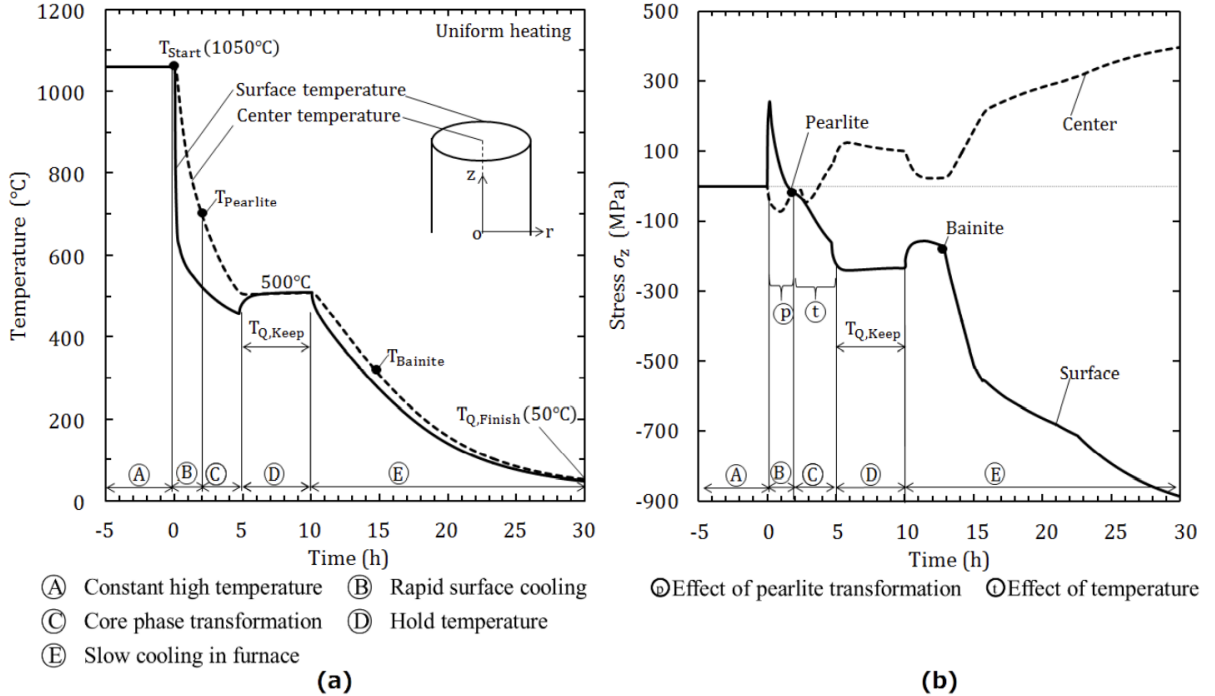


Figure (2-7): Uniform heating process and corresponding stress  $\sigma_z$ : (a) temperature versus time and (b) stress  $\sigma_z$  versus time



## 2. Residual stress after the heating quenching treatment of the bimetallic work roll

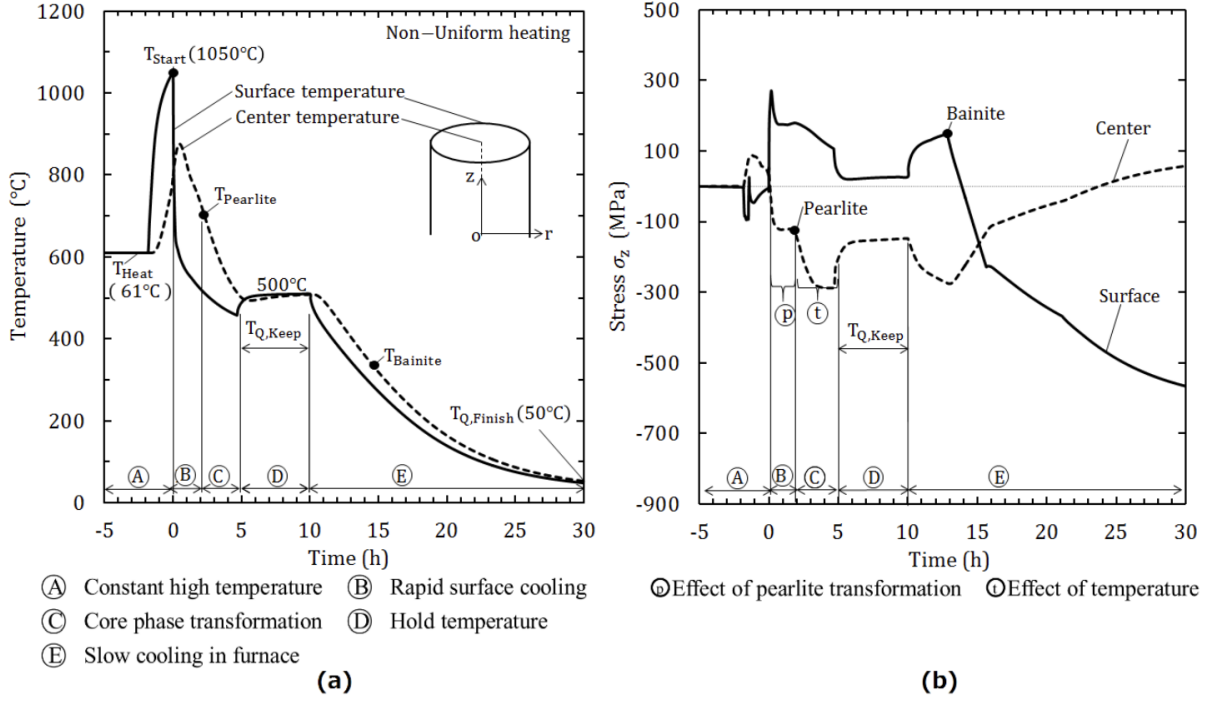


Figure (2-8): Non-Uniform heating process and corresponding stress  $\sigma_z$ : (a) temperature versus time and (b) stress  $\sigma_z$  versus time

As shown in Figure (2-8), during the non-uniform heating process A, the entire roll is heated up initially to the pre-quenching temperature,  $T_{\text{Heat}}$ . After that, the roll surface is rapidly heated up to the roll surface temperature,  $T_{\text{Start}}$ , while the roll center is heated at a lower temperature in a non-uniform manner. At the early stage of this heating process, tension is generated at the center due to the surface thermal expansion. The surface compressive stress turns into tensile stress due to transformation contraction at the austenitization temperature,  $T_{\text{Austenite}}$ . After that, the temperature difference becomes smaller between the surface and the center and both stresses decrease. At the initial stage of quenching B, a large tensile stress forms at the surface because of the high cooling speed. The pearlite transformation occurs at the initial stage of C, and the center compressive stress is maintained. At the initial stage of D, due to the roll surface heating process, the surface tensile stress turns into compressive stress. During the temperature keeping period,  $T_{\text{Q,Keep}}$ , the temperature difference becomes smaller between the surface and the center. Then, the stress change is small. During the air-cooling period E, Bainite

## 2. Residual stress after the heating quenching treatment of the bimetallic work roll

---

expansion transformation occurs. In the outer layer—similar to the uniform heating case in Figure (2–7)—both the surface compressive stress and the center tensile stress increase.

As shown in Figure 2-6, the central compressive stress under uniform heating becomes smaller than that under non-uniform heating. This can be explained by the following. During pearlite transformation  $\textcircled{P}$ , in Figure 2-7 and Figure 2-8, the stress change under non-uniform heating (indicated as  $\textcircled{P}$  in Figure 2-8) is smaller than the stress change under uniform heating (indicated as  $\textcircled{P}$  in Figure 2-7). In a similar way, the central stress increase (indicated as  $\textcircled{t}$  in Figure 2-8) under non-uniform heating is also smaller than the central stress increase (indicated as  $\textcircled{t}$  in Figure 2-7) under uniform heating after the pearlite transformation. The effects of the temperature keeping period D, and air-cooling period E, are nearly the same in Figure (2–7)b and Figure (2–8)b. In the non-uniform heating process, the smaller stress increase after the central pearlite transformation results in the reduction of the center tensile stress.

### 2.5.2 Effect of diameter on uniform and non-uniform heating quenching

Figure (2–9)a shows the residual stress distribution for uniform heating obtained by varying the diameter from 500 mm to 1000 mm in increments of 100 mm with an area ratio of 0.4. Since the area ratio is fixed, the residual stress of the inner layer can be represented by the stress at the center. At the center, the tensile stress increases by 53 MPa as the diameter changes from 500 mm to 1000 mm. Meanwhile, Figure 2-9b shows the diameter effect result of non-uniform heating. The result is significant as the real roll diameter used is between 600 mm to 800 mm. The maximum tensile stress at the inner layer is 261 MPa when the roll diameter is 900 mm. The surface compressive stress varies significantly as the roll diameter changes from 500 mm to 600 mm.

## 2. Residual stress after the heating quenching treatment of the bimetallic work roll

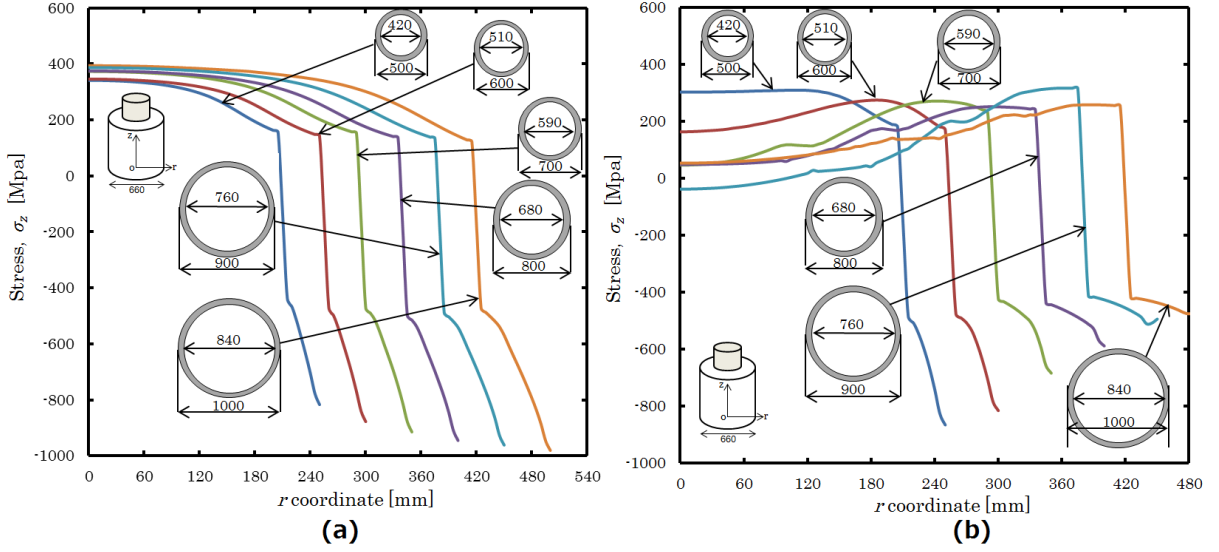


Figure (2-9): Residual stress distribution  $\sigma_z$  for different diameters: (a) Uniform heating; (b) Non-uniform heating

### 2.5.3 Effect of area ratio on uniform and non-uniform heating quenching

Figure (2-10) shows the residual stress distribution for different area ratios for uniform and non-uniform heating processes. The outer roll diameter is fixed as 660 mm. For uniform heating, the center tensile stress increases by 120 MPa as the area ratio changes from 0.2 to 0.8. Meanwhile, for non-uniform heating, the tensile stress increases by 127 MPa for the same ratios. The compressive stresses at the surface are almost unchanged for both results. The results show that the area ratio only exerts a small influence on the residual stress of the bimetallic roll.

## 2.6 Conclusion for Chapter 2

In this chapter, residual stress was discussed under uniform and non-uniform heating treatments by considering creep behavior. The bimetallic roll tested consisted of high-speed steel at the shell and ductile cast iron at the core. Although a similar study can be found in previous work, no material data was indicated. In the current work, all the material data were indicated to provide a detailed view of the effects of material properties

## 2. Residual stress after the heating quenching treatment of the bimetallic work roll

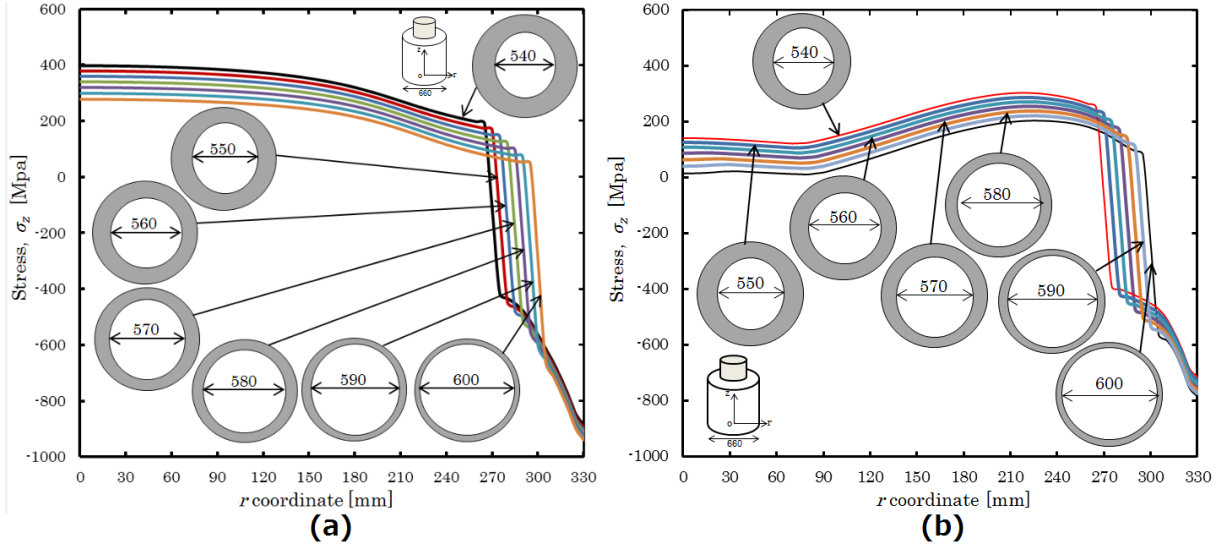


Figure (2-10): Residual stress distribution  $\sigma_z$  for different area ratios: (a) Uniform heating; (b) Non-uniform heating

on residual stress.

After uniform and non-uniform heating treatments, the quenching process was simulated by applying thermo-elastic plastic finite element method analysis. The conclusions are summarized as follows:

1. The tensile stress of the inner layer after non-uniform heating and quenching was less than that obtained after uniform heating and quenching by 24%, while the compressive stress on the surface for both heating treatments did not differ greatly. As a result, the effect of preventing surface cracking can be expected to reduce damage originating from the center.
2. Based on the stress generation mechanisms, it was found that the stress in the central part decreased by non-uniform heating because during pearlite transformation B, the increase in the central stress in non-uniform heating ⑤ was small. Similarly, the increase in the central stress ⑥ in non-uniform heating is also small in region C after the pearlite transformation.
3. Based on the diameter effect result, the center tensile stress for non-uniform heating

## **2. Residual stress after the heating quenching treatment of the bimetallic work roll**

---

was smaller compared to that for uniform heating. Furthermore, the surface compressive stress varied significantly as the diameter changes from 500 mm to 1000 mm.

4. The results of the area ratio effect showed that the center tensile stress almost unchanged as the diameter changes from 500 mm to 1000 mm for uniform heating. For non-uniform heating, the center tensile stress changed when the area ratio changed. The surface compressive stress varies significantly as the roll diameter changes from 500 mm to 600 mm.

## 3 Residual stress after the heating, quenching, and tempering treatment of the bimetallic work roll

### 3.1 Introduction

In previous chapter, the residual stress after quenching of the bimetallic work roll was discussed by varying the thermal conditions as well as the roll dimensions since the residual stress is mainly controlled by the heat treatment of the roll.

For this chapter, to reduce the internal stress, the additional heat treatment called tempering is done after quenching.

### 3.2 Analysis method

Thermo-elastic-plastic finite simulation is performed by using similar analytical model with the previous quenching analysis in Chapter 2 by using the similar material properties, mechanical properties and chemical compositions for HSS and DCI.

The residual stress distribution after two tempering process is investigated for both uniform and non-uniform heating methods. Figure (3–1) shows the temperature of the roll surface for both uniform heating and non-uniform heating. Quenching simulation has been discussed in previous chapter and for this chapter, the tempering simulation will be continued after the quenching end point  $T_{Q,Finish}$ . The temperature is raised again to  $T_{T,Keep}$  and after a certain time, it is slowly cooled until  $T_{T,Finish}$  to complete one tempering cycle.

### 3.3 Effect of creep behaviour on residual stress

In the creep analysis, the transient creep strain also should be considered as well as the steady creep strain. Among several equations available for creep analysis, the time

### 3. Residual stress after the heating, quenching, and tempering treatment of the bimetallic work roll

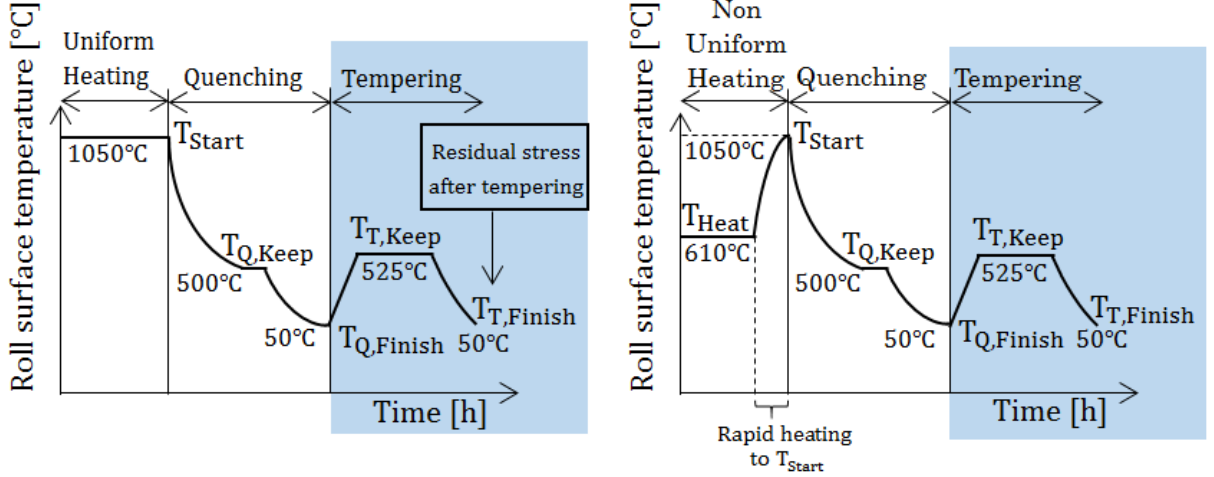


Figure (3–1): Work roll surface temperature during pre-heating, quenching and tempering; (a) Uniform heating quenching; (b) Non-uniform heating quenching

hardening law, sometimes called power law, is used to express the core material which has low strength under high temperature. It should be noted that the creep should be considered in a short hours for the roll quenching compared to the common creep analysis. The creep equation can be given as the following Eq (3–1). [31]

$$\varepsilon_c = A\sigma^m t^n \quad (3-1)$$

where  $\varepsilon_c$  is the transient strain,  $\sigma$  is the stress,  $t$  is the time, and  $A$ ,  $m$ , and  $n$  are temperature-dependent material constants.

In order to examine the validity of Eq. (3–2) and Eq. (3–3), the stress relaxation effect obtained by the stress relaxation test was compared with the stress reduction effect by creep. This creep testing was conducted by using a miniature creep rupture testing machine based on JIZ2271 [32]. The specimen were prepared from the core material DCI due to its low-temperature strength.

Those specimens were, respectively, heated up to the testing temperatures,  $T_{Q,Keep}$  and  $T_{T,Keep}$ , and kept at theses temperatures during the testing process. Then, the creep tests were carried out by applying constant loads 130 and 160 MPa. The strain changes were

### 3. Residual stress after the heating, quenching, and tempering treatment of the bimetallic work roll

recorded with time. From the strain–time curves obtained, the creep equations can be written as shown in Eq. (3–2) and Eq. (3–3).

$$\varepsilon_c = 2.23 \times 10^{-13} \sigma^{3.442} t^{0.6724} \text{ at } T_{Q,Keep} = 500^\circ\text{C} \quad (3-2)$$

$$\varepsilon_c = 8.43 \times 10^{-16} \sigma^{5.003} t^{0.4919} \text{ at } T_{T,Keep} = 525^\circ\text{C} \quad (3-3)$$

As shown in Figure (3–2), the creep test is the strain of the test piece pulled at a constant stress in a high temperature atmosphere. In contrast to the time change of the initial stress, the stress relaxation test looks at the time change of the initial stress with a constant displacement, and both evaluate the properties of the same roll material.

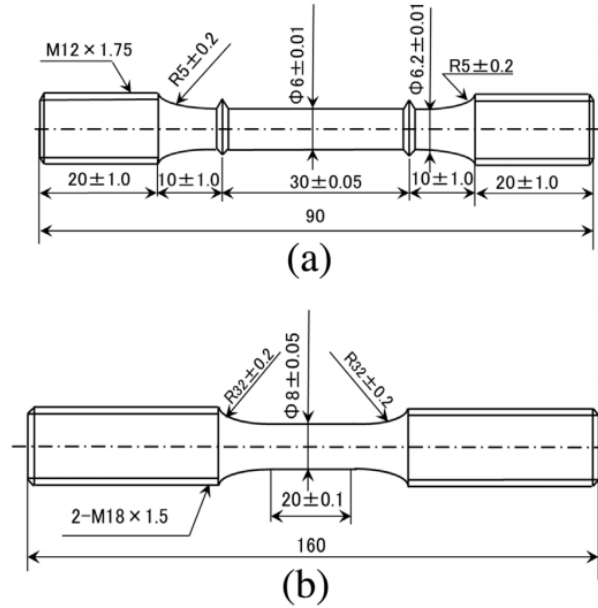


Figure (3–2): Specimen of creep test and stress relaxation test; (a) Specimen of creep test (mm); (b) Specimen of stress relaxation test (mm)

It is confirmed that the results of the stress relaxation test performed using the initial stress of 130 MPa and 160 MPa on the inner layer material at both  $T_{Q,Keep}$  and  $T_{T,Keep}$  have similar results with the same simulation using Eq. (3–2) and Eq. (3–3) [29]. It has been used for the analysis of creep effect [30]. The creep effect during the raising temperature



### 3. Residual stress after the heating, quenching, and tempering treatment of the bimetallic work roll

and cooling temperature is small. Therefore, the creep effect is only considered during the temperature holding process, which has a large creep effect. During  $T_{Q,Keep}$  and  $T_{T,Keep}$ , the creep behavior is considered at the roll's core layer due to its low-temperature strength.

#### 3.4 Residual stress distribution

Stress distribution of the axial residual stress  $\sigma_z$  from the roll center to the roll surface will be considered for this study. Figure (3–3) shows the stress distribution after quenching, after first tempering, and after second tempering for uniform heating quenching. After the first tempering, the maximum tensile stress decreased by 35% from 397 MPa to 257 MPa. Meanwhile, after the second tempering, it decreased by 54% from 397 MPa to 183 MPa.

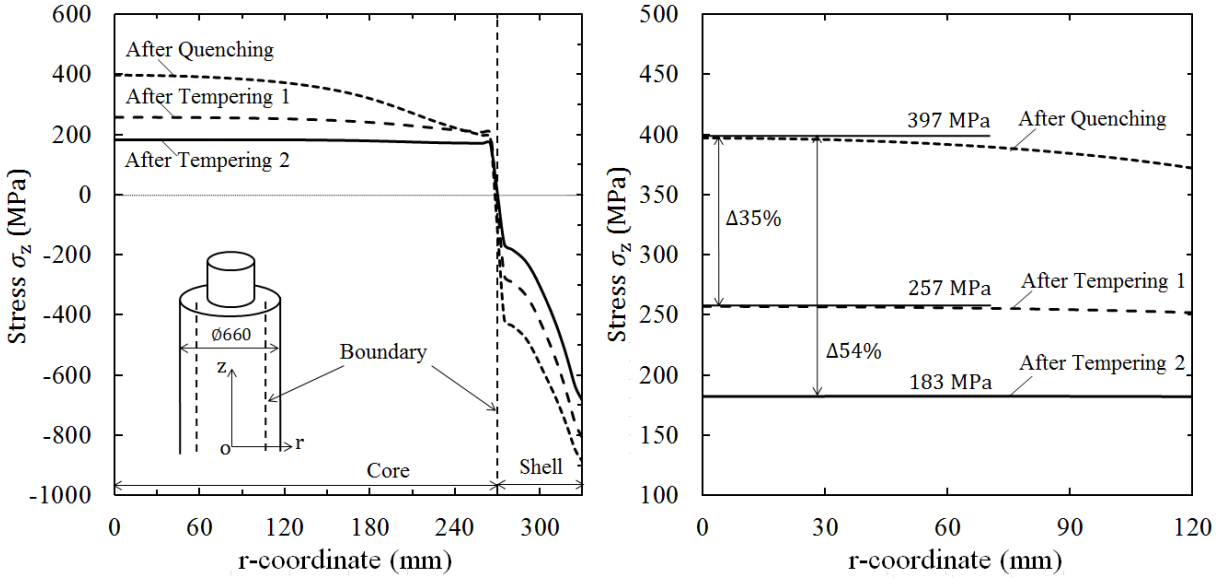


Figure (3–3): Effect of tempering after uniform heating, quenching and tempering; (a) Tempering after uniform heating quenching; (b) Details of maximum stress range

Figure (3–4) shows the stress distribution after quenching, after first tempering, and after second tempering for non-uniform heating quenching. After the first tempering, the maximum stress reduced by 25% from 286 MPa to 214 MPa. After the second tempering,

### 3. Residual stress after the heating, quenching, and tempering treatment of the bimetallic work roll

it decreased by 46% from 286 MPa to 183 MPa.

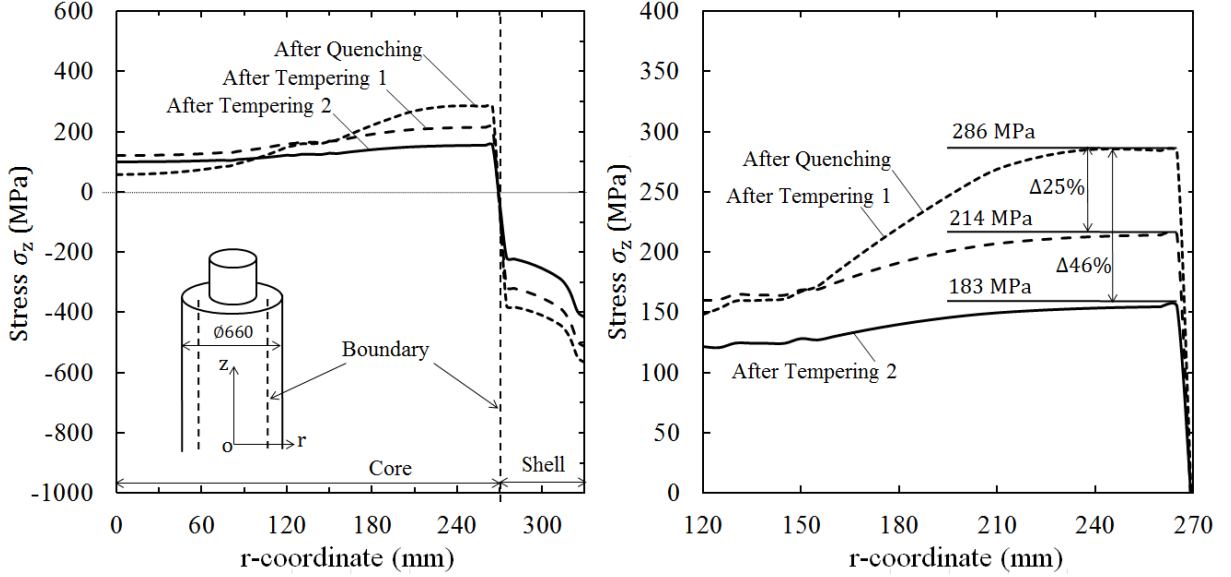


Figure (3-4): Effect of tempering after non-uniform heating, quenching and tempering; (a) Tempering after non-uniform heating quenching; (b) Details of maximum stress range

From Figure (3-3) and Figure (3-4), it may be concluded that nonuniform heating quenching is useful in reducing the risk of roll failure by decreasing the center tensile stress without decreasing the surface compressive stress.

### 3.5 Stress generation mechanism during tempering

Figure (3-5) and Figure (3-6) show the time course of the surface and center temperature from the start of tempering to the end of the second tempering, and the time course of the surface and center stress. In the tempering performed after uniform heat quenching, as shown in Figure (3-3)a, The maximum stress point occurs in the center. On the other hand, the maximum stress point of the inner layer after non-uniform heat quenching appears near the boundary between the inner and outer layers, so the stress history of the maximum stress point is added. Since the formation mechanism is described, in this paper, the stress change with time is described by focusing on the part where the stress change is observed, starting from the start of tempering. By comparing Figure (3-5) and

### **3. Residual stress after the heating, quenching, and tempering treatment of the bimetallic work roll**

Figure (3–6), there is a difference in stress level. However, because the stress changes in the same way, the explanation for Figure (3–6) will be similar to Figure (3–5).

As shown in Figure (3–5), the temperature of the outer layer changes near 200°C at (1). Because of the structure change at the outer layer, the stress increases slightly in the tensile direction (1) to (2). During the keeping temperature (2) to (3), the stress at the center of the roll is decreased before and after the start of creep due to the creep effect. After the temperature is maintained, the compressive stress on the surface decreases and the tensile stress also decreases in the center as the surface temperature decreases (3) to (4). After that, the temperature at the center of the roll and the surface The stress transition is shown only by the difference, and no significant change is observed (4) to (5). In the region where the retained austenite in the outer layer material undergoes martensite transformation, it increases again to the compression side due to transformation expansion (5) to (6). The stress at the center also increases so that it is balanced with the surface (5) to (6). This completes the first tempering.

The second tempering (6) to (11) shows the same stress transition tendency as the first, with the central stress reduced by 33% from the start of the first tempering. At the transformation expansion point of the outer layer during the raising temperature, the transformation expansion amount in the second raising temperature process is not as large as the first time.

## **3.6 Conclusion for Chapter 3**

In this chapter, the tempering treatment of the bimetallic roll is analyzed by considering the creep effect and transformation effect. The bimetallic roll model has a diameter of 660 mm using HSS outer layer and DCI inner layer. The analysis is performed to two tempering processes by using the thermal elasto-plastic finite element method, and the effect on the residual stress distribution is considered. The conclusions obtained are shown below.

### 3. Residual stress after the heating, quenching, and tempering treatment of the bimetallic work roll

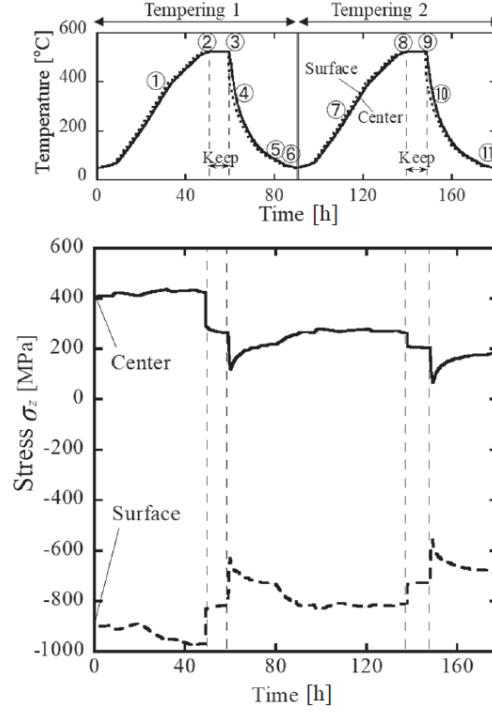


Figure (3–5): Histories of temperature and stress  $\sigma_z$  during tempering process after uniform heating

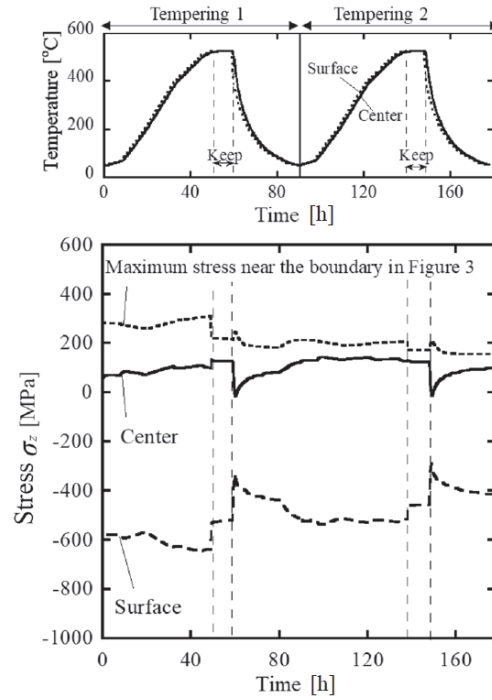


Figure (3–6): Histories of temperature and stress  $\sigma_z$  during tempering process after non-uniform heating

### **3. Residual stress after the heating, quenching, and tempering treatment of the bimetallic work roll**

1. It may be concluded that tempering treatment is useful in reducing the risk of roll failure by decreasing the center tensile stress without decreasing the surface compressive stress.
2. For uniform heating quenching, the maximum stress at the center decreased by 35% from 397 MPa to 257 MPa after the first tempering. The second tempering reduced the maximum stress by 54% from 397 MPa to 183 MPa.
3. For non-uniform heating quenching, the maximum stress decreased by 25% from 286 MPa to 214 MPa after the first tempering. The second tempering reduced the maximum stress by 46% from 286 MPa to 183 MPa.
4. It is found that in this tempering process, the residual stress inside the roll is reduced by stress relaxation due to the creep effect.

## 4 Rolling stress and fatigue failure during rolling analysis

### 4.1 Introduction

In Chapter 4, to observe the fatigue failure risk inside the bimetallic work roll, the rolling stress analysis will be performed consecutively after pre-heating, quenching and tempering. However, since the heat treatment conditions are different depending on each roll manufacture companies, this chapter will focus on clarifying the rolling stress in four high rolling mill, which has not been studied until now.

In this chapter, we focus on the rolling stress generated inside the bimetallic work roll in the 4-high rolling mill, based on the fatigue risk evaluation. Residual stress is absolutely necessary as a rolling force factor, but since the effect of rolling stress is the first priority, the residual stress is set to zero for this study. Then, from the viewpoint of rolling stress, the safety evaluation of the fatigue fracture will be considered at some critical points.

### 4.2 Problem background

Compared to the backup roll, the work roll surface is frequently ground with a smaller wear amount in order to use the surface repeatedly by removing surface roughness caused by wear during the use. For this reason, surface spalling caused by the crack initiated at the roll surface hardly occurs in work rolls although often occurs in backup rolls. Although the outer surface damage is often removed, the inner layer of the bimetallic roll is consecutively used and therefore is subjected to large number of load repetitions exceeding  $10^7$  times corresponding to the total life of the roll. Small defects and abnormal microstructures appearing at the casting process may cause delamination of the HSS/DCI boundary layer due to the repeated rolling loads. Since the recent work roll tends to be used for a longer period under severe condition by applying high strength materials,

#### 4. Rolling stress and fatigue failure during rolling analysis

---

the fatigue fracture caused by the crack initiation at the inside of the roll is becoming important. Figure (4–1) illustrates an example of internal fatigue failure considered in this thesis [33] [12].

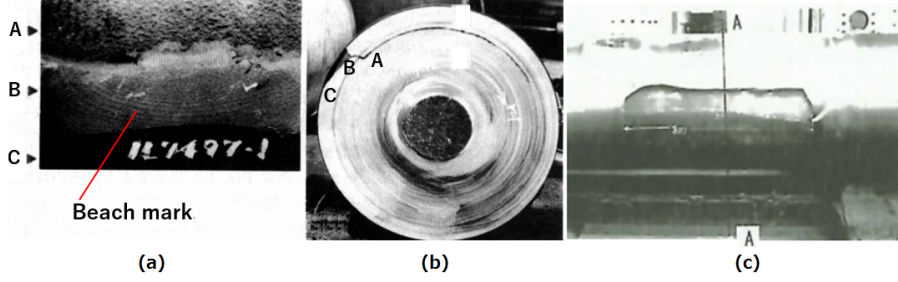


Figure (4–1): Failure at HSS/DCI boundary in bimetallic work roll; (a) Fractured surface; A: Near boundary, B: Beach mark in shell, C: Roll surface, (b) Cross-section A-A view from right figure, (c) Outer view of spalling

In this high alloy grain roll, as shown in Figure (4–1)a, a semi-elliptical beach mark can be clearly seen near the HSS/DCI boundary at point B proving that the fatigue crack initiates at the inner boundary point A and propagates to the surface. Roll maker companies also identified that sometimes similar failure can be seen near the end of the roll body (see point  $B_{750}^{270}$  in Figure (4–25)). Such peeling shown in Figure (4–1) is caused by the variation of radial stress  $\sigma_r$  during the roll rotation. In this way, the internal failure focused in this study is totally different from the surface spalling causing surface layer peeling observed in the backup rolls. This is because the spalling is mainly controlled by the shear stress amplitude due to the rolling contact fatigue at several mm depth from the roll surface. Considering those situations, the authors have been keenly aware of the necessity for fatigue failure analysis. In other words, it is important to evaluate and clarify the fatigue risk over the entire roll based on the factors related to the strength of the roll itself and the stress caused by the rolling.

Therefore, in this study, the fatigue risk will be evaluated by focusing on the rolling stress appearing inside of the bimetallic work rolls when the work roll is used in 4-high rolling mill. It is necessary to consider the residual stress of the work roll in the final

evaluation of fracture risk. However, the heat treatment conditions are different depending on each roll manufacture companies. Therefore, this study focuses on clarifying the rolling stress in four high rolling mill, which has not been studied until now. For this purpose, the residual stress is set to zero and the fatigue fracture risk point will be clarified from the viewpoint of rolling stress.

### 4.3 FEM modelling and fundamental dimension and condition of the work roll and backup roll

Table (4-1) shows the roll dimensions used in the analysis. As shown in Table (4-1) and Figure (4-2), the work roll diameter is  $D_W=660$  mm, the backup roll diameter is  $D_B=1400$  mm, and the body length for both work roll and backup roll is  $L=1800$  mm. The width of the rolled steel is  $W=1200$  mm. The work roll as well as the backup roll is subjected to the total rolling force  $P_{total}$  whose standard value is  $P_{total}=16400$  kN [34] [35]. Then, the work roll is subjected to the line force  $p_S^{ave} = P_{total}/W$  from the rolled steel. Also, the work roll is subjected to the line force  $p_B^{ave} = P_{total}/L$  from the backup roll. As shown in Figure (4-2), the backup roll is chamfered with a length of 90 mm and a depth of 20 mm [36]. The necessity of chamfering will be described in Section 4.4.

Table (4-2) shows the material properties of the rolls used in the analysis [37]. High-chrome steel is used for the backup roll, high-speed steel (HSS) is used for the outer layer of the work roll, and ductile casting iron (DCI) is used for the inner layer of the work roll. The outer layer HSS has a thickness of 60 mm in the region  $r = 270 \sim 330$  mm. During one roll rotation, the thermal stress appears due to heating and cooling from the hot rolled steel. However, it is known that the thermal stress affects only a few  $\mu\text{m} \sim 1$  mm depth from the surface and never affect the inside boundary stress [38] [39]. After the rolling starts, the roll temperature increases and becomes stable after 1 hour under an equilibrium temperature of about  $50^\circ\text{C} \sim 80^\circ\text{C}$  [12] [20]. Since the rolling operation is more than 10 hours continuously before removing the damaged roll surface, the effect of



#### 4. Rolling stress and fatigue failure during rolling analysis

Table (4-1): Rolling size and condition (Base value)

Size	Work roll	Backup roll	Rolled steel
Diameter (mm)	$D_W=660$	$D_B=1400$	-
Length/Width (mm)	$L = 1800$	$L = 1800$	$W = 1200$
Rolling force, $P_{total}$ (kN)	16400		
Line force, $p_B^{ave}$ from Backup roll (kN/mm) $P_{total}$ (kN)	$P_{total}/L=9.11$		
Line force, $p_S^{ave}$ from Rolled steel (kN/mm) $P_{total}$ (kN)	$P_{total}/W=13.67$		

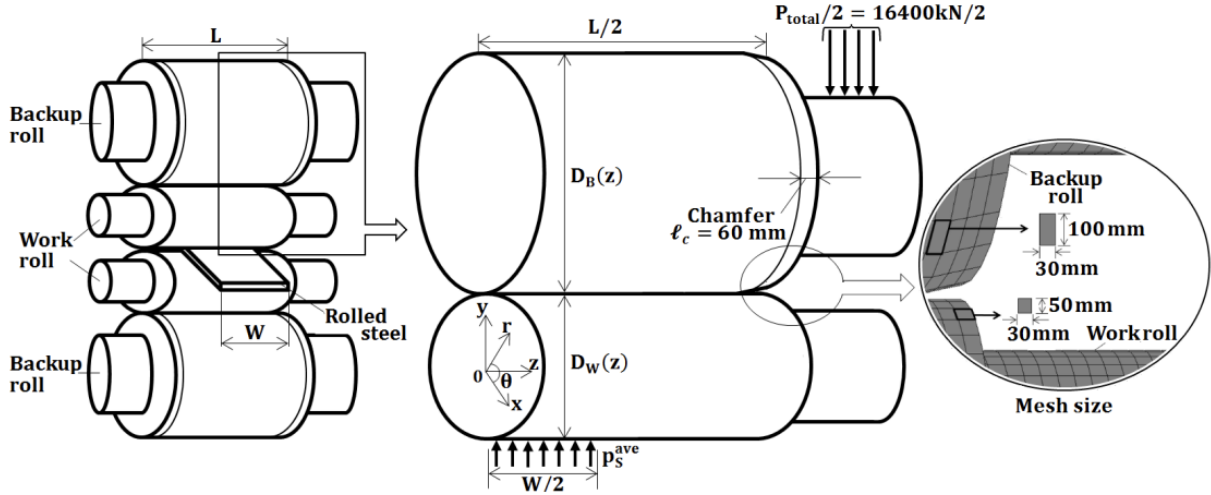


Figure (4-2): Three-dimensional FEM model of four-high rolling mill

thermal stress at the initial stage of rolling is relatively smaller and can be ignored when considering fatigue fracture [12].

Therefore, in this study, the thermal stress is not considered and the analysis is performed at room temperature. Figure (4-3) shows the stress-strain diagrams used for elastoplastic contact analysis for both HSS and DCI layers. They are provided in the analysis software MSC Marc / Mentat 2012 as the material properties at room temperature.

#### 4. Rolling stress and fatigue failure during rolling analysis

Table (4-2): Mechanical properties of the shell and core at room temperature

Property	HSS	DCI	Backup Roll
0.2% proof stress (MPa)	1270	410	
Tensile strength (MPa)	1575	415	1575
Fatigue strength (MPa)	630	166	630
Yield strength (MPa)	1270	410	-
Young' s modulus (GPa)	230	174	210
Poisson' s ratio	0.3	0.28	0.3
Density (kg/m <sup>3</sup> )	7600	7300	7800

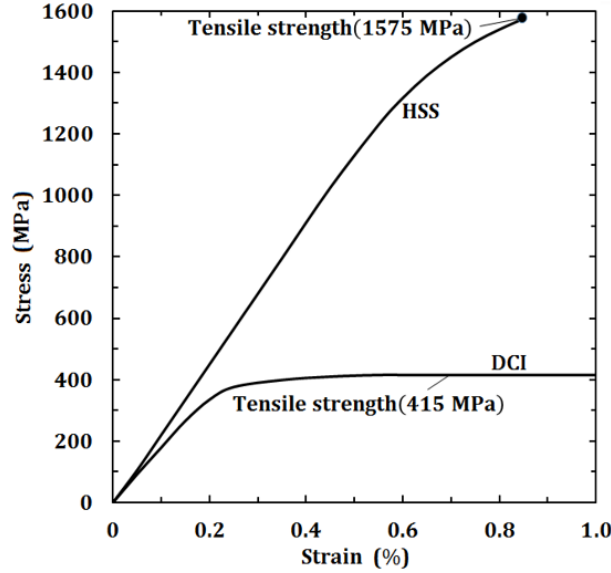


Figure (4-3): Stress-strain relations for HSS and DCI

The software MSC Marc/Mentat 2012 is applied to performing the three-dimensional elastoplastic analysis since it is not clear whether plastic deformation occurs or not in the internal region of the work roll. Figure (4-4) shows the FEM analysis model whose minimum mesh has dimensions 30 mm x 30 mm x 30 mm. The FEM element used are 4-node tetrahedral element. and 8-node hexahedral element for the stress concentration part. The number of nodes is 22,320 and the number of elements is 20,006. The direct

#### 4. Rolling stress and fatigue failure during rolling analysis

constrain method is used for contact analysis between work roll and backup roll.

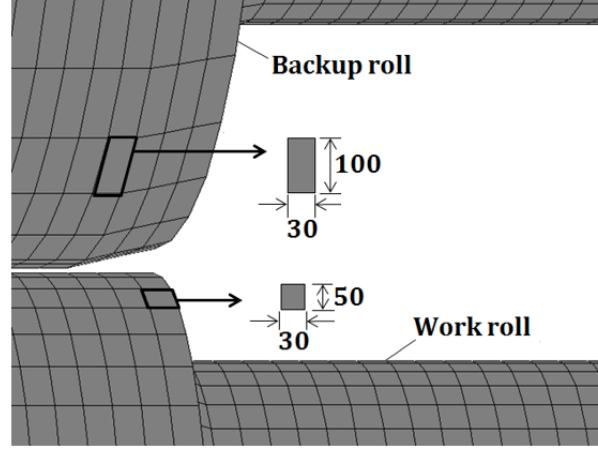


Figure (4-4): FEM mesh for backup roll and work roll

#### 4.4 Stress variation in the work roll during a roll rotation

With the aid of previous roll failures experienced in industries, several critical points can be identified by applying FEM to the entire three-dimensional space of the work roll. As mentioned in the previous section, since the fracture origin is located at the  $r = \text{constant}$  surface [33] [40], the stress amplitude of  $\sigma_r$  is focused and consider where the maximum stress amplitude occurs. Since the stress amplitude is caused by the roll rotation, the stress variation in the  $\theta$ -direction is considered in the work roll. Table (4-4) shows the fundamental roll profile, rolling force and roll dimensions used for the analysis.

Table (4-4): Fundamental roll profile and rolling force considered in Section 4.4

Roll profile (mm)			Rolling	Target
Backup roll	Work roll		force ratio	results
$l_c$	$h_c$	$h_w$	$P/P_{total}$	(MPa)
60	0	0	1.0	Stress $\sigma_r$ , $\sigma_\theta$ , $\sigma_z$
$l_c$ :Chamfer length, $h_c$ :Crown profile, $h_w$ :Wear profile				

#### 4.4.1 Surface stress variation in the $\theta$ -direction the work roll

Figure (4–5) illustrates the line forces  $p_B(z)$  and  $p_S^{ave}$  commonly used in roll industries and also used in this analysis. Along the line  $\theta = 90^\circ$ , the work roll is subjected to the line force  $p_B(z)$  from the backup roll. Along the line  $\theta = 90^\circ$ , the work roll is subjected to the line force  $p_S^{ave}$  from the rolled steel. The line force  $p_S^{ave}$  is insensitive to the work roll's wear profile, but varies in the width direction of the rolled steel due to the temperature. However, since the analysis method is not generalized, in this paper, assume  $p_S^{ave} = \text{constant}$ .

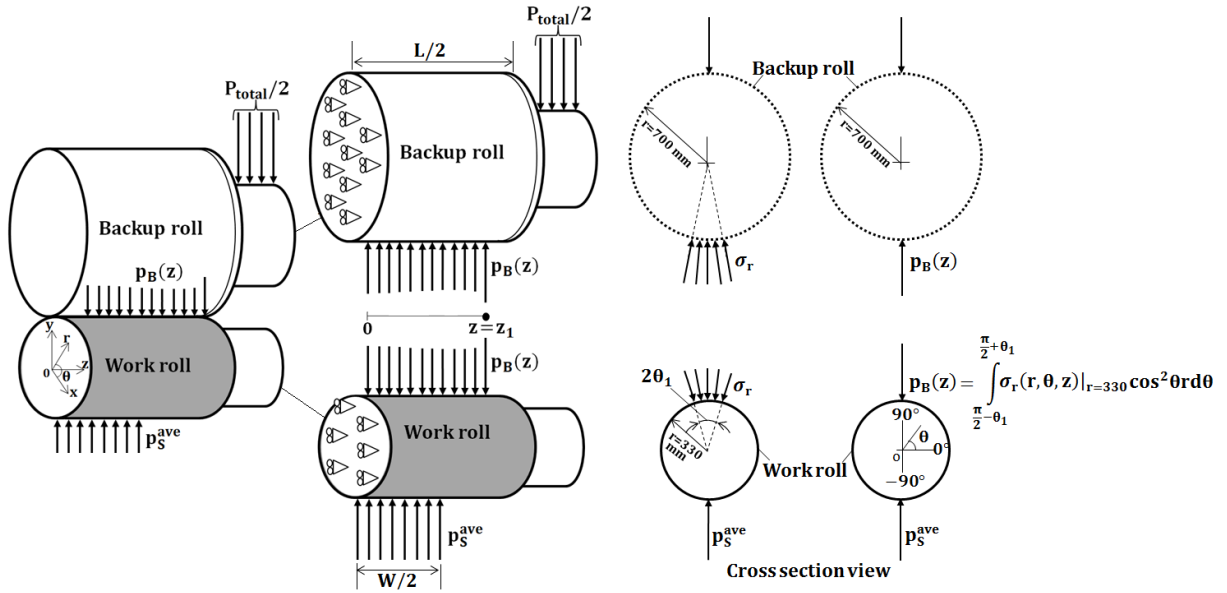


Figure (4–5): Definition of  $p_B(z)$  and  $p_S^{ave}$  due to contact between backup roll and work roll

Figure (4–6), Figure (4–7), and Figure (4–8) show the surface stress variation  $\sigma_r$ ,  $\sigma_\theta$ ,  $\sigma_z$  at  $z = 0$  in the  $\theta$ -direction. The internal stress varies in a similar way in Figure (4–9) as described later (see Figure (4–13) and Figure (4–14)). Figure (4–6) shows that the target stress  $\sigma_r$  takes the maximum compressive stress at  $\theta = -90^\circ$  due to the contact of the rolled steel as well as  $\sigma_\theta$ ,  $\sigma_z$ . Those stresses take the secondary maximum compressive stresses at  $\theta = 90^\circ$  due to the contact of the backup roll. This is because the line force  $p_S^{ave} = P_{total}/W$  from the rolled steel is larger than the line force  $p_B^{ave} = P_{total}/L$  from the

#### 4. Rolling stress and fatigue failure during rolling analysis

---

backup roll since  $W = 1200$  mm is shorter than  $L = 1800$  mm.

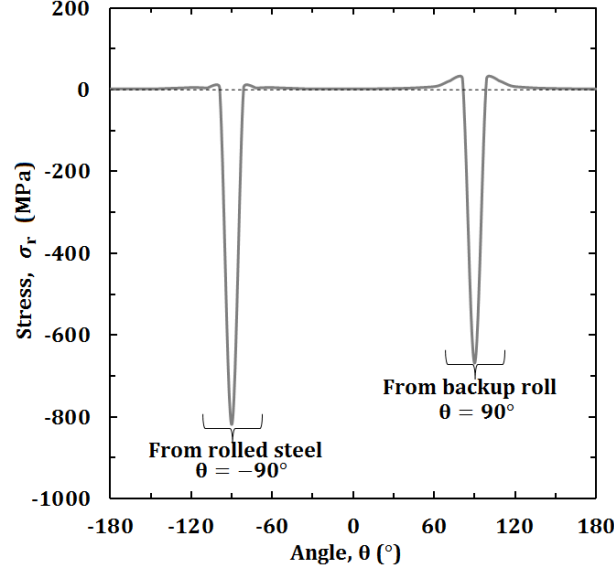


Figure (4-6): Stress distribution  $\sigma_r$  along the roll surface in the  $\theta$ -direction at  $z = 0$

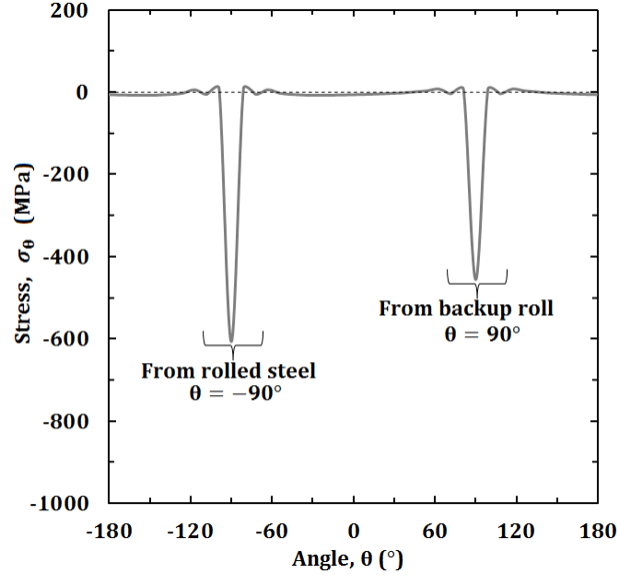


Figure (4-7): Stress distribution  $\sigma_\theta$  along the roll surface in the  $\theta$ -direction at  $z = 0$

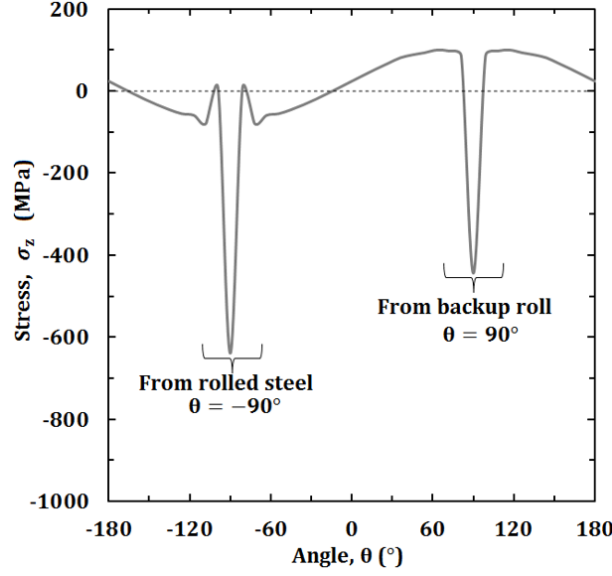


Figure (4-8): Stress distribution  $\sigma_z$  along the roll surface in the  $\theta$ -direction at  $z = 0$

#### 4.4.2 Internal stress variation in the z-direction of the work roll

Figure (4-9) compares the stress distribution at the surface  $r = 330$  mm with the stress distribution at the HSS/DCI boundary  $r = 270$  mm. As illustrated in Figure (4-9), the five lines specified as  $\theta = -90^\circ, -45^\circ, 0^\circ, 45^\circ, 90^\circ$  are focused to compare the stress distributions.

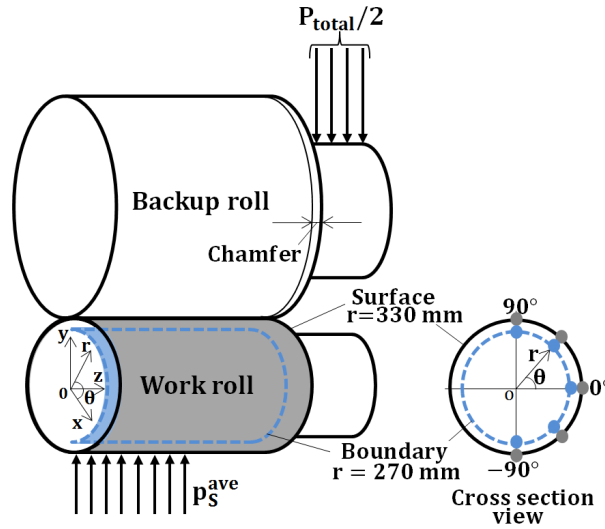


Figure (4-9): Surface and boundary layers in the work roll

#### 4. Rolling stress and fatigue failure during rolling analysis

---

Figure (4–10), Figure (4–11), and Figure (4–12) show the stresses  $\sigma_r$ ,  $\sigma_\theta$ ,  $\sigma_z$  at each angle on the roll surface and HSS/DCI boundary surface. In the previous section, Figure (4–6) showed that the maximum surface compressive stress appears at  $\theta = -90^\circ$  and  $z = 0$ . Regarding the inside stress at the HSS/DCI boundary  $r = 270$  mm, Figure (4–6) indicates that the maximum compressive stress appears at  $\theta = -90^\circ$  and the secondary maximum stress appears at  $\theta = 90^\circ$  similar to the surface stress. The maximum compressive stress  $\sigma_r$  is larger than  $\sigma_\theta$ ,  $\sigma_z$ . Also, since the stress  $\sigma_r$  controls the HSS/DCI boundary fatigue failure as shown in Figure (4–1), in the following discussion we will focus on the stress  $\sigma_r$ .

The compressive stress on the surface  $r = 330$  mm,  $\sigma_r = 817$  MPa is lower than the yield stress 1270 MPa of the outer layer (HSS); and therefore, the yielding condition is not satisfied since  $\sigma_r = 817$  MPa  $<$  1270 MPa with  $\sigma_z < 0$  and  $\sigma_\theta < 0$ . Similarly, the HSS/DCI boundary stress at  $r = 270$  mm  $\sigma_r = 388$  MPa is lower than the yield stress 410 MPa of the inner layer (DCI); and therefore, the yielding condition is not satisfied since  $\sigma_r = 388$  MPa  $<$  410 MPa with  $\sigma_z < 0$  and  $\sigma_\theta < 0$ .

As shown in Figure (4–10), the maximum compressive stress  $\sigma_r$  appears on the surfaces. However, in this study, the HSS/DCI boundary stress is focused because of the following reason. Compared to the backup roll, the work roll surface is frequently ground with a smaller wear amount in order to use the surface repeatedly by removing surface roughness caused by wear during the use. For this reason, surface spalling caused by the crack initiated at the roll surface hardly occurs in work rolls although often occurs in backup rolls. The authors' investigation regarding roll fracture revealed that the work roll surface failure is not caused by normal fatigue but closely related to rolling troubles [33] [12]. Instead, the backup rolls' spalling is caused by the fatigue crack initiated at a few mm depth from the surface. In this failure, the repeated shear stress causing the crack initiation controls the rolling contact fatigue and therefore the backup rolls' spalling. In this way, the fatigue failure of the work roll considered in this paper does not have to consider the largest surface stress and has to focus on the inside stress  $\sigma_r$ .

near the HSS/DCI boundary. Although most of the previous studies treated the backup roll spalling, the failure mechanism is totally different from the one of the inside fatigue failure targeted in this study.

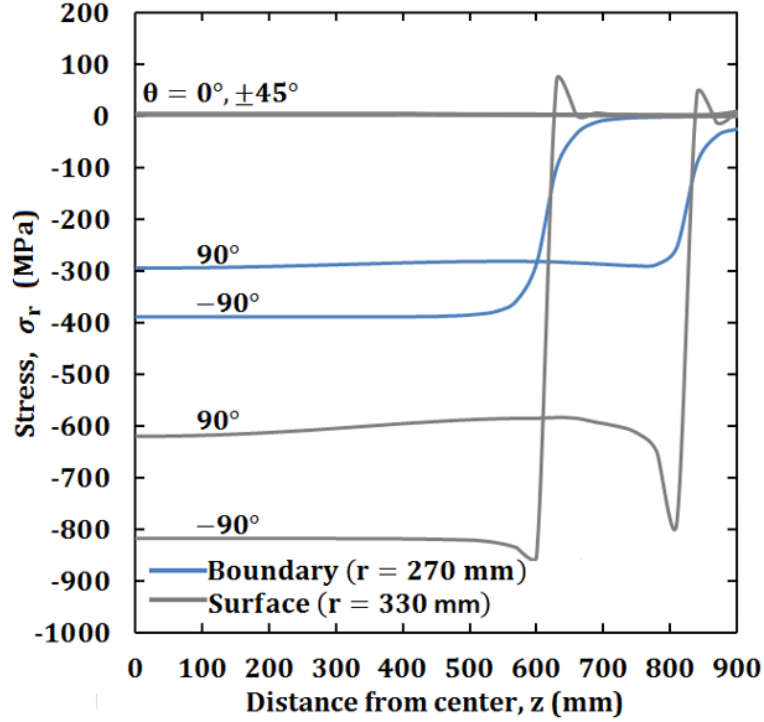


Figure (4-10): Stress  $\sigma_r$  at  $r = 330$  mm and the HSS/DCI boundary  $r = 270$  mm in the  $z$ -direction

#### 4.4.3 Stress variation $\sigma_r$ in the vicinity of HSS/DCI boundary at $\theta = \pm 90^\circ$ of the work roll

Figure (4-13) and Figure (4-14) illustrate  $\sigma_r$  distributions in the range  $255 \leq r \leq 330$  mm including the HSS/DCI boundary  $r = 270$  mm. Figure (4-13) shows  $\sigma_r$  in the longitudinal section  $\theta = 90^\circ$  of the work roll due to the contact  $0 \leq z \leq L/2 = 900$  mm from the backup roll. A peak value of  $\sigma_r$  can be seen near the end of the contact area. Figure (4-14) shows  $\sigma_r$  in the longitudinal section  $\theta = -90^\circ$  of the work roll due to the contact  $0 \leq z \leq W/2 = 600$  mm from the rolled steel. A peak value of  $\sigma_r$  can be seen near the end of the contact area. From the comparison between Figure (4-13) and Figure



#### 4. Rolling stress and fatigue failure during rolling analysis

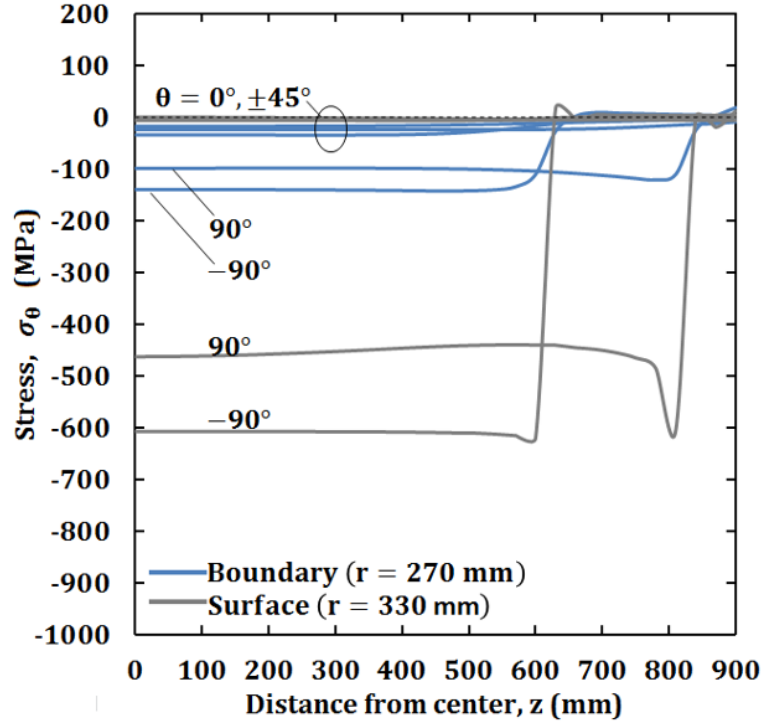


Figure (4-11): Stress  $\sigma_\theta$  at  $r = 330$  mm and the HSS/DCI boundary  $r = 270$  mm in the  $z$ -direction

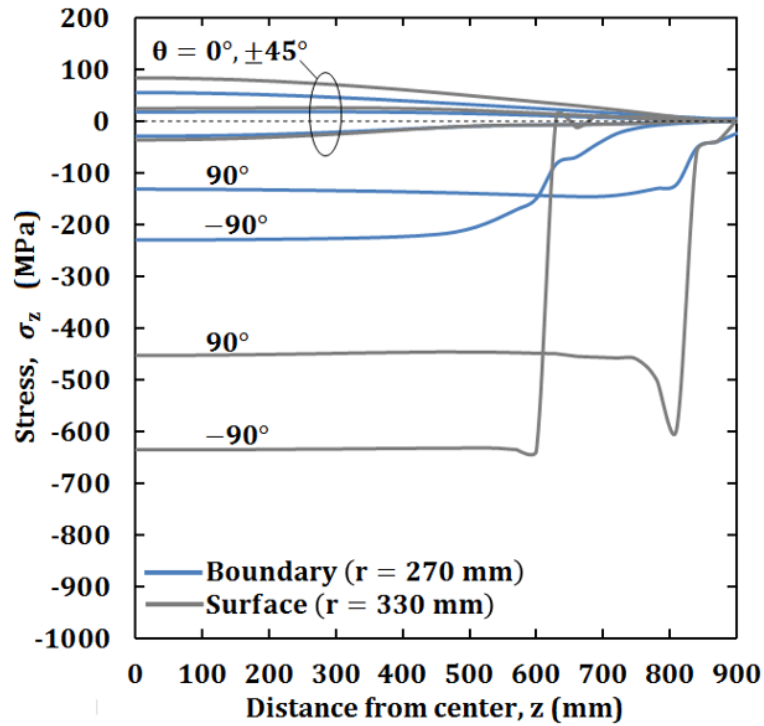


Figure (4-12): Stress  $\sigma_z$  at  $r = 330$  mm and the HSS/DCI boundary  $r = 270$  mm in the  $z$ -direction

#### 4. Rolling stress and fatigue failure during rolling analysis

(4–14),  $\sigma_r$  due to the contact from the rolled steel is larger because the contact length  $W/2 = 600$  mm is smaller than the one of  $L/2 = 900$  mm. The maximum stress position  $\theta = -90^\circ$  for the inside  $\sigma_r$  is equal to the position for the surface  $\sigma_r$ .

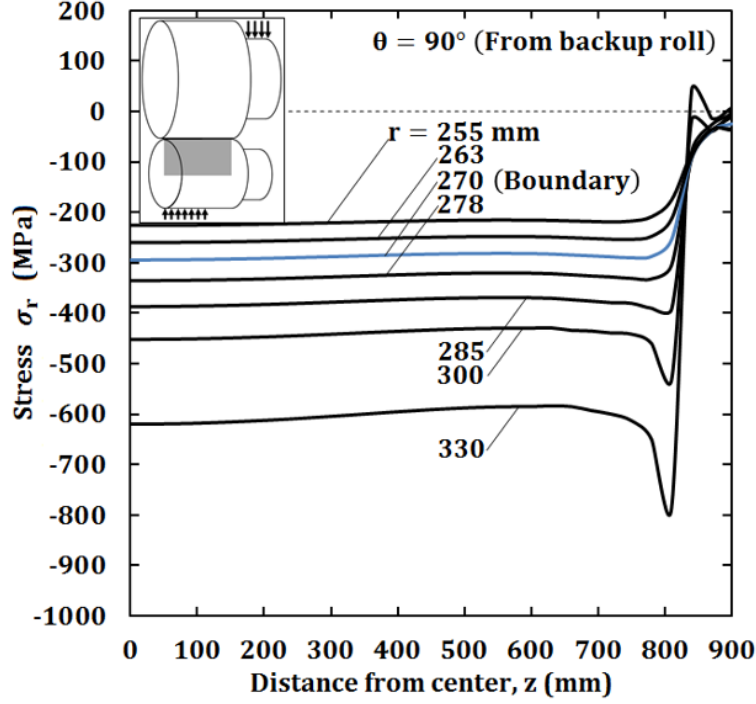


Figure (4–13): Stress  $\sigma_r$  for the contact region between work roll and backup roll

As shown in (4–13) and (4–14), the stress  $\sigma_r$  is largest at the surface; however, as mentioned in the in section 4.2, the surface spalling mainly studied in backup roll previously is not happened in work rolls [41] [42] [43]. Although the crack initiation of the rolling fatigue is mainly controlled by shear stress at a few mm depth of the surface, the fatigue fracture treated in this study starts from the inside the roll near the HSS/DCI boundary. In this failure, the stress amplitude of  $\sigma_r$  near the HSS/DCI boundary controls for the crack initiation and propagation as shown in Figure (4–1). In the following Section 4.5, the rolling condition will be determined to approximate real rolling in the numerical simulation. Then, in Section 4.6, the internal stress  $\sigma_r$  on the HSS/DCI boundary at  $r = 270$  mm will be mainly focused to evaluate the fatigue failure risk, which has not been studied so far.

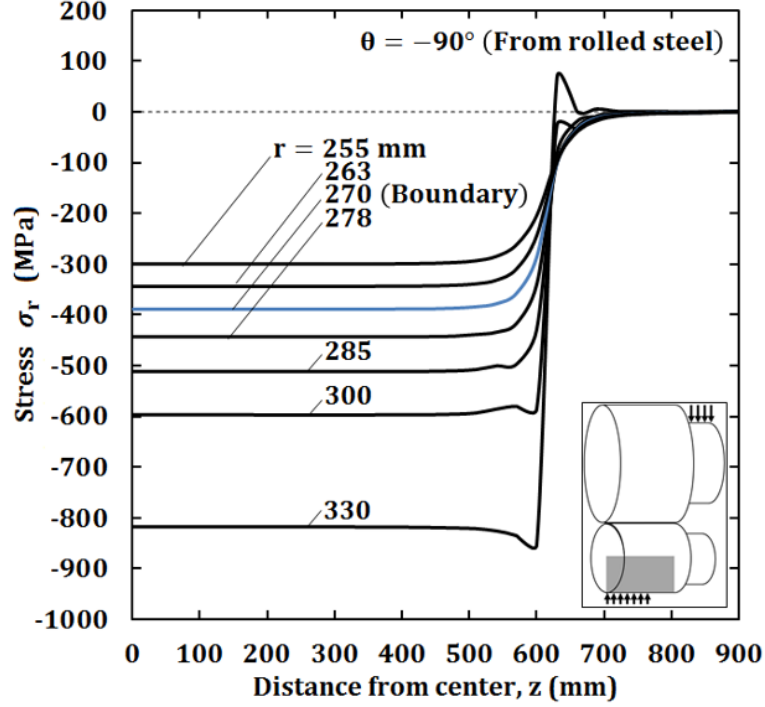


Figure (4-14): Stress  $\sigma_r$  for the contact region between work roll and rolled steel

## 4.5 Effect of chamfer geometry in backup roll and effect of wear profile in work roll

Table (4-5) shows the general roll profile and rolling force to specify the general roll profile. As shown in Table (4-5), the roll chamfer length  $l_c$  is changed as  $l_c = 0 \sim 120$  mm, the crown height  $h_c$  is fixed as  $h_c = 0.5$  mm, and the wear depth  $h_w$  is changed as  $h_w = 0 \sim 0.3$  mm (see Eq. 4-1, Eq. 4-2 and Figure (4-18)). Then, the effect of those geometry on the line force will be discussed.

### 4.5.1 Effect of chamfer geometry in backup roll on the surface shear stress

The line force from the backup roll takes a peak value near the contact end. Therefore, a chamfer is provided to avoid the damage at both roll ends. Figure (4-15) illustrates several chamfer geometries by varying the chamfer length as  $l_c = 0, 30, 60, 90$ , and 120 mm. Figure (4-16) shows the shear stress  $\tau_{rz}$  controlling the crack initiation due to the

#### 4. Rolling stress and fatigue failure during rolling analysis

Table (4-5): General roll profile and rolling force considered in Section 4.5

Roll profile (mm)			Rolling	Target
Backup roll	Work roll		force ratio	results
$l_c$	$h_c$	$h_w$	$P/P_{total}$	(MPa)
0~120	0.5	0~0.3	0.5~1.0	Shear stress $\tau_{rz}$ /Line force $p_B(z)$

$l_c$ :Chamfer length,  $h_c$ :Crown profile,  $h_w$ :Wear profile

rolling contact fatigue at roll end. As mentioned above, in this paper, fatigue failure from the internal HSS/DCI boundary is focused and the shear stress contributing the crack initiation near the surface is not considered. However, to consider the optimum chamfer geometry, in this section, the shear stress is specially discussed. Shear stress  $\tau_{rz}$  can be smallest when  $l_c = 0$ ; however, a certain amount of chamfer  $l_c$  is necessary to avoid collision damage during roll handling. The surface shear stress  $\tau_{rz}$  can be smallest when  $l_c = 30$  mm; however, a larger chamfer length is necessary to reduce work roll bending by introducing the contact at the central portion of the rolls. In this sense, the chamfer length is  $l_c = 60$  mm is chosen for the following analysis.

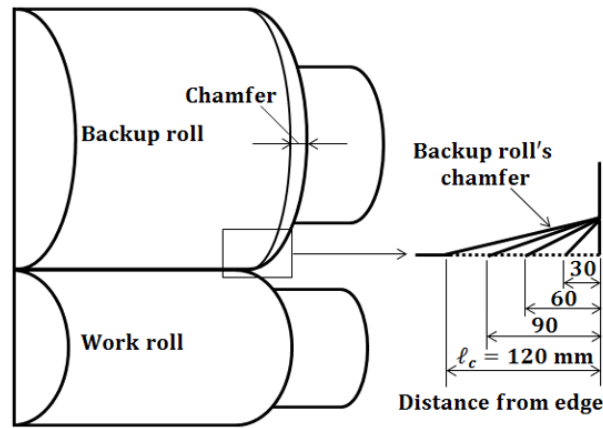


Figure (4-15): Chamfer geometry at the edge of the backup roll when chamfer length  $l_c = 30, 60, 90,$  and  $120$  mm from the edge under  $P/P_{total} = 1.0$

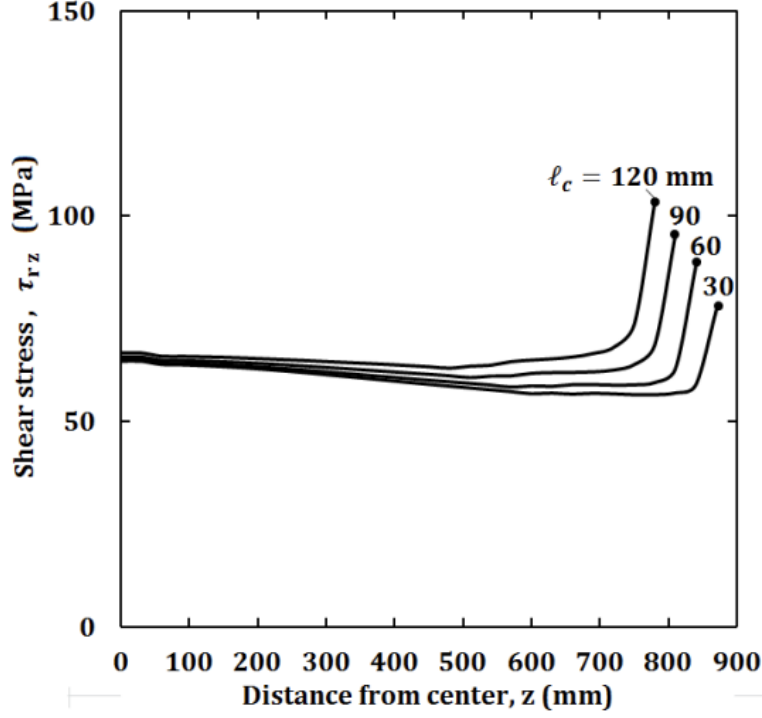


Figure (4-16): Surface shear stress to determine the chamfer geometry on backup roll

#### 4.5.2 Effect of wear profile in work roll on the line force $p_B(z)$

Next, the crown profile  $h_c$  in the backup roll diameter  $D_B(z)$  in Figure (4-2) and the wear profile  $h_w$  in the work roll diameter  $D_W(z)$  will be discussed. Thermal crown caused by the thermal expansion is not considered since thermal deformation is smooth compared to the wear profile and the effect on the line force distribution can be negligible. Therefore, the following Eq.(4-1) and Eq. (4-2) are applied to express the backup roll diameter  $D_B(z)$  with crown height  $h_c$  and the work roll diameter  $D_W(z)$  with the wear amount  $h_w$  (see Figure (4-17)).

$$D_B(z) = 1400 + 2h_c\sqrt{1 - z/l_b} \quad (4-1)$$

$$D_W(z) = 660 - 2h_w\sqrt{1 - z/l_a} \quad (4-2)$$

#### 4. Rolling stress and fatigue failure during rolling analysis

Here,  $l_a$  is the length of the curved part of the work roll, and  $l_b$  is the length of the curved part of the backup roll. Under the basic conditions, the amount of wear  $h_w=0$ . In Eq. (4-2), the wear profile changes slightly at the center of the wear  $z \approx 0$  and changes largely near the wear end of wear  $z \approx l_a$ . The comparison shows Eq. (4-1) coincides with the circular arc shaped backup roll diameter expressed in Eq. (4-3) within 0.12mm.

$$D_B(z) = 1400 + 2h_c - 2 \left[ \frac{(h_c)^2 + (l_b)^2}{2h_c} - \sqrt{\left( \frac{(h_c)^2 + (l_b)^2}{2h_c} \right)^2 - z^2} \right] \quad (4-3)$$

Consider the appropriate amount of crown  $h_c$  used for analysis using Eq. (4-1) and Eq. (4-2). The bending deformation of the backup roll can be calculated from the deflection  $\delta_{z=900}$  at the body end and the deflection  $\delta_{z=0}$  at the body center as  $\Delta\delta = \delta_{z=900} - \delta_{z=0} = 0.2$  mm. The maximum wear profile of the work roll can be estimated as  $h_w = 0.3$  mm. Therefore, the crown amount of the backup roll  $h_c$  should be  $h_c = \Delta\delta + h_w = 0.2$  mm+0.3mm=0.5 mm. Here,  $\Delta\delta = \delta_{z=900} - \delta_{z=0} = 0.2$  mm is the backup roll' s bending deformation and  $h_w = 0.3$  mm is the maximum wear appearing in the work roll.

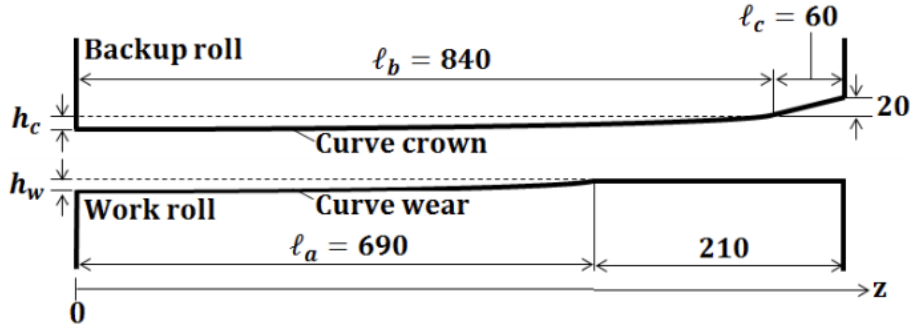


Figure (4-17): Crown profile with height  $h_c$  at the backup roll and wear profile with depth  $h_w$  at the work roll

The line force defined in Eq. 4-4 to Eq. 4-7 are commonly used to express the external force applied to the work roll. In this section, the effect of the wear profile on the line force is clarified for the roll modelling. As shown in Figure (4-18), by varying  $h_w$  the effect of wear profile on the line force  $p_B(z)$  is discussed.

$$p_B(z) = \int_{\frac{\pi}{2}-\theta_1}^{\frac{\pi}{2}+\theta_1} \sigma_r(r, \theta, z)|_{r=330} \cos^2 \theta r d\theta \quad (4-4)$$

Here,  $\theta_1$  is the angle of the contact area shown in Figure (4-5),  $z_1$  is the contact length where  $z_1 = L/2 - l_c$ , and  $\sigma_r|_{r=330}$  is the contact stress on the roll surface ( $r = 330$  mm). The line force  $p_B(z)$  can be defined in Eq. 4-4. And the total rolling force  $P$  can be defined in Eq. 4-5 [44].

$$P = \int_0^{z_1} p_B(z) dz \quad (4-5)$$

The average line forces  $p_B^{ave}$  and  $p_S^{ave}$  is defined in Eq. 4-6 and Eq. 4-7.

$$p_B^{ave} = P/L \quad (4-6)$$

$$p_S^{ave} = P/W \quad (4-7)$$

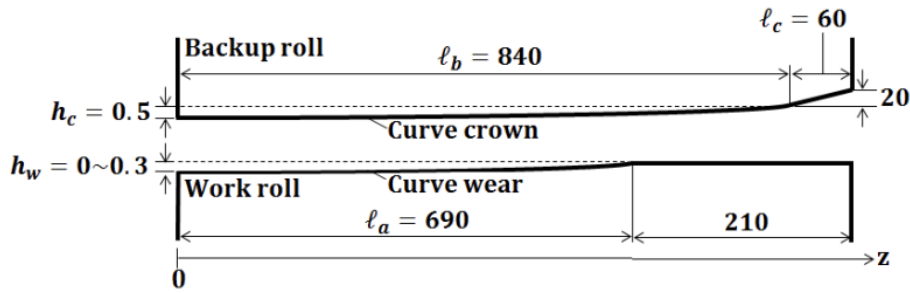


Figure (4-18): Crown profile with fixed  $h_c = 0.5$  mm at the backup roll and wear profile with depth  $h_w = 0 \sim 0.3$  mm at the work roll

Figure (4-19) shows the line force  $p_B(z)$  along the contact area for different wear amount  $h_w$ . Here, the backup roll's crown amount is fixed,  $h_c = 0.5$  mm and the work roll's wear amount is changed as  $h_w = 0, 0.1, 0.2, 0.3$  mm. When the wear profile  $h_w = 0$ ,

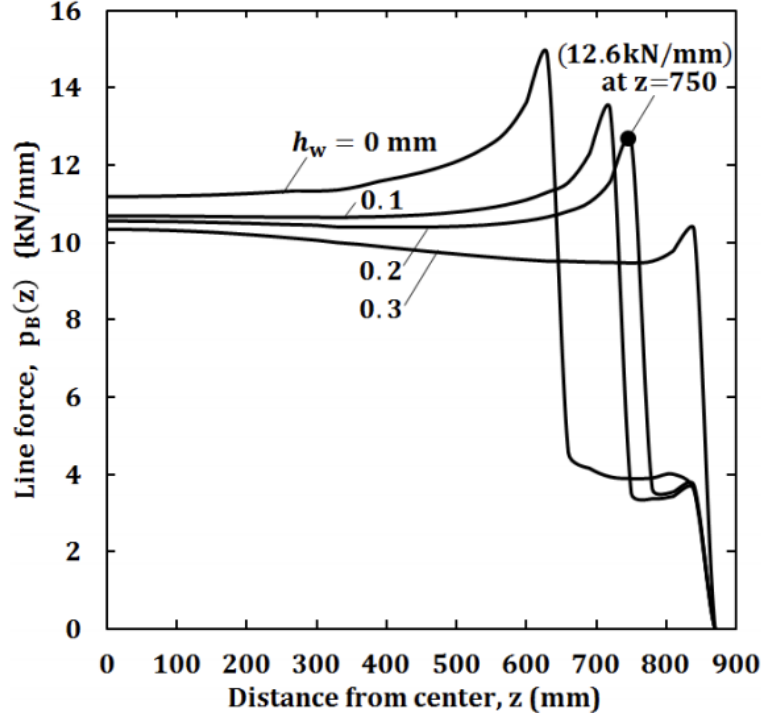


Figure (4-19): Line force  $p_B(z)$  from backup roll when  $h_c$  changes

the line force distribution  $p_B(z)$  is the largest. With increasing  $h_w$ ,  $p_B(z)$  decreases and the largest position moves to the roll end. Point may express the real rolling condition.

Figure (4-20) shows the maximum value of the line force  $p_B(z)$  and the position when the rolling force ratio  $P/P_{total} = 0.5, 1.0, 1.5$ . This is because the standard force  $P/P_{total} = 1.0$  may vary depending on the setting error regarding the rolling material temperature, rolling force, and the impact force at the rolling trouble. As shown in Figure (4-20), with increasing  $h_w$  the maximum line force  $p_B(z)$  decreases. As an example, the position of the peak line force is width  $z = 630$  mm when  $h_w = 0$ . The peak position moves to the roll end. This is because the crown highest is largest at the roll center and gradually decreases toward the end roll. From the above discussion, for the analysis model a relatively large amount of wear amount  $h_w = 0.2$  mm is chosen providing a relatively high maximum line force  $p_B(z)$ .



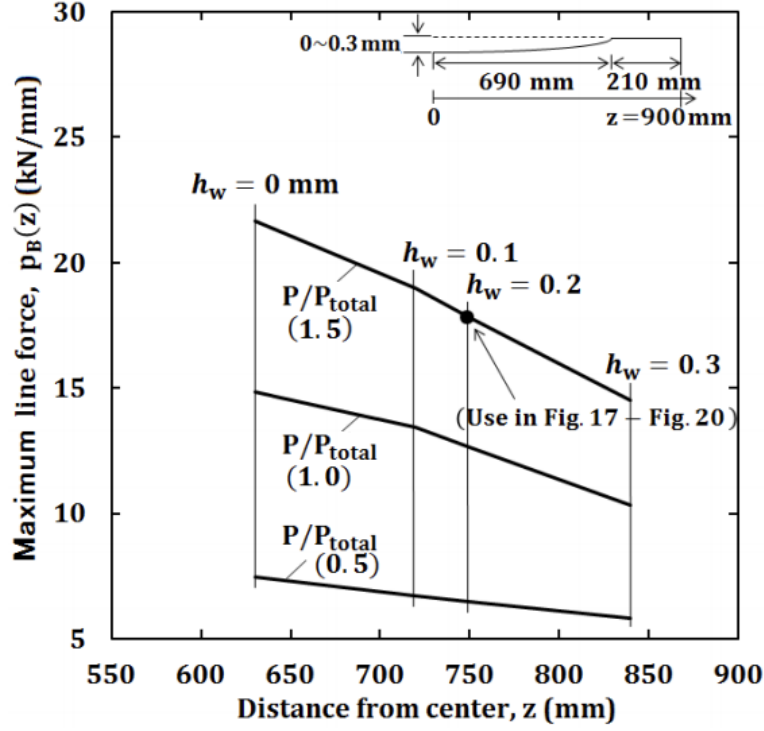


Figure (4-20): Maximum line force  $p_B(z)$  applied from backup roll vs. the position of the maximum line force

#### 4.6 Fatigue risk evaluation of rolls assuming actual rolling

As discussed in the previous section, the followings are assumed for typical roll modelling. Regarding the backup roll, the chamfer length is set to  $l_c = 60$  mm, the crown amount is set to  $h_c = 0.5$  mm. Also, the work roll's wear amount is set to  $h_w = 0.2$  mm. Table (4-6) shows the standard roll profile, rolling force, and target results used in Section 4.6.

Table (4-6): Standard roll profile and rolling force considered in Section 4.6

Roll profile (mm)			Rolling	Target
Backup roll	Work roll		force ratio	results
$l_c$	$h_c$	$h_w$	$P/P_{total}$	(MPa)
60	0.5	0.2	1.5	Stress $\sigma_r$

$l_c$ :Chamfer length,  $h_c$ :Crown profile,  $h_w$ :Wear profile

#### 4. Rolling stress and fatigue failure during rolling analysis

As shown in Table (4-6), although the standard rolling force ratio is  $P/P_{total} = 1.0$ , more severe ratio  $P/P_{total} = 1.5$  is assumed to evaluate the fatigue failure risk when the rolling trouble happens such as the impact force due to the rolling plate biting and the temperature drop of the rolled material.

##### 4.6.1 Analysis of roll' s internal stress

Considering the HSS/DCI boundary failure in Figure (4-1), the fatigue risk will be evaluated at the critical region. The maximum and minimum values of  $\sigma_r$  during a roll rotation is the driving force causing the internal fatigue. Figure (4-21) illustrates critical positions denoted by  $B_{0\sim 900}^{270} |_{\theta=-90^\circ}, B_{0\sim 900}^{270} |_{\theta=90^\circ}, B_{0\sim 900}^{270} |_{\theta=0^\circ}, C_{0\sim 900}^0 |_{\theta=90^\circ}$  and  $C_{0\sim 900}^0 |_{\theta=0^\circ}$ , which are based on the experience. Taking  $B_{0\sim 900}^{270} |_{\theta=90^\circ}$  as an example, superscript 270 represents the HSS/DCI boundary  $r = 270$  mm and subscript  $0 \sim 900$  represents  $z = 0 \sim 900$  mm. At those critical positions, consider the effects of the line force  $p_S^{ave}$  from the rolled steel ( $\theta = -90^\circ$ ) and the line force  $p_B^{ave}$  from the backup roll ( $\theta = 90^\circ$ ). The  $\sigma_r$  variation during a roll rotation can be evaluated from the results at  $B_{0\sim 900}^{270} |_{\theta=-90^\circ}, B_{0\sim 900}^{270} |_{\theta=90^\circ}, B_{0\sim 900}^{270} |_{\theta=0^\circ}, C_{0\sim 900}^0 |_{\theta=90^\circ}$  and  $C_{0\sim 900}^0 |_{\theta=0^\circ}$ .

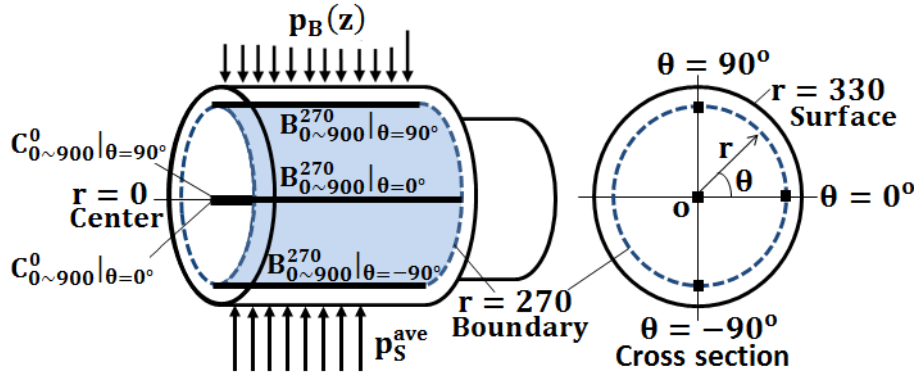


Figure (4-21): Critical position caused by the variation of  $\sigma_r$  in the work roll

Figure (4-22) shows the variation of  $\sigma_r$  in the  $z$ -direction on the HSS/DCI boundary. Along the line  $\theta = 0^\circ$ , the stress  $\sigma_r$  is almost constant and close to zero during  $z = 0 \sim 900$

#### 4. Rolling stress and fatigue failure during rolling analysis

mm. The maximum stress is  $\sigma_{r_{max}}^{\theta=0^\circ} = 4$  MPa at  $z = 0$ .

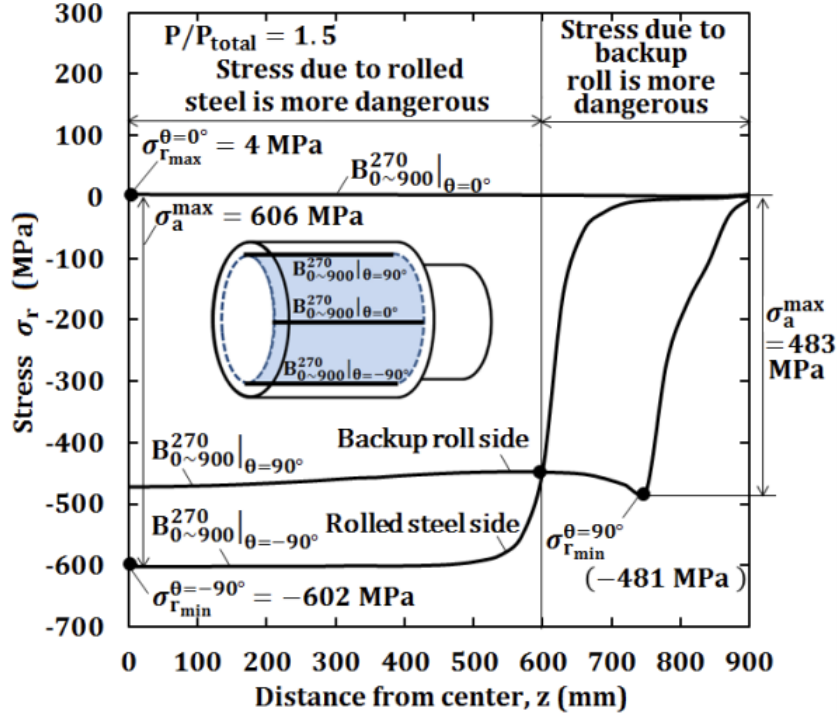


Figure (4-22): Rolling stress  $\sigma_r$  at  $\theta = 0^\circ$ ,  $\theta = 90^\circ$  and  $\theta = -90^\circ$  along  $z$ -direction on the boundary  $r = 270$  mm of the work roll

In Figure (4-22), the stress amplitude  $\sigma_a$  controlling the fatigue fracture during a rotation can be discussed by comparing the results at  $\theta = 0^\circ$ ,  $\theta = 90^\circ$  and  $\theta = -90^\circ$ . A larger stress amplitude  $\sigma_a$  can be provided from the rolled steel side line  $\theta = -90^\circ$  in the range  $0 \leq z \leq 600$  mm. Another larger stress amplitude  $\sigma_a$  the backup roll side line  $\theta = 90^\circ$  in the range  $600 \leq z \leq 900$  mm. Here,  $z = 600$  mm is the intersection of the two stress distributions. The minimum stress from the rolled steel side ( $\theta = -90^\circ$ ) is  $\sigma_{r_{min}}^{\theta=-90^\circ} = -602$  MPa at  $z = 0$ ; and therefore, the maximum stress amplitude is  $\sigma_a^{max} = \sigma_{r_{max}}^{\theta=0^\circ} - \sigma_{r_{min}}^{\theta=-90^\circ} = 606$  MPa. This position  $(r, z) = (270 \text{ mm}, 0)$  is represented by  $B_0^{270}$ . On the other hand, the minimum stress from the backup roll side ( $\theta = 90^\circ$ ) is  $\sigma_{r_{min}}^{\theta=90^\circ} = -481$  MPa at  $z = 750$  mm; and therefore, the maximum stress amplitude is  $\sigma_a^{max} = \sigma_{r_{max}}^{\theta=0^\circ} - \sigma_{r_{min}}^{\theta=-90^\circ} = 483$  MPa. This position  $(r, z) = (270 \text{ mm}, 750 \text{ mm})$  is represented by  $B_{750}^{270}$ .

#### 4. Rolling stress and fatigue failure during rolling analysis

Figure (4–23) shows the stress distribution  $\sigma_r$  over the circumference of the work roll on the HSS/DCI boundary  $r = 270$  mm. At  $z = 0$  denoted by the solid line, the maximum compressive stress  $\sigma_r$  is generated on the rolled steel side and the second maximum compressive stress  $\sigma_r$  is generated on the backup roll side. When  $z = 750$  mm denoted by dotted line, the maximum compressive stress  $\sigma_r$  is generated only on the backup roll side.

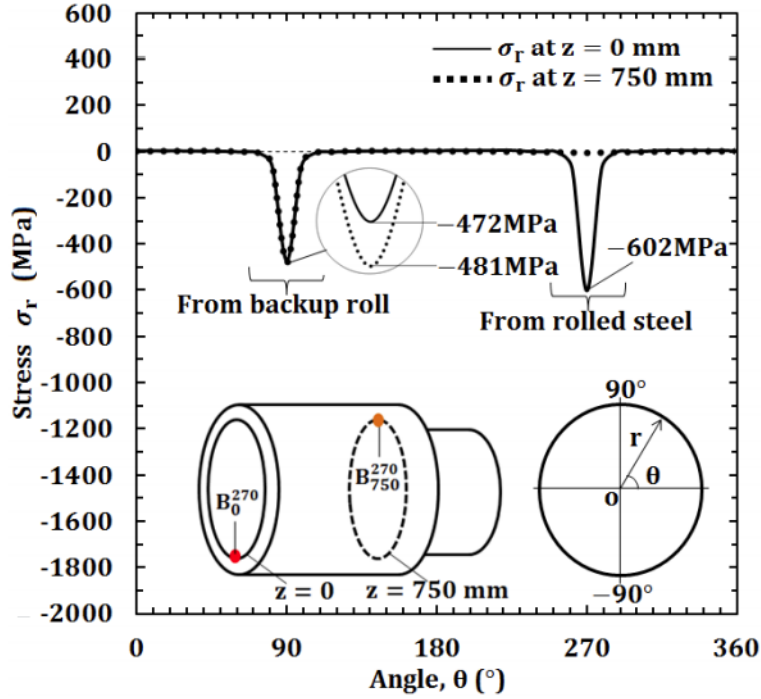


Figure (4–23): Stress distribution  $\sigma_r$  at the boundary along  $\theta$ -direction

Next, considering failure from the roll central portion experienced previously, the stress amplitude at the work roll center  $(r, z) = (0, 0)$  is considered in Figure (4–24). At the center  $(r, z) = (0, 0)$ , maximum tensile stress  $\sigma_{r_{max}}^{\theta=90^\circ} = 46$  MPa, maximum compressive stress  $\sigma_{r_{min}}^{\theta=0^\circ} = -85$  MPa, and maximum stress amplitude  $\sigma_a^{max} = 131$  MPa. The center  $(r, z) = (0, 0)$  is denoted by  $C_0^0$ .

Figure (4–25) illustrates three critical points  $B_0^{270} |_{Rolled\ steel}$ ,  $B_{750}^{270} |_{Backup\ roll}$  and  $C_0^0$ . Results from Figure (4–22) to Figure (4–24) reveal that the three points inside the roll are under the compressive stress field. Therefore, endurance limit diagram under compressive

#### 4. Rolling stress and fatigue failure during rolling analysis

stress will be considered in the next section to evaluate the fatigue failure risk.

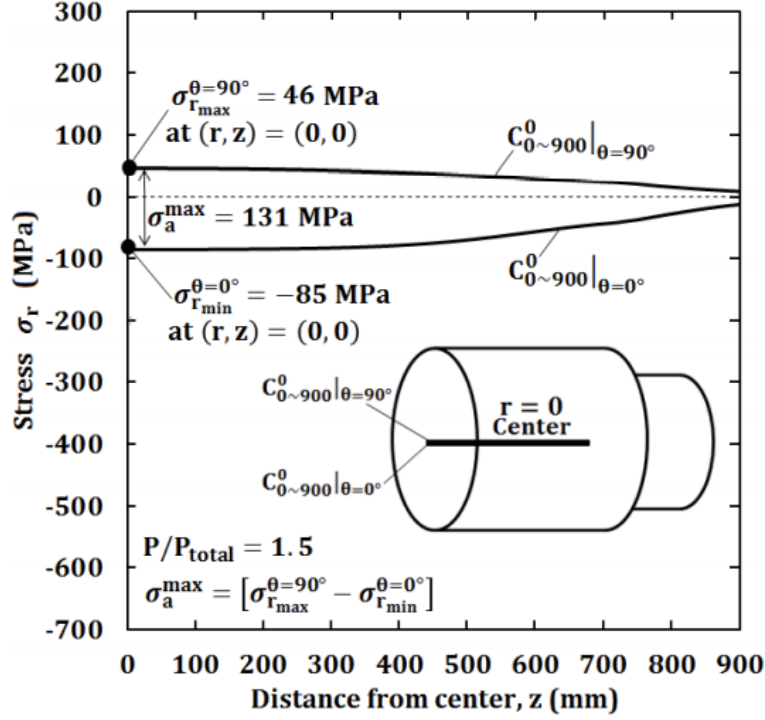


Figure (4-24): Rolling stress  $\sigma_r$  at  $\theta = 0^\circ$  and  $\theta = 90^\circ$  along  $z$ -direction at the work roll center  $r = 0$

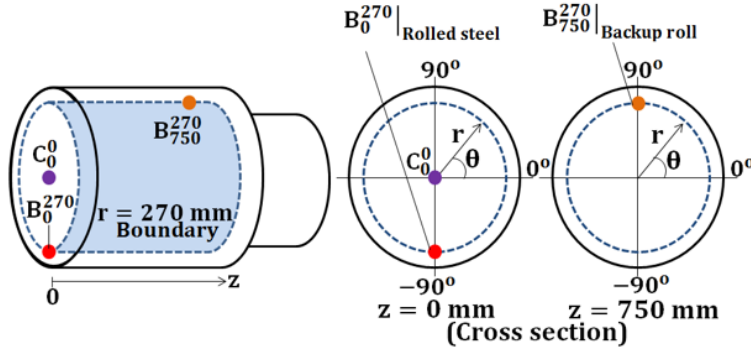


Figure (4-25): Illustration of three critical points denoted by  $B_0^{270} |_{\text{Rolled steel}}$ ,  $B_{750}^{270} |_{\text{Backup roll}}$  and  $C_0^0$

#### 4.7 Fatigue damage under repeated compressive stress

Fatigue failure under large compressive stress was treated by several previous papers but usually they focused on rolling contact fatigue in ball/roller bearings and backup

#### 4. Rolling stress and fatigue failure during rolling analysis

roll surface spalling [45] [46]. In other words, few data are available for ordinary fatigue strength under large compressive stress fields [2]. Only the followings are known for the fatigue life under the compressive mean stress [47] [48] [49]. Figure (4–26) illustrates three types of compressive alternative loading under the mean stress  $\sigma_m < 0$ . Figure (4–26)a shows  $\sigma_a + \sigma_m = \sigma_{max} > 0$ , Figure (4–26)b shows  $\sigma_a + \sigma_m = \sigma_{max} = 0$  and Figure (4–26)c shows  $\sigma_a + \sigma_m = \sigma_{max} < 0$ . Considering that the fatigue life consists of a crack initiation period, crack growth period, and finally ultimate failure, the followings are known.

1. During the crack initiation stage, the fatigue life is controlled by the stress amplitude irrespective of the mean stress, positive or negative. Under the fixed stress amplitude as shown in Figure (4–26)a to (4–26)c, the crack initiates at the same time [47].
2. Instead, during the crack growth stage, with decreasing the mean stress, the crack growth rate decreases sensitively and the fatigue life increases significantly. It is known that under  $\sigma_{max} = 0$  in Figure (4–26)b and  $\sigma_{max} < 0$  in Figure (4–26)c, the crack does not propagate and no final failure [47] [48].
3. However, under  $\sigma_{max} > 0$  in Figure (4–26)a, the amount of tensile stress  $\sigma_{max} = \sigma_a + \sigma_m > 0$  necessary for the final failure is not known because it has not been discussed yet until now. It must vary depending on the magnitude of  $\sigma_m < 0$ .

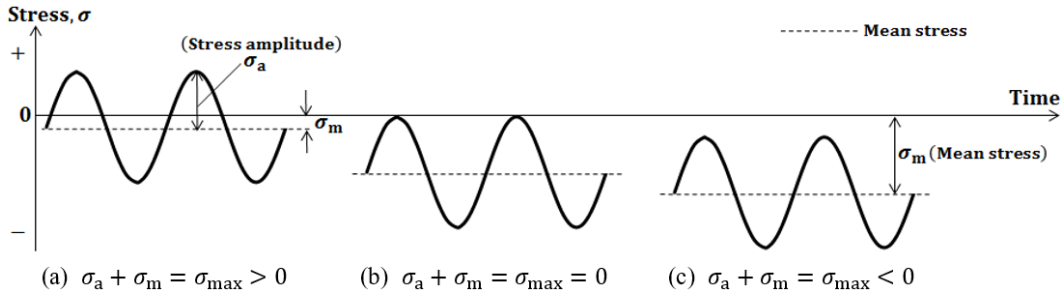


Figure (4–26): Three types of compressive alternative loading where the mean stress  $\sigma_m < 0$

## 4.8 Stress amplitude vs mean stress diagram for compressive mean stress

Considering this situation, the endurance limit lines are newly prescribed under large compressive stress since no studies can be seen. Figure (4–26) shows a stress amplitude versus mean stress diagram ( $\sigma_a$ - $\sigma_m$  diagram) to discuss the fatigue limit under large compressive alternative loading  $\sigma_m \leq 0$ . First of all, assume the amount of the ultimate tensile strength  $\sigma_B$  can be applied to the compressive stress  $\sigma_m < 0$  and alternative stress  $\sigma_a > 0$ . They can be expressed in Eq. (4–8).

$$|\sigma_m| < \sigma_B, |\sigma_m| < \sigma_B \quad (4-8)$$

Assume the so-called modified Goodman law defined in Eq. (4–9) for

$$\sigma_m \geq 0.$$

$$\frac{\sigma_a}{\sigma_{w0}} + \frac{\sigma_m}{\sigma_B} \leq 1 \quad (4-9)$$

The limit line  $\sigma_a/\sigma_{w0} + \sigma_m/\sigma_B = 1$  can be extended to the negative region  $\sigma_m < 0$  [50]. Consider pulsating compressive loading  $\sigma_a + \sigma_m = \sigma_{max} = 0$  in Figure (4–26)b. In Figure (4–27)a, the line is indicated as  $\sigma_m = -\sigma_a$  denoted by a dotted line with the angle of  $\theta = 45^\circ$  from the ordinate from the origin. As described above, no fatigue final failure happens in the region described by Eq. (4–10).

$$\sigma_a + \sigma_m = \sigma_{max} \leq 0 \quad (4-10)$$

Denote the intersection  $\sigma_a/\sigma_{w0} + \sigma_m/\sigma_B = 1$  and  $\sigma_a + \sigma_m = \sigma_{max} = 0$  as point E (Figure (4–27)a). Since point E satisfies Eq. (4–10), there is no final fracture. Therefore, consider point F and point F' by adding a certain amount of positive tensile stress to

#### 4. Rolling stress and fatigue failure during rolling analysis

---

point E. Those point F and point F' can be the fatigue limit below which no final failure [51]. Consider fully reversible fatigue limit at point D (see Figure (4-27)b) where the maximum tensile stress  $\sigma_r = 166$  MPa and the maximum compressive stress  $\sigma_r = 166$  MPa are applied. Instead, at point E, the maximum compressive stress  $\sigma_r = 0$  but the maximum compressive stress  $\sigma_r = 554$  MPa is more than three times larger than the compressive stress of point D  $\sigma_r = 166$  MPa as  $\sigma_r = 554$  MPa =  $277 \text{ MPa} \times 2 > 166 \text{ MPa} \times 3 = 498 \text{ MPa}$ . Therefore, more severe damage is accumulated at point E compared to point D.

Consider F' where the same maximum tensile stress  $\sigma_r = 332$  MPa. Due to the larger compressive stress  $\sigma_r = 554$  MPa compared to the one  $\sigma_r = 166$  MPa at the point D, the tensile stress necessary for the fatigue limit can be smaller than  $\sigma_r = 332$  MPa, which is the same as the tensile stress at point D. At point E, however, because of no tensile stress, no final failure as the previous studies indicated [47] [48] [49]. In this way, the fatigue limit point F should be between point D and point F'. Therefore, assume half value  $\sigma_{w0}/2 = 83$  MPa for this tensile stress at point F as shown in Figure (4-27)d. By drawing the line through point D and point F in Figure (4-27)a, the fatigue limit can be estimated. The range can be expressed by the following equation.

$$\sigma_a \leq -\frac{\sigma_B + \sigma_{w0}}{2\sigma_B} \sigma_m + \sigma_{w0} \quad (4-11)$$

For large compressive alternative loading, the fatigue limit is determined from Eq. (4-8) to Eq. (4-11), which is expressed by the thick solid lines passing through points A, D, F, G, H in Figure (4-27)a. Figure (4-27)a shows the three critical points' results  $B_0^{270} |_{\text{Rolled steel}}$ ,  $B_{750}^{270} |_{\text{Backup roll}}$  and  $C_0^0$ . The fatigue risk at the point  $C_0^0$  is small because of the residual stress and the material defects are not taken into consideration.

Table (4-7) shows the safety factor evaluation defined as  $SF = \overline{OB'}/\overline{OB}$  in Figure (4-27)e. A larger SF value means the point is relatively safer than another point having a smaller SF value. Therefore, the safety factor SF can be used to evaluate the risk of



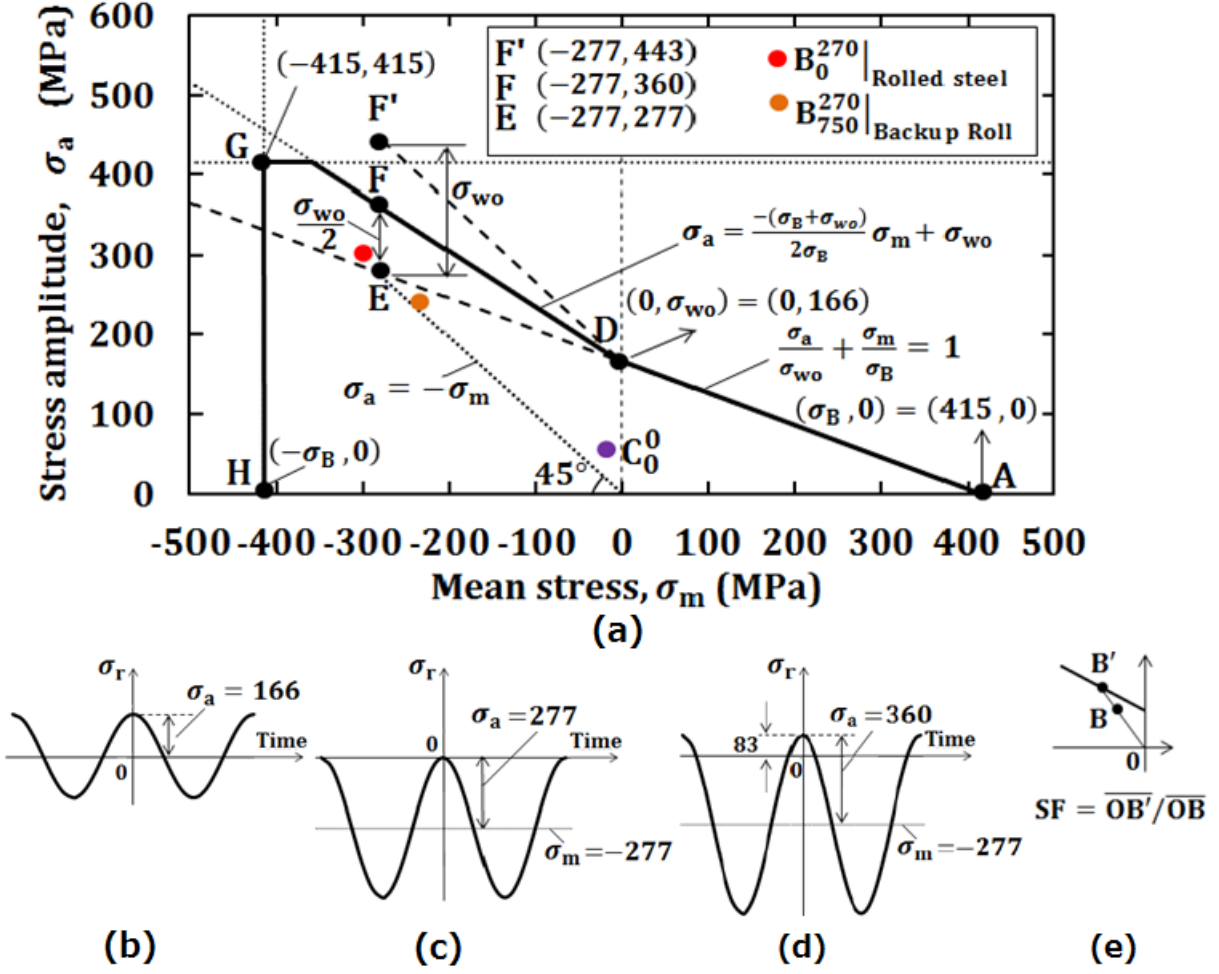


Figure (4-27): (a) Fatigue limit diagram to evaluate three critical points, (b) Stress at point D, (c) Stress at point E, (d) Stress at point F, (e) Safety factor definition

fatigue failure relatively. Although the safety factor  $SF \geq 1$ ,  $B_0^{270} |_{Rolled\ steel}$  is relatively more dangerous than  $B_{750}^{270} |_{Backup\ roll}$  and  $C_0^0$ . The results showed that the fatigue crack initiation around points  $B_0^{270}$  and  $B_{750}^{270}$  on the HSS/DCI boundary may contribute to several roll failures previously occurred.

## 4.9 Conclusion for Chapter 4

In the previous roll failure studies, the surface spalling caused by the crack initiated at the roll surface has been focused in backup rolls because the work roll surface is frequently ground to use the surface repeatedly by removing surface roughness. Since no study is

#### 4. Rolling stress and fatigue failure during rolling analysis

Table (4-7): Mean stress, stress amplitude and safety factor evaluation at  $B_0^{270}$ ,  $B_{750}^{270}$  and  $C_0^0$

All points on the circle	$\sigma_{r_{max}}$ (MPa)	$\sigma_{r_{min}}$ (MPa)	$\sigma_m$ (MPa)	$\sigma_a$ (MPa)	Safety factor
$B_0^{270}$	4	-602	-299	303	1.77
$B_{750}^{270}$	2	-486	-242	244	2.23
$C_0^0$	47	-85	-19	66	3.14

available, in this study, the HSS/DCI boundary stress is clarified during the use in 4-high rolling mill. To clarify the mechanical stress, no residual stress is assumed in the work roll. This study assumed the following rolling conditions that can be regarded as the average values in present steelworks [34], where the work roll diameter  $D_W = 660$  mm with the length  $L = 1800$  mm, the high chrome steel backup roll diameter of  $D_B = 1400$  mm with the length  $L = 1800$  mm, the width of the rolled steel  $W = 1200$  mm and the standard rolling force  $P_{total} = 16400$  kN [34] [35]. The conclusions obtained can be summarized in the following way.

1. No study is available regarding the fatigue limit under compressive mean stress region, stress amplitude versus mean stress diagram is newly considered. Then, a fatigue limit line was proposed under large compressive stress by considering the final failure never occurs at the pulsating compressive loading state.
2. Considering the whole roll geometry, three critical points were chosen on the basis of the analysis and experience. It may be concluded that the most critical point is located at the HSS/DCI boundary point  $B_0^{270}$  where  $(r, z) = (270 \text{ mm}, 0)$  because the largest stress amplitude is caused from the rolling steel. Another critical point is located at  $B_{750}^{270}$  where  $(r, z) = (270 \text{ mm}, 750 \text{ mm})$  due to the backup roll contact.
3. The fatigue failure risk was discussed through the relative safety factor SF. The results showed that the fatigue crack initiation around points  $B_0^{270}$  and  $B_{750}^{270}$  on the HSS/DCI boundary may contribute to several roll failures previously occurred in

#### 4. Rolling stress and fatigue failure during rolling analysis

---

industries.

## 5 Actual stress and fatigue failure during consecutive rolling analysis

### 5.1 Introduction

Since the residual stress is absolutely necessary as a rolling force factor, in this chapter, a three-dimensional finite element method is applied to investigate the residual stress and the rolling stress of the bimetallic work roll in the four-high rolling mill. The residual stress is analyzed by considering pre-heating, quenching, and tempering. By using the results as an initial condition, the rolling stress analysis is performed consecutively.

The generated rolling stress  $\sigma_r$  will be clarified. Then, the risk of internal fatigue fracture will be discussed by considering the fatigue of the roll material by focusing on some critical points empirically known. Since the consecutive FEM analysis considering each roll rotation is time-consuming, the simple evaluation method will be discussed by superposing the residual stress and the rolling stress. The fatigue failure evaluation at center point will also be clarified by considering material defect.

### 5.2 FEM modelling and fundamental dimension and condition of the work roll and backup roll

As mentioned in introduction, the roll residual stress is considered as an initial condition. Then, the rolling stress analysis is performed. Since the detail of the residual stress analysis is indicated in Chapter 2 and Chapter 3, this section mainly focuses on the method of rolling stress analysis by the consecutive FEM analysis.

Figure (5-1) shows the three dimensional model for four-high rolling mill. Table (5-1) shows the roll dimensions used in this consecutive FEM analysis. As shown in Figure (5-1), the work roll diameter is  $D_W = 660$  mm, the backup roll diameter is  $D_B = 1400$  mm, and the body length for both work roll and backup roll is  $L = 1800$  mm. The width

## 5. Actual stress and fatigue failure during consecutive rolling analysis

of the rolled steel is  $W = 1200$  mm. The work roll as well as the backup roll are subjected to the total rolling force  $P_{total}$  whose standard value is  $P_{total} = 16400$  kN [34] [35]. Then, the work roll is subjected to the line force  $p_S^{ave} = P_{total}/W$  from the rolled steel. Also, the work roll is subjected to the line force  $p_B^{ave} = P_{total}/L$  from the backup roll.

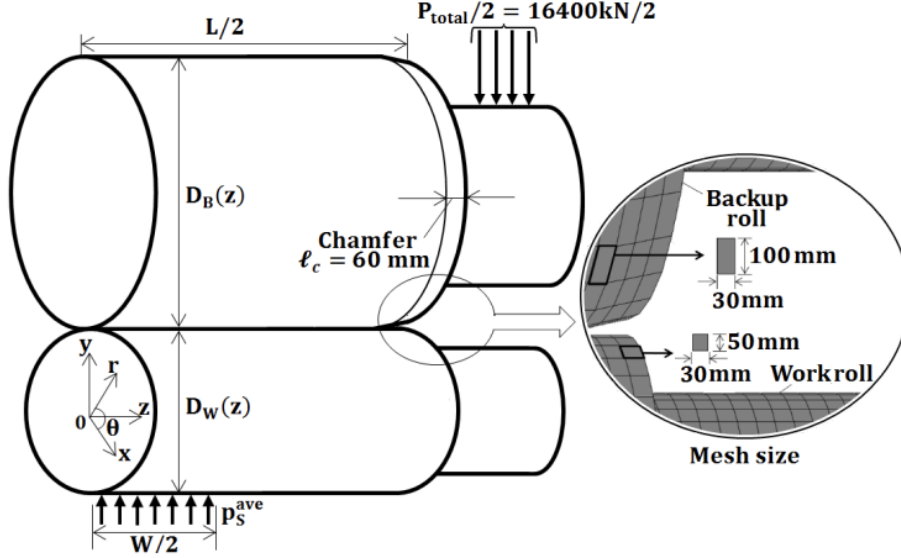


Figure (5–1): 3D FEM model of four-high rolling mill and the roll dimensions used for the consecutive FEM analysis

Table (5-1): Rolling size and condition (Base value)

Size	Work roll	Backup roll	Rolled steel
Diameter (mm)	$D_W=660$	$D_B=1400$	-
Length/Width (mm)	$L = 1800$	$L = 1800$	$W = 1200$
Rolling force, $P_{total}$ (kN)	16400		
Line force, $p_B^{ave}$ from Backup roll (kN/mm) $P_{total}$ (kN)	$P_{total}/L=9.11$		
Line force, $p_S^{ave}$ from Rolled steel (kN/mm) $P_{total}$ (kN)	$P_{total}/W=13.67$		

Figure (5–2) illustrates the line forces  $p_B(z)$  and  $p_S^{ave}$  commonly used in roll industries

## 5. Actual stress and fatigue failure during consecutive rolling analysis

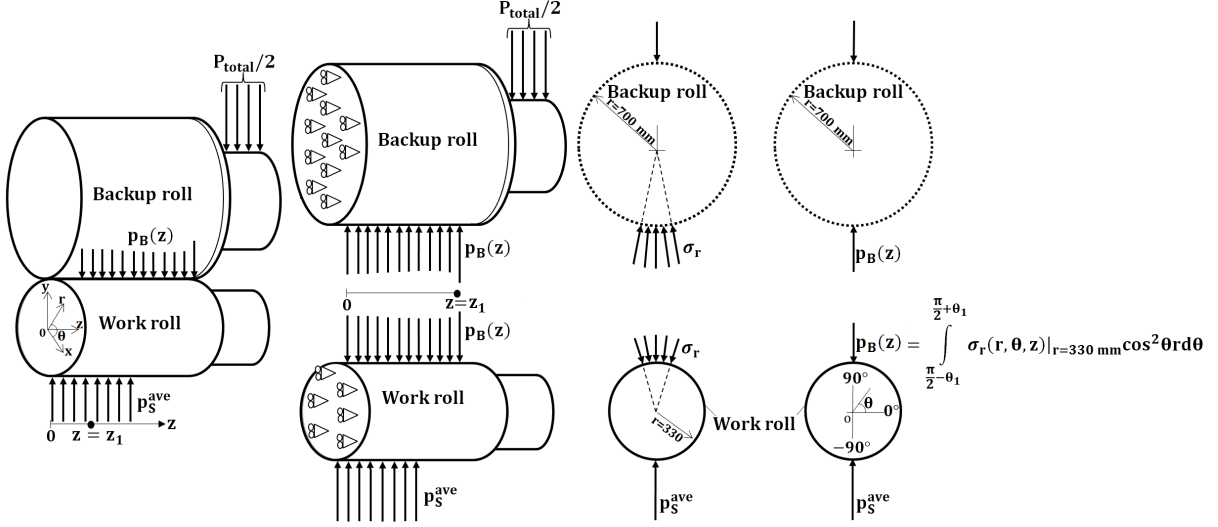


Figure (5-2): Definition of  $p_B(z)$  and  $p_S^{ave}$  due to contact between backup roll and work roll

and also used in this analysis. Along the line  $\theta = 90^\circ$ , the work roll is subjected to the line force  $p_B(z)$  from the backup roll. Along the line  $\theta = -90^\circ$ , the work roll is subjected to the line force  $p_S^{ave}$  from the rolled steel. The line force  $p_S^{ave}$  is insensitive to the work roll's wear profile, but varies in the width direction of the rolled steel due to the temperature. However, since the analysis method is not generalized, in this paper, assume  $p_S^{ave} = \text{constant}$ . The line force  $p_B(z)$  in Figure (5-2), can be expressed by

$$p_B(z) = \int_{\frac{\pi}{2}-\theta_1}^{\frac{\pi}{2}+\theta_1} \sigma_r(r, \theta, z)|_{r=330} \cos^2 \theta r d\theta \quad (5-1)$$

As shown in Figure (5-2), the rolling stress of the work roll is affected by the roll profiles [36] [52]. These roll profiles include the backup roll's chamfer, the backup roll's crown, and the work roll's wear profile. Figure (5-3) illustrates the backup roll's crown profile with  $h_c = 0.5$  mm and the work roll's wear profile with  $h_w = 0.2$  mm. In this analysis, Eq. (5-2) is assumed to express the backup roll's crown and Eq. (5-3) is assumed to express the work roll's wear crown. The length of the curved part of the work roll is denoted as  $l_a$  and the length of the curved part of the backup roll is denoted as  $l_b$  (see Figure (5-3)).

$$D_B(z) = 1400 + 2h_c\sqrt{1 - z/l_b} \quad (5-2)$$

$$D_B(z) = 660 - 2h_w\sqrt{1 - z/l_a} \quad (5-3)$$

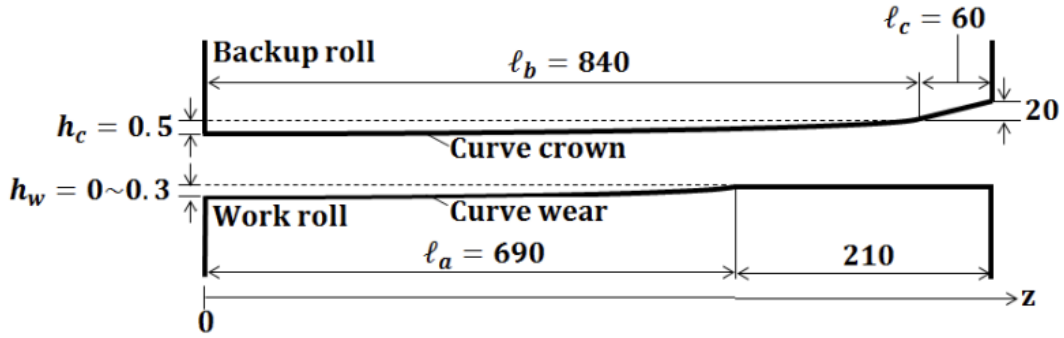


Figure (5-3): Crown profile with fixed  $h_c = 0.5$  mm at the backup roll and wear profile with depth  $h_w = 0 \sim 0.3$  mm at the work roll

Due to the contact with the work roll, the backup roll's deformation causes different deflections at  $z=0$  and  $z=900$  mm, which can be expressed as  $\delta_{z=900} - \delta_{z=0} = 0.2$  mm. Also, the maximum wear appearing on the work roll can be estimated as  $h_w = 0.3$  mm. By considering those profiles, the backup roll's crown is set as  $h_c = 0.5$  mm ( $=0.2$  mm+ $0.3$  mm).

Table (5-2) shows the material properties of the rolls used in the analysis [37]. High-chrome steel is used for the backup roll, high-speed steel (HSS) is used for the outer layer of the work roll, and ductile casting iron (DCI) is used for the inner layer of the work roll. The outer layer HSS has a thickness of 60 mm ( $r = 270 \sim 330$  mm).

The previous studies showed that during one roll rotation, the thermal stress appears due to the heating and cooling of the hot plate (rolled steel) affecting only a few  $\mu\text{m} \sim 1$  mm depth from the surface and does not affect the stress near the boundary [6] [39] [38]. After the rolling starts, the roll temperature increases and become stable after 1 hour and

## 5. Actual stress and fatigue failure during consecutive rolling analysis

Table (5-2): Mechanical properties of the shell and core at room temperature

Property	HSS	DCI	Backup Roll
0.2% proof stress (MPa)	1270	410	-
Tensile strength (MPa)	1575	415	1575
Fatigue strength (MPa)	630	166	630
Yield strength (MPa)	1270	410	-
Young' s modulus (GPa)	230	174	210
Poisson' s ratio	0.3	0.28	0.3
Density (kg/m <sup>3</sup> )	7600	7300	7800

reaches an equilibrium temperature of about 50°C~80°C [12] [20]. Therefore, the effect of the thermal stress can be ignored when considering fatigue fracture in this study, and the analysis is performed at room temperature. Figure (5–4) shows stress-strain diagrams of both the HSS layer and the DCI layer of the work roll at room temperature.

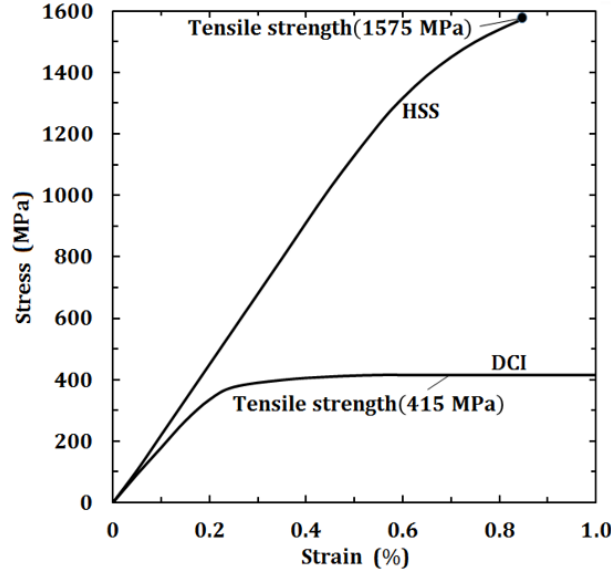


Figure (5–4): Stress-strain relations for HSS and DCI

The software MSC Marc/Mentat 2012 is used to perform the three-dimensional elastic-plastic analysis. Since it is not clear whether plastic deformation occurs with respect to



## 5. Actual stress and fatigue failure during consecutive rolling analysis

---

the internal stress of the work roll, elastic-plastic analysis was used in this analysis. Figure (5–5) shows the FEM analysis model. The minimum mesh is 30 mm x 30 mm x 30 mm and the element types used are 4-node tetrahedral element type and 8-node hexahedral element type at the stress concentration part. The number of nodes is 23,883 and the number of elements is 21,410. The direct constrain method is used for contact analysis between work roll and backup roll.

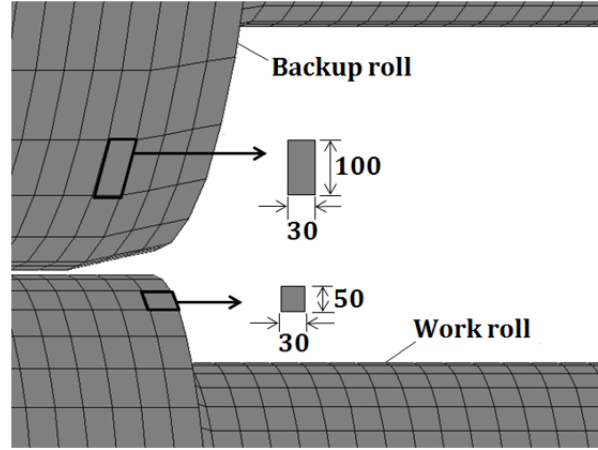


Figure (5–5): FEM mesh for backup roll and work roll

### 5.3 Residual stress as the initial condition to the rolling stress analysis

In this study, the roll residual stress is considered as an initial condition of the rolling stress analysis. Since the detail of the residual stress analysis is indicated in the previous paper [18] [28] [29], this section shows the outline of the residual stress analysis method. Figure (5–6) illustrates the surface temperature history of the bimetallic work roll during heat treatment consisting of the pre-heating, quenching, and tempering. In pre-heating process, the whole roll is heated up to the uniform temperature of  $T_{Start} = 1050^{\circ}\text{C}$  and kept for several hours. Then, the roll temperature drops rapidly through air cooling. After that, the roll is put into the furnace again and maintained at  $T_{Q,Keep}$  to prevent excessive

## 5. Actual stress and fatigue failure during consecutive rolling analysis

---

thermal stresses caused by rapid cooling. After keeping period, the roll is cooled down slowly until to the temperature of  $T_{T,Finish}$ . After the quenching process, the tempering process will be performed 2 times to release the residual stress and obtained the stable microstructure. After this process, the generated residual stress is used as an initial condition for the consecutive FEM analysis of the rolling analysis.

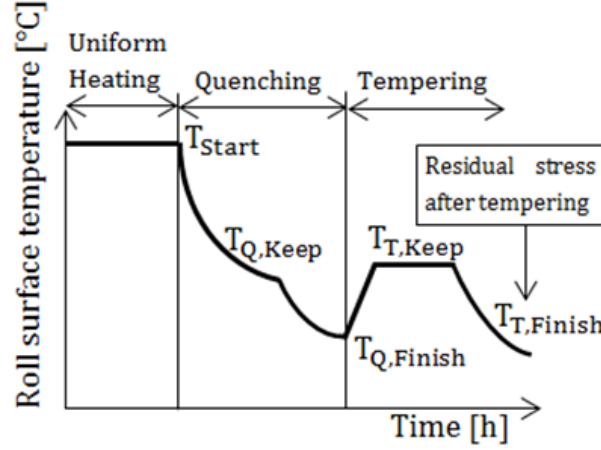


Figure (5–6): Heating, quenching, and tempering treatment of the bimetallic work roll

Figure (5–7) shows the residual stresses  $\sigma_r, \sigma_\theta$ , and  $\sigma_z$  at boundary  $r = 270$  mm along  $z$ -direction after the heating treatment. The tensile stress  $\sigma_r$  is almost constant along the  $z$ -direction and it may cause the boundary debonding. Figure (5–8) shows an example of the boundary failure considered in this paper. As shown in Figure 7(a), a semi-elliptical beach mark can be clearly seen near the boundary at point A, which shows that the fatigue crack initiates at the inner boundary point A and propagates to the surface [33]. Roll maker companies also identified that sometimes similar failure can be seen near the end of the roll body (see point  $B_{750}^{270}$  in Figure 5-10). Such peeling shown in Figure (5–8) is caused by the radial stress  $\sigma_r$  variation during the roll rotation [33]. In this thesis, this internal fatigue failure caused by  $\sigma_r$  will be studied since the previous papers only focused on the surface spalling in backup rolls [41] [43] [53] [42] [54]. This surface failure starts from several mm inside from the surface caused by the shear stress under rolling fatigue is very different from the failures in Figure 7 caused by  $\sigma_r$  in Figure (5–7).

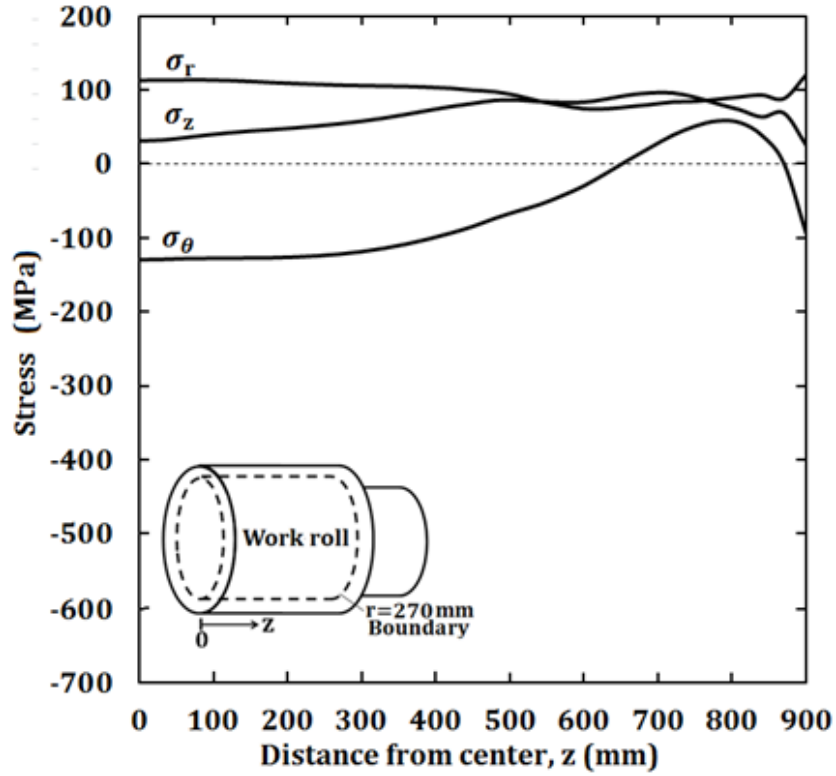


Figure (5-7): The generated residual stresses  $\sigma_r, \sigma_\theta$ , and  $\sigma_z$  at the boundary  $r = 270$  mm after heating, quenching, and tempering treatment in Figure (5-6)

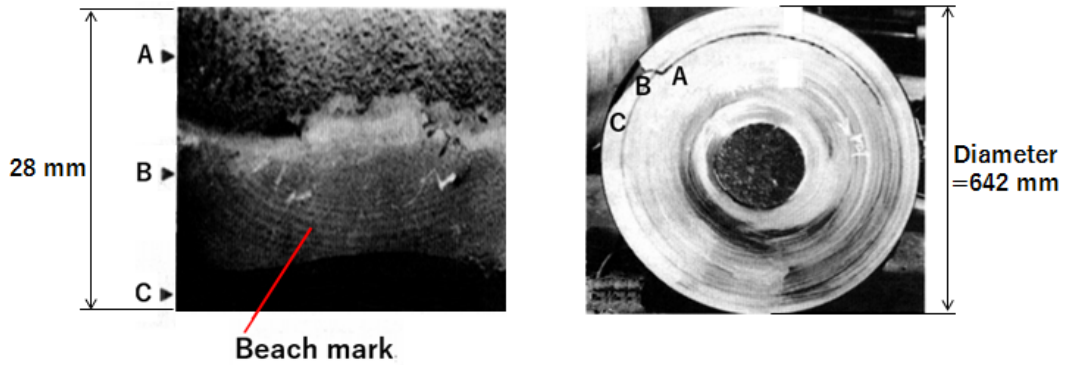


Figure (5-8): Failure at HSS/DCI boundary in bimetallic work roll (a) Fractured surface; A: Near boundary, B: Beach mark in shell, C: Roll surface, (b) Cross-section view of spalling crack

#### 5.4 Rolling stress generated in the bimetallic work roll obtained by the consecutive FEM analysis

In this section, the rolling stress is discussed when the bimetallic work roll with the residual stress in Section 5.3 is used in the four-high rolling mill as shown in Figure

## 5. Actual stress and fatigue failure during consecutive rolling analysis

(5–1). Considering the boundary debonding previously reported as well as the roll center fracture, the risk of fatigue failure is evaluated at those critical points. In this evaluation, the repeated maximum and minimum values of  $\sigma_r$  appearing at each roll rotation should be considered as the driving force causing the internal fatigue failure [55].

To estimate the maximum stress amplitude  $\sigma_r$  controlling the internal fatigue failure, Figure (5–9) illustrates the several critical lines denoted by  $B_{0\sim 900}^{270} |_{\theta=-90^\circ}$ ,  $B_{0\sim 900}^{270} |_{\theta=90^\circ}$ ,  $B_{0\sim 900}^{270} |_{\theta=0^\circ}$ ,  $C_{0\sim 900}^0 |_{\theta=90^\circ}$  and  $C_{0\sim 900}^0 |_{\theta=0^\circ}$  assumed inside of the work roll. For example,  $B_{0\sim 900}^{270} |_{\theta=-90^\circ}$  denotes the line at  $r = 270$  mm,  $\theta = -90^\circ$ ,  $z = 0 \sim 900$  mm. The superscript 270 of  $B_{0\sim 900}^{270} |_{\theta=-90^\circ}$  represents the  $r$ -coordinate  $r = 270$  mm, and the subscript  $0 \sim 900$  of  $B_{0\sim 900}^{270} |_{\theta=-90^\circ}$  represents the  $z$ -coordinate  $z = 0 \sim 900$  mm. As mentioned in Table 1,  $p_B(z)$  denotes the line force applied to the work roll from the backup roll, and  $p_S^{ave}$  denotes the line force applied to the work roll from the rolled steel.

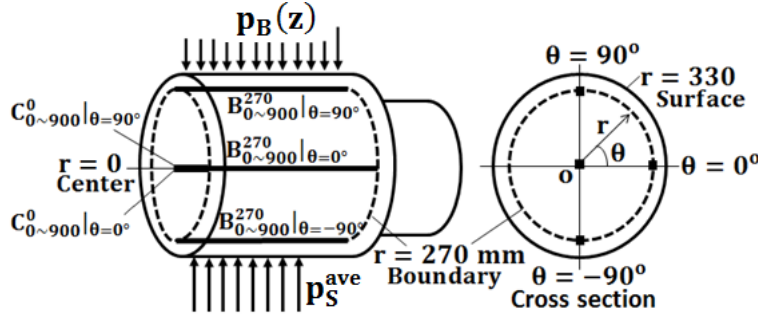


Figure (5–9): Critical position caused by the variation of  $\sigma_r$  in the work roll

### 5.4.1 Rolling stress variation due to the contact of the rolled steel

To estimate the rolling stress variation due to the contact of the rolled steel from  $\theta = -90^\circ$ , Figure (5–10) illustrates the stress distributions  $\sigma_r$  along the  $z$ -direction denoted by  $B_{0\sim 900}^{270} |_{\theta=-90^\circ}$  and  $B_{0\sim 900}^{270} |_{\theta=0^\circ}$  on the boundary  $r=270$  mm. Note that the stress variation is largest between the angle  $-90^\circ \leq \theta \leq 0^\circ$ . This is because the maximum tensile stress  $\sigma_r$  appears at  $\theta = 0^\circ$  and the maximum compressive stress  $\sigma_r$  appears at  $\theta = -90^\circ$ . Since  $\sigma_r$  in Figure (5–7) is almost equal to  $\sigma_r$  in Figure (5–10), the rolling

## 5. Actual stress and fatigue failure during consecutive rolling analysis

stress  $\sigma_r \cong 0$  at  $\theta = 0^\circ$ . Figure (5–10) also shows the largest compressive stress appears in the range of  $0 \leq z \leq 600$  mm because the rolled steel width is 600 mm. In Figure (5–10), the stress amplitude is considered in the region  $0 \leq z \leq 600$  mm. Then, it is found that the maximum stress amplitude appears at  $(r,z)=(270,0)$  where the maximum tensile stress  $\sigma_{r_{max}}^{\theta=0^\circ} = 115$  MPa, the maximum compressive stress  $\sigma_{r_{min}}^{\theta=-90^\circ} = -347$  MPa, and maximum stress amplitude  $\sigma_a^{max} = \sigma_{r_{max}}^{\theta=0^\circ} - \sigma_{r_{min}}^{\theta=-90^\circ} = 462$  MPa. This maximum stress amplitude at  $(r,z)=(270 \text{ mm}, 0)$  is denoted by  $B_0^{270} |_{\text{Rolled steel}}$  to discuss the fatigue failure.

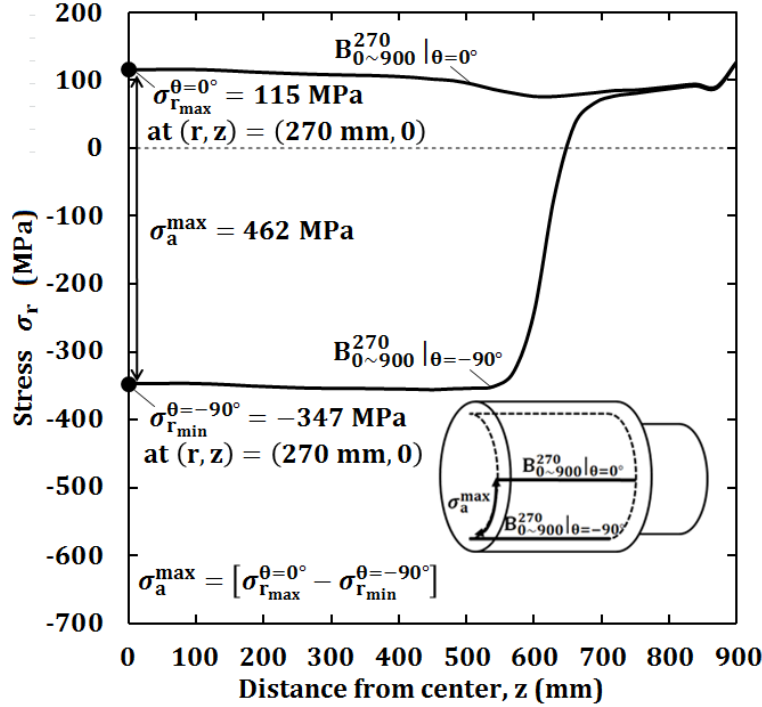


Figure (5–10): Variation of the stress distribution  $\sigma_r$  at the boundary  $r = 270$  mm due to the contact of the rolled steel from  $\theta = -90^\circ$

### 5.4.2 Rolling stress variation due to the contact of the backup roll

To estimate the rolling stress variation due to the contact of the backup roll from  $\theta = 90^\circ$ , Figure (5–11) illustrates the stress distributions  $\sigma_r$  denoted by  $B_{0 \sim 900}^{270} |_{\theta=-90^\circ}$  and  $B_{0 \sim 900}^{270} |_{\theta=0^\circ}$  along the  $z$ -direction on the boundary  $r = 270$  mm. The stress variation

## 5. Actual stress and fatigue failure during consecutive rolling analysis

is largest between the angle  $0 \leq \theta \leq -90^\circ$ . In Figure (5–11), the stress amplitude is considered in the region  $0 \leq z \leq 810$  mm. Then, it is found that the maximum stress amplitude appears at  $(r, z) = (270 \text{ mm}, 750 \text{ mm})$  from the tensile stress  $\sigma_{r_{max}}^{\theta=0^\circ} = 86 \text{ MPa}$  and the compressive stress  $\sigma_{r_{min}}^{\theta=-90^\circ} = -265 \text{ MPa}$ . The maximum stress amplitude  $\sigma_a^{max} = \sigma_{r_{max}}^{\theta=0^\circ} - \sigma_{r_{min}}^{\theta=90^\circ} = 351 \text{ MPa}$  at  $(r, z) = (270 \text{ mm}, 750 \text{ mm})$  is denoted by  $B_{750}^{270} |_{Backup \text{ roll}}$  to discuss the fatigue failure.

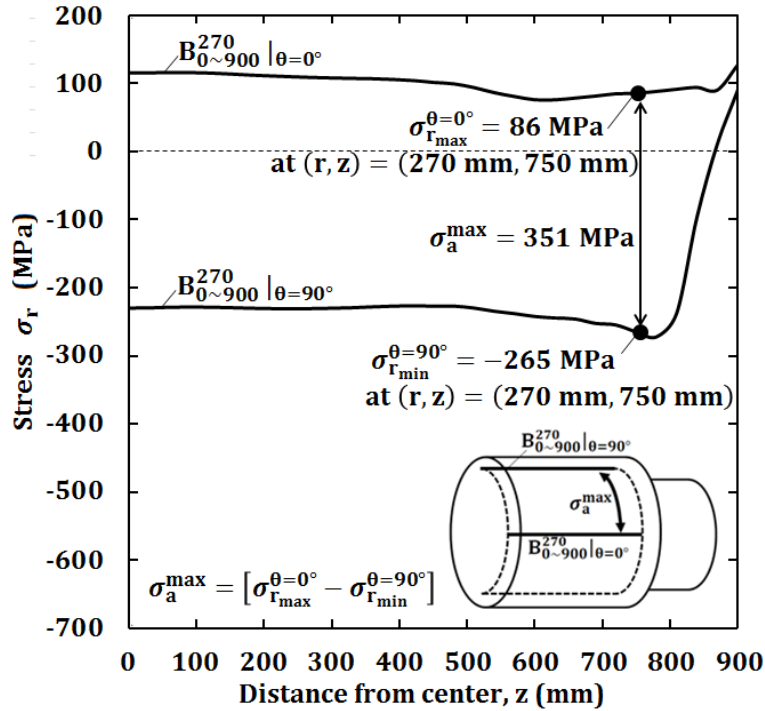


Figure (5–11): Variation of the stress distribution  $\sigma_r$  at the boundary  $r = 270$  mm due to the contact of the backup roll from  $\theta = 90^\circ$

### 5.4.3 Rolling stress variation at the roll center

Next, to evaluate the risk of the roll center fracture, Figure (5–12) illustrates the stress distributions denoted by  $C_{0~900}^0 |_{\theta=90^\circ}$  and  $C_{0~900}^0 |_{\theta=0^\circ}$  at the roll center at  $r = 0$ . The maximum stress amplitude  $\sigma_r$  can be seen at  $z = 0$  from the maximum tensile stress is  $\sigma_{r_{max}}^{\theta=90^\circ} = 169 \text{ MPa}$  and the minimum tensile stress  $\sigma_{r_{min}}^{\theta=0^\circ} = 35 \text{ MPa}$ . The maximum stress amplitude  $\sigma_a^{max} = \sigma_{r_{max}}^{\theta=90^\circ} - \sigma_{r_{min}}^{\theta=0^\circ} = 134 \text{ MPa}$  at  $(r, z) = (0, 0)$  is denoted by  $C_0^0$  to discuss

the fatigue failure.

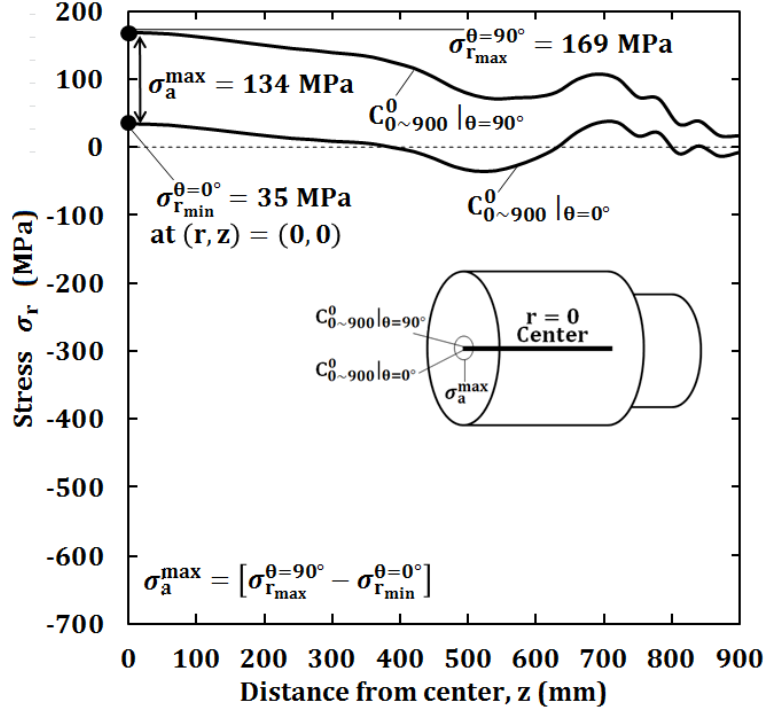


Figure (5-12): Variation of the stress distribution  $\sigma_r$  at the roll center at  $r = 0$  due to the contact of the rolled steel and the backup roll

### 5.5 Fatigue risk evaluation for three critical points

Figure (5-13) illustrates three critical points  $B_0^{270} |_{\text{Rolled steel}}$ ,  $B_{750}^{270} |_{\text{Backup roll}}$  and  $C_0^0$  as shown in Figure (5-10), Figure (5-11), Figure (5-12). Table (5-4) summarizes the maximum stress, the minimum stress, the mean stress, and the stress amplitude at those three critical points during the roll rotation. Among them,  $B_0^{270} |_{\text{Rolled steel}}$  and  $B_{750}^{270} |_{\text{Backup roll}}$  are subjected to quite large alternative compressive stress.

For large compressive alternative loading, the fatigue limit is determined in the previous chapter from Eq. (4-8) to Eq. (4-11), which is expressed by the thick solid lines passing through points A, D, F, G, H in Figure (5-14). Figure (5-14) shows the evaluation of the three critical points' results  $B_0^{270} |_{\text{Rolled steel}}$ ,  $B_{750}^{270} |_{\text{Backup roll}}$  and  $C_0^0$ .

Table (5-5) shows the safety factor defined as  $SF = \overline{OB'} / \overline{OB}$ . A larger SF value means

## 5. Actual stress and fatigue failure during consecutive rolling analysis

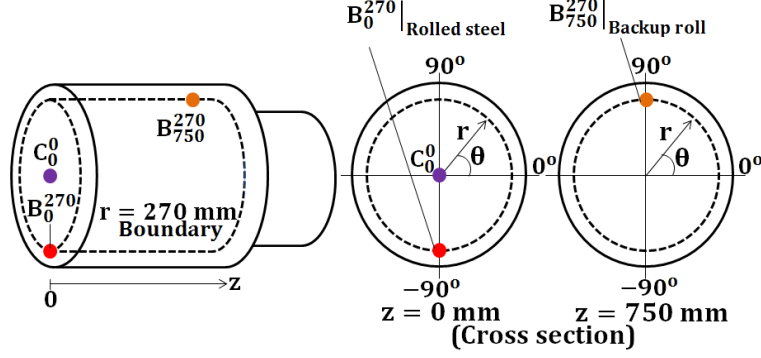


Figure (5-13): Illustration of three critical points denoted by  $B_0^{270} |_{Rolled\ steel}$ ,  $B_{750}^{270} |_{Backup\ roll}$  and  $C_0^0$  where fatigue risk should be evaluated based on the analysis and experience

Table (5-4): Maximum stress, minimum stress, mean stress, and stress amplitude at three critical points

Point	$\sigma_{r_{max}}$	$\sigma_{r_{min}}$	$\sigma_m$	$\sigma_a$
$B_0^{270}  _{Rolled\ steel}$	115	-347	-116	231
$B_{750}^{270}  _{Backup\ roll}$	86	-265	-90	176
$C_0^0$	169	35	102	67

the point is relatively safer than another point having a smaller SF value. Therefore, the safety factor SF can be used to evaluate the risk of fatigue failure relatively. Although the safety factor  $SF \geq 1$ ,  $B_0^{270} |_{Rolled\ steel}$  is relatively more dangerous than  $B_{750}^{270} |_{Backup\ roll}$  and  $C_0^0$ . The results showed that the fatigue crack initiation around points  $B_0^{270}$  on the HSS/DCI boundary may contribute to several roll failures previously occurred.

Table (5-5): Safety factor defined as  $SF = \overline{OB'}/\overline{OB}$  for three critical points by applying the consecutive FEM analysis

Point	Safety factor, SF
$B_0^{270}  _{Rolled\ steel}$	1.09
$B_{750}^{270}  _{Backup\ roll}$	1.43
$C_0^0$	1.55



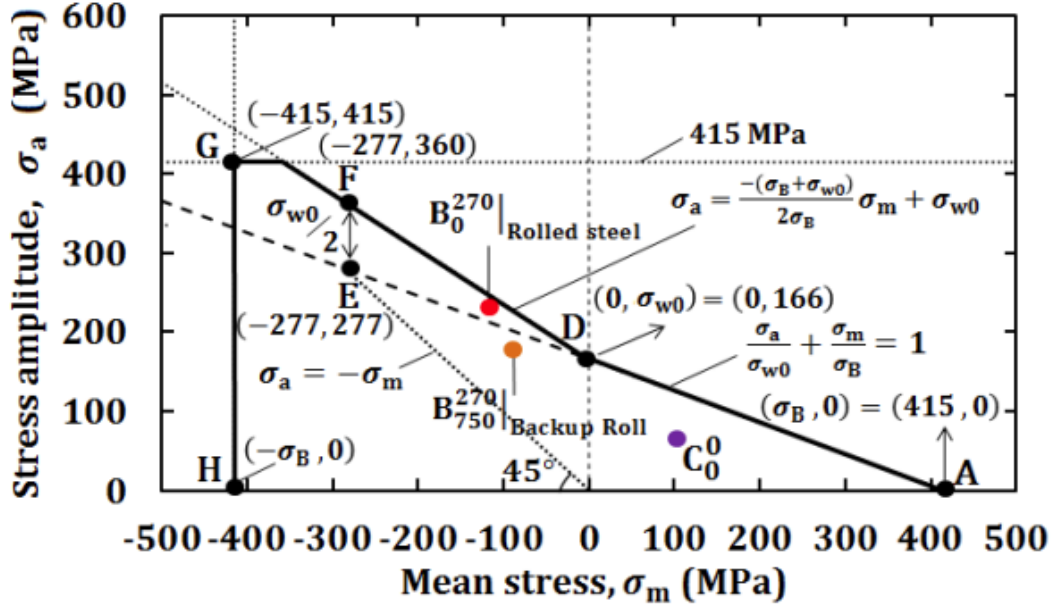


Figure (5-14): Stress amplitude versus mean stress diagram to evaluate the fatigue failure at three critical points

Although  $C_0^0$  is relatively safer, material defects often observed at the roll center are not taken into account in Figure (5-14). Hidaka et al. evaluated the maximum defect size by using statistics of extremes in the DCI specimens and confirmed that the lowest fatigue limit of DCI joints is larger than welded joints [56] [57]. To evaluate the fatigue failure risk at the roll center point  $C_0^0$  more accurately, in this study, the following formula is applied [58].

$$\sigma_{w0} = \frac{1.56(H_V + 120)}{\sqrt{area}^{1/6}} \quad (5-4)$$

Here,  $\sigma_{w0}$  is in MPa and is the fatigue limit under fully reversed loading of a material containing a defect;  $H_V$  is in  $\text{kgf/mm}^2$  and is the Vickers hardness number; and  $\sqrt{area}$  is in  $\mu\text{m}$  and is the square root of defect/crack area projected normal to the maximum principal stress. Figure (5-15) illustrates the fatigue limit  $\sigma_{w0}$  when the spheroidal defect diameter  $2a=0,5000, 10000 \mu\text{m}$  is assumed through  $\sqrt{area} = \sqrt{\pi a^2}$ . Here, the defect size 5 mm ( $=5000 \mu\text{m}$ ) is empirically known for the roll maker companies, and for the safety

## 5. Actual stress and fatigue failure during consecutive rolling analysis

reason, 10 mm (=10000  $\mu\text{m}$ ) defect size is also considered. Figure (5–15) shows that the fatigue limit  $\sigma_{w0}$  decreases from  $\sigma_{w0} = 166 \text{ MPa}$  to  $\sigma_{w0} = 87 \text{ MPa}$  when the defect diameter is changed from  $2a = 0$  to  $2a = 5000 \mu\text{m}$ . When  $2a=10000 \mu\text{m}$ , the fatigue limit  $\sigma_{w0}$  decreases to  $\sigma_{w0} = 78 \text{ MPa}$ . Table (5-6) shows that the safety factor SF decreases with increasing the defect size. Figure (5–15) shows that the point  $C_0^0$  becomes dangerous depending on the defect dimensions. If the defect size is 5 mm, the risk of fatigue failure at the point  $C_0^0$  is larger than the point  $C_0^0$  without defect in Table (5-6).

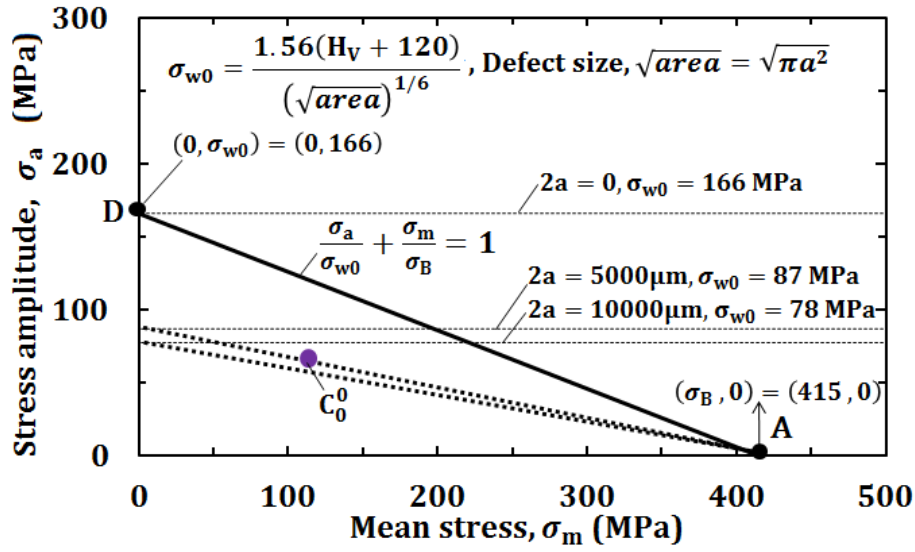


Figure (5–15): Stress amplitude versus mean stress diagram to evaluate the fatigue failure at point  $C_0^0$  when the spheroidal defect diameter  $2a = 0,5000, 10000 \mu\text{m}$  is assumed through  $\sqrt{area} = \sqrt{\pi a^2}$

Table (5-6): Safety factor defined as  $SF = \overline{OB'}/\overline{OB}$  at center point  $C_0^0$  when the spheroidal defect diameter  $2a = 0,5000, 10000 \mu\text{m}$  is assumed through  $\sqrt{area} = \sqrt{\pi a^2}$

Diameter change ( $\mu\text{m}$ )	Safety factor, SF
$2a=0$	1.55
$2a=5000$	0.98
$2a=10000$	0.91

## 5.6 Rolling stress estimation by superposing the residual stress and the rolling stress

As shown in Figure (5–16)a, in this study, the consecutive analysis is performed from the residual stress to the rolling stress to evaluate the fatigue failure risk. Then, the critical points  $B_0^{270} |_{\text{Rolled steel}}$ ,  $B_{750}^{270} |_{\text{Backup roll}}$  and  $C_0^0$  are considered on the  $\sigma_a$ - $\sigma_m$  diagram. However, in the real roll rotation, the results of  $\sigma_a$  and  $\sigma_m$  may change because the plastic stress varies depending on the loading history. Since another consecutive analysis has to be done every roll rotation, lots of calculation is necessary to clarify the differences. Therefore, in this section, a simple evaluation method is considered. Figure (5–16)b illustrates the method of superposition, which simply superposing the residual stress and the rolling stress.

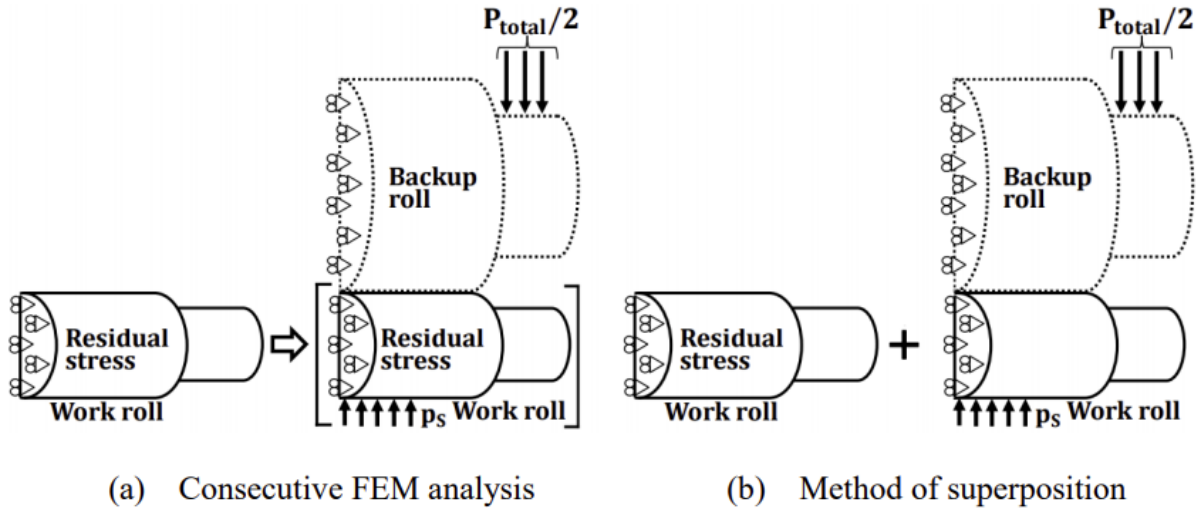


Figure (5–16): Comparison between two different methods of the rolling stress; (a) Consecutive FEM analysis, (b) Method of superposition

Figure (5–17) shows the stress amplitude versus mean stress diagram for the three critical points obtained by simply superposing the residual stress and the rolling stress as shown in Figure (5–16)b. Table (5-7) compares the safety factor SF obtained by the superposition with the results of the previous consecutive FEM analysis. As shown in Table (5-7), the SF of the superposition is smaller than the SF of the consecutive analysis.

## 5. Actual stress and fatigue failure during consecutive rolling analysis

In other words, the superposition method may evaluate the risk of failure in a safer way because the FEM consecutive results in Figure (5–16)a are safer than the results of the superposition in Figure (5–16)b. It may be concluded that we can estimate the rolling stress by simply superposing the results.

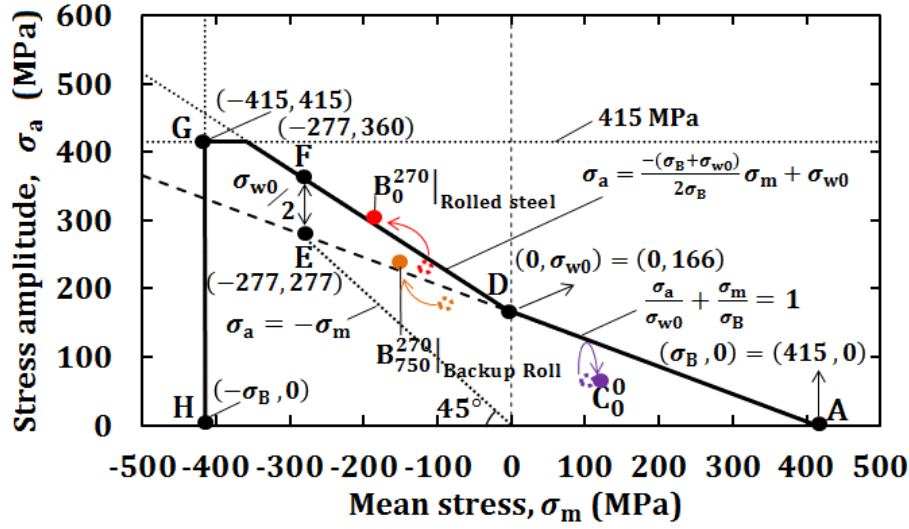


Figure (5–17): Stress amplitude versus mean stress diagram to evaluate the fatigue failure at three critical points denoted by the coloured solid circles obtained by superposing the residual stress and the rolling stress in comparison with the dotted circle obtained by the consecutive FEM

Table (5-7): Comparison of safety factor for both methods in Figure (5–16) at three critical points

Point	By consecutive FEM analysis	By superposition
$B_0^{270}$   <i>Rolled steel</i>	1.09	> 0.95
$B_{750}^{270}$   <i>Backup roll</i>	1.43	> 1.27
$C_0^0$	1.55	> 1.49

### 5.7 Conclusion

In this study, the three-dimensional elastic-plastic contact FEM is applied to calculate the rolling stress generated in bimetallic work roll during rolling in a four-high rolling mill. The initial residual stress was considered and the consecutive analysis was performed to evaluate the risk of fatigue failure. The conclusions obtained can be summarized in the following way.

1. The consecutive FEM analysis for quenching-tempering-rolling was performed to evaluate the risk of fatigue failure. By focusing on three critical points based on the analysis and experience, it may be concluded that the most critical point is located at the HSS/DCI boundary point  $B_0^{270}$  where  $(r, z)=(270 \text{ mm}, 0)$  because of the rolling steel caused the largest amplitude. Another critical point is also located at  $B_{750}^{270}$  where  $(r, z)=(270 \text{ mm}, 750 \text{ mm})$  because of the backup roll contact.
2. By using the relative safety factor SF, the fatigue failure risk was discussed. The results showed that the fatigue crack initiation around points  $B_0^{270}$  and  $B_{750}^{270}$  on the HSS/DCI boundary may contribute to several roll failures previously occurred.
3. Since the consecutive FEM analysis considering each roll rotation is time-consuming, the simple evaluation method was discussed by superposing the residual stress and the rolling stress. The results showed that the superposition method may evaluate the risk of failure in a safer way because the FEM consecutive results are safer than the results of the superposition.
4. The results showed that the superposition method may evaluate the risk of failure in a safer way because the FEM consecutive results are safer than the results of the superposition. Also, we found that point  $C_0^0$  becomes dangerous depending on the defect dimensions. If the defect size is 5 mm, the risk of fatigue failure at the point  $C_0^0$  is larger than the point  $C_0^0$  without defect

## **6 Main Conclusion**

### **6.1 Conclusion for present study**

In this study, bimetallic roll consisting of high-speed steel (HSS) and ductile casting iron (DCI) was considered to clarify the HSS/DCI boundary failure. A three-dimensional finite element method was applied to investigate the residual stress and the rolling stress of the bimetallic work roll in the four-high rolling mill. The residual stress was analyzed by considering pre-heating, quenching, and tempering. By using the results as an initial condition, the rolling stress analysis was performed consecutively. Then, the fatigue failure risk was discussed focusing on several critical points subjected to the largest stress amplitude inside of the work roll. The accuracy of the simple superposition method was also discussed to evaluate the risk conveniently. The following conclusions based on each chapter can be summarized as follow.

Chapter 1 provided a brief introduction of the bimetallic work roll used in 4-high rolling mill. Also the previous studies on the development of the bimetallic work roll to replace the single material roll. The characteristics of the bimetallic work roll were also discussed. Then, the research problem, focusing on the failure of the HSS/DCI boundary due to the residual stress and the rolling stress are included.

Chapter 2 analyzed the residual stress distribution of the bimetallic work roll after completing heating and quenching treatment. The bimetallic roll model has a diameter of 660 mm using HSS outer layer and DCI inner layer. A thermo-elastic-plastic finite element simulation was performed by using MSC Marc 2012 to investigate the residual stress during the quenching process. Uniform and non-uniform heating methods were considered to study the difference to the residual stress distribution. The conclusions are summarized as follows:

1. The tensile stress of the inner layer after non-uniform heating and quenching was less than that obtained after uniform heating and quenching by 24%, while the com-

## 6. Main Conclusion

---

pressive stress on the surface for both heating treatments did not differ greatly. As a result, the effect of preventing surface cracking can be expected to reduce damage originating from the center.

2. Based on the stress generation mechanisms, it was found that the stress in the central part decreased by non-uniform heating because during pearlite transformation B, the increase in the central stress in non-uniform heating (Ⓟ) was small. Similarly, the increase in the central stress (Ⓣ) in non-uniform heating is also small in region C after the pearlite transformation.
3. Based on the diameter effect result, the center tensile stress for non-uniform heating was smaller compared to that for uniform heating. Furthermore, the surface compressive stress varied significantly as the diameter changes from 500 mm to 1000 mm.
4. The results of the area ratio effect showed that the center tensile stress almost unchanged as the diameter changes from 500 mm to 1000 mm for uniform heating. For non-uniform heating, the center tensile stress changed when the area ratio changed. The surface compressive stress varies significantly as the roll diameter changes from 500 mm to 600 mm.

In chapter 3, the tempering treatment of the bimetallic roll is analyzed by considering the creep effect and transformation effect. The bimetallic roll model has a diameter of 660 mm using HSS outer layer and DCI inner layer. The analysis is performed to two tempering processes by using the thermal elasto-plastic finite element method, and the effect on the residual stress distribution is considered. The conclusions obtained are shown below.

1. It may be concluded that tempering treatment is useful in reducing the risk of roll failure by decreasing the center tensile stress without decreasing the surface compressive stress.
2. For uniform heating quenching, the maximum stress at the center decreased by 35% from 397 MPa to 257 MPa after the first tempering. The second tempering reduced

## 6. Main Conclusion

---

- the maximum stress by 54% from 397 MPa to 183 MPa.
3. For non-uniform heating quenching, the maximum stress decreased by 25% from 286 MPa to 214 MPa after the first tempering. The second tempering reduced the maximum stress by 46% from 286 MPa to 183 MPa.
  4. It is found that in this tempering process, the residual stress inside the roll is reduced by stress relaxation due to the creep effect.

In Chapter 4, to clarify the mechanical stress, no residual stress was assumed in the work roll. This study assumed the following rolling conditions that can be regarded as the average values in present steelworks, where the work roll diameter  $D_W = 660$  mm with the length  $L = 1800$  mm, the high chrome steel backup roll diameter of  $D_B = 1400$  mm with the length  $L = 1800$  mm, the width of the rolled steel  $W = 1200$  mm and the standard rolling force  $P_{total} = 16400$  kN. The conclusions obtained can be summarized in the following way.

1. No study is available regarding the fatigue limit under compressive mean stress region, stress amplitude versus mean stress diagram is newly considered. Then, a fatigue limit line was proposed under large compressive stress by considering the final failure never occurs at the pulsating compressive loading state.
2. Considering the whole roll geometry, three critical points were chosen on the basis of the analysis and experience. It may be concluded that the most critical point is located at the HSS/DCI boundary point  $B_0^{270}$  where  $(r, z) = (270 \text{ mm}, 0)$  because the largest stress amplitude is caused from the rolling steel. Another critical point is located at  $B_{750}^{270}$  where  $(r, z) = (270 \text{ mm}, 750 \text{ mm})$  due to the backup roll contact.
3. The fatigue failure risk was discussed through the relative safety factor SF. The results showed that the fatigue crack initiation around points  $B_0^{270}$  and  $B_{750}^{270}$  on the HSS/DCI boundary may contribute to several roll failures previously occurred in industries.



## 6. Main Conclusion

---

In Chapter 5, the three-dimensional elastic-plastic contact FEM was applied to calculate the rolling stress generated in bimetallic work roll during rolling in a four-high rolling mill. The initial residual stress was considered and the consecutive analysis was performed to evaluate the risk of fatigue failure. The conclusions obtained can be summarized in the following way.

1. The consecutive FEM analysis for quenching-tempering-rolling was performed to evaluate the risk of fatigue failure. By focusing on three critical points based on the analysis and experience, it may be concluded that the most critical point is located at the HSS/DCI boundary point  $B_0^{270}$  where  $(r, z)=(270 \text{ mm}, 0)$  because of the rolling steel caused the largest amplitude. Another critical point is also located at  $B_{750}^{270}$  where  $(r, z)=(270 \text{ mm}, 750 \text{ mm})$  because of the backup roll contact.
2. By using the relative safety factor SF, the fatigue failure risk was discussed. The results showed that the fatigue crack initiation around points  $B_0^{270}$  and  $B_{750}^{270}$  on the HSS/DCI boundary may contribute to several roll failures previously occurred.
3. Since the consecutive FEM analysis considering each roll rotation is time-consuming, the simple evaluation method was discussed by superposing the residual stress and the rolling stress. The results showed that the superposition method may evaluate the risk of failure in a safer way because the FEM consecutive results in Figure 16(a) are safer than the results of the superposition in Figure 16(b).
4. The results showed that the superposition method may evaluate the risk of failure in a safer way because the FEM consecutive results are safer than the results of the superposition. Also, we found that point  $C_0^0$  becomes dangerous depending on the defect dimensions. If the defect size is 5 mm, the risk of fatigue failure at the point  $C_0^0$  is larger than the point  $C_0^0$  without defect

### 6.2 Future work

In the present study, the bimetallic work roll is considered to study the fatigue failure risk under combination of residual stress and the rolling stress. In future, the effect of the roll manufacturing processes will be clarified to investigate the residual stress.

The roll manufacturing process can be seen in Appendix 3. The first method is to drill the roll center of the solid roll after heat treatment. The second method is to drill the center first before heat treatment of the solid roll. By applying FEM, the residual stresses of sleeve rolls are compared to find out the suitable manufacturing method.

## Acknowledgement

Alhamdulillah. My sincere gratitude to my late father, my mother, my lovely wife, my good son, and to all my family members for their great continuous support, time, and encouragement more than I need throughout my years of this Ph.D. study.

I would like to thank my supervisor Professor Nao-Aki Noda for his valuable guidance and advice throughout my study. Without his consistent guidance, this study could not have reached its present form.

Also, I would also like to appreciate Dr. Yoshikazu Sano, my project advisor for his great advice for almost over the last four years. I would also to thank the laboratory technical staff, Dr. Yasushi Takase, for his help and advice concerning the experimental simulations and facilitating the mathematical computations.

Many thanks to the contributions and insightful observations of my committee members, Prof. Kenji Matsuda, Prof. Yasuhiro Akahoshi, Prof. Tsuboi, and Prof. Yamada.

Particular thanks are due to Dr. Anuaruddin, Dr. Siti, Dr. Hiromasa Sakai, Dr. Chen Dong, Dr. Wang Biao, Rei Takaki, Rahimah, Kenji Tsuboi, Kakeru Takata, Torigue, and Akane Inoue for their valuable discussions, support and friendship. Thank you to all lab mates of Elasticity and Fracture Laboratory, and all those who have helped me carry out my work.

Also, special thanks to Keiko Matsuoka Sensei for her help throughout our stay in Japan.

Many thanks are due to the technical staff of the postgraduate and student office including the Departments of Mechanical Engineering, Kyushu Institute of Technology for their support during my study.

Lastly, I would also like to gratefully acknowledge the Ministry of Education, Culture, Sports, Science and Technology of Japan (MEXT) for the Monbukagakusho scholarship, which made it possible for my study and stays in Japan with my family.

## References

- [1] Y. Sano, T. Hattori, and M. Haga, “Characteristics of High-carbon High Speed Steel Rolls for Hot Strip Mill,” *ISIJ International* **32**(11), 1194–1201 (1992).
- [2] K. H. Schroder, *Basic Understanding of the Mechanics of Rolling Mill Rolls* (Eisenwerk Sulzau-Werfen, ESW-Handbook, Tenneck, Austria, 2003).
- [3] K. Goto, Y. Matsuda, K. Sakamoto, and Y. Sugimoto, “Basic Characteristics and Microstructure of High-carbon High Speed Steel Rolls for Hot Rolling Mill,” *ISIJ International* **32**(11), 1184–1189 (1992).
- [4] J. H. Ryu and H. B. Ryu, “Effect of Thermal Fatigue Property of Hot Strip Mill Work Roll Materials on the Rolled-in Defects in the Ultra-low Carbon Steel Strips,” *ISIJ International* **43**(7), 1036–1039 (2003).
- [5] J. W. Park, H. C. Lee, and S. Lee, “Composition, microstructure, hardness, and wear properties of high-speed steel rolls,” *Metallurgical and Materials Transactions A* **30**, 399–409 (1999).
- [6] F. J. Belzunce, A. Zaidi, and C. Rodriguez, “Structural integrity of hot strip mill rolling rolls,” *Engineering Failure Analysis* **11**, 789–797 (2004).
- [7] M. Shimizu, O. Shitamura, S. Matsuo, T. Kamata, and Y. Kondo, “Development of High Performance New Composite Roll,” *ISIJ International* **32**, 1244–1249 (1992).
- [8] Y. L. Cao, Z. H. Jiang, Y. W. Dong, X. Deng, L. Medovar, and G. Stovpchenko, “Research on the Bimetallic Composite Roll Produced by an Improved Electrosag Cladding Method: Mathematical Simulation of the Power Supply Circuits,” *ISIJ International* **58**, 1052–1060 (2018).

## References

---

- [9] M. Hashimoto, T. Oda, K. Hokimoto, T. Kawakami, and R. Kurahashi, “Development and application of high-speed tool steel rolls in hot strip rolling,” Nippon Steel Technical Report **66**, 82–90 (1995).
- [10] M. Ooshima, Y. Sugimura, and Y. Sano, “The development of the new type high performance compound rolls for hot rolling,” 32nd Mechanical Working and Steel Processing **28**, 31–34 (1990).
- [11] H. Fu, Q. Xiao, and J. D. Xing, “A Study on the Crack Control of a High-Speed Steel Roll Fabricated by a Centrifugal Casting Technique,” Materials Science and Engineering: A **474**, 82–87 (2008).
- [12] Y. Sano, “Statistical Analysis about Crack and Spalling on Work Roll for Hot Strip Mill Finishing Rear Stands,” The 245th JSMS Committee on Fatigue of Materials and The 36th JSMS Committee on Strength Design • Safety Evaluation, The Society of Materials Science, Kyoto **40**, 1–10 (1999).
- [13] H. Kejun, “Study on Residual Stress for Hot Strip Rolling Bimetallic Rolls during the Heat Treatment Process,” Ph.D. Thesis, Kyushu Institute of Technology (2017).
- [14] Y. Sekimoto, Transaction of Iron Steel Institute of Japan **10**, 341–349 (1970).
- [15] C. M. Park, W. S. Kim, and G. J. Park, “Thermal analysis of the roll in the strip casting process,” Mechanics Research Communications **30**, 297–310 (2009).
- [16] N. A. Noda, K. Hu, Y. Sano, Y. Hosokawa, and X. Wang, “Accuracy of Disk Method to Predict Roll Residual Stress by Measuring the Sliced Disk Stress,” ISIJ International **8**, 1432–1440 (2017).
- [17] N. V. Konstantin, A. D. Gennady, and G. E. Lyudmila, “Technology of Heat Treatment of Mill Rolls,” Transaction of Iron Steel Institute of Japan **54**, 233–238 (2019).

## References

---

- [18] N. A. Noda, Y. Sano, M. R. Aridi, K. Tsuboi, and N. Oda, “Residual Stress Differences between Uniform and Non-Uniform Heating Treatment of Bimetallic Roll:Effect of Creep Behavior on Residual Stress,” *Metals* **8**, 1–10 (2018).
- [19] Y. Z. Yin and Y. C. Wang, “Numerical Solutions of the Effects of of Non-uniform Temperature Distributions on Lateral Torsional Buckling Resistance of Steel I-Beams,” *Journal of Constructional Steel Research* **59**, 1009–1033 (2003).
- [20] C. S. Li, H. L. Yu, G. Y. Deng, X. H. Liu, and G. D. Wang, “Numerical Simulation of Temperature Field and Thermal Stress Field of Work Roll During Hot Strip Rolling,” *Journal of Iron and Steel Research International* **14**, 18–21 (2007).
- [21] D. Benasciutti, E. Brusa, and G. Bazzaro, “Finite elements prediction of thermal stresses in work roll of hot rolling mills,” *Procedia Engineering* **2**, 707–,716 (2010).
- [22] K. Sakai, “Calculation of thermal stress in cylindrical steel during cooling,” *Tetsu to Hagane* **60**, 1591–1,598 (1974).
- [23] T. Inoue, K. Haraguchi, and S. Kimura, “Stress analysis during quenching and tempering,” *Journal of the Society of Materials Science Japan* **25**, 521–526 (1976).
- [24] C. Acevedo and A. Nussbaumer, “Effect of tensile residual stresses on fatigue crack growth and S-N curves in tubular joints loaded in compression,” *International Journal of Fatigue* **36**, 171–180 (2012).
- [25] H. Fu, Y. Qu, J. Xing, X. Zhi, Z. Jiang, M. Li, and Y. Zhang, “Investigation on Heat Treatment of a High-Speed Steel Roll,” *Journal of Materials Engineering and Performance* **17**, 535–542 (2008).
- [26] Y. Sano, D. Chin, and E. Matsunaga, “Analysis of Propagation of Surface Cracks of Work Roll for Hot Strip,” *Transcation of JSME Part C* **58**, 248–253 (1992).

## References

---

- [27] M. Sedlacek, B. Podgornik, and S. Milanovic, “A Modified Heat Treatment to Improve the Properties of Double-Layer Act Rolls,” *Materials and Technology* **48**, 983–990 (2014).
- [28] N. A. Noda, K. Hu, Y. Sano, K. Ono, and Y. Hosokawa, “Residual Stress Simulation for Hot Strip Bimetallic Roll during Quenching,” *Steel Research International* **87**, 1478–1488 (2016).
- [29] N. A. Noda, K. Hu, Y. Sano, K. Ono, and Y. Hosokawa, “Usefulness of Non-Uniform Heating and Quenching Method for Residual Stress of Bimetallic Roll: FEM Simulation Considering Creep Behavior,” *Steel Research International* **88**, 1600,165 (2017).
- [30] J. Tanaka and T. Obata, “A Study on Stress Relief Heat Treatment (Report II),” *The Japan Welding Engineering Society* **36**, 222–228 (1967).
- [31] Y. Sano, D. Chin, and E. Matsunaga, “The Application of the Norton-Bailey Law for Creep Prediction Through Power Law Regression,” *Proceedings of ASME Turbo Expo 2013: Turbine Technical Conference and Exposition GT2013 June 3-7* **GT2013-96008**, 1–8 (2013).
- [32] JISZ2271, *Metallic Materials-Uniaxial Creep Testing in Tension-Method of Test* (Japanese Industrial Standards Committee, Tokyo, Japan, 2010).
- [33] Y. Sano and K. Kimura, “Statistical Analysis about Crack and Spalling on Work Roll for Hot Strip Mill Finishing Rear Stands,” *Tetsu to Hagane* **73**, 78–85 (1987).
- [34] Y. Sano, “鉄鋼・非鉄金属圧延加工用ロールの最近の技術,” 第93回塑性加工学講座「棒線形管の圧延中心とした塑性加工の基礎と応用」 pp. 199–213 (2004).
- [35] H. Sakai, N. A. Noda, Y. Sano, G. Zhang, and Y. Takase, “Effect of Driving Torque on the Interfacial Creep for Shrink-fitted Bimetallic Work Roll,” *Tetsu to Hagane* **105**, 1126–1134 (2019).

## References

---

- [36] T. I. S. I. of Japan, *Recent hot strip manufacturing technology in Japan* (The Iron and Steel Institute of Japan, Tokyo, Japan, 1987).
- [37] S. Hamada, Y. Sakoda, D. Sasaki, M. Ueda, and H. Noguchi, “Evaluation of fatigue limit characteristics of lamellar pearlitic steel in consideration of microstructure,” *Journal of the Society of Materials Science Japan* **60**, 790–795 (2011).
- [38] Y. Sekimoto, M. Tanaka, R. Sawada, and M. Koga, “熱間圧延ロールの材質と寿命,” *塑性と加工* **23**, 952–957 (1982).
- [39] Y. Sekimoto, M. Tanaka, R. Sawada, and M. Koga, “Effects of Rolling Condition on the Surface Temperature of Work Roll in Hot Strip Mill,” *Tetsu to Hagane* **61**, 2337–2349 (1975).
- [40] K. H. Schroder, “Heavy Spalls Originating in the Cores of High Chromium Rolls,” *Metallurgical Plant and Technology* **2**, 62–66 (1986).
- [41] H. Li, Z. Jiang, K. A. Tieu, and W. Sun, “Analysis of premature failure of work rolls in a cold strip plant,” *Wear* **263**, 1442–1446 (2007).
- [42] Q. Dong, J. G. Cao, H. B. Li, Y. S. Zhou, T. L. Yan, and W. Z. Wang, “Analysis of Spalling in Roughing Mill Backup Rolls of Wide and Thin Strip Hot Rolling Process,” *Steel Research International* **86**, 129–136 (2015).
- [43] G. Pantazopoulos and A. Vazdirvanidis, “Fractographic and metallographic study of spalling failure of steel straightener rolls,” *Journal of Failure Analysis and Prevention* **8**, 509–514 (2008).
- [44] K. L. Johnson, *Contact Mechanics* (Cambridge University Press, New York, 2003).
- [45] T. Sakai, B. Lian, M. Takeda, K. Shiozawa, N. Oguma, Y. Ochi, M. Nakajima, and T. Nakamura, “Statistical duplex S–N characteristics of high carbon chromium bearing steel in rotating bending in very high cycle regime,” *International Journal of Fatigue* **32**, 497–504 (2010).



## References

---

- [46] E. Zalnezhad, A. A. D. Sarhan, and P. Jahanshahi, “A new fretting fatigue testing machine design, utilizing rotating-bending principle approach,” *The International Journal of Advanced Manufacturing Technology* **70**, 2211–2,219 (2014).
- [47] H. Nisitani and N. Yamashita, “Effect of mean stress on initiation and growth of fatigue crack in 70/30 Brass,” *Transaction of JSME* **32**, 1456–1461 (1966).
- [48] H. Nisitani and M. Goto, “Effect of mean stress on initiation and initial growth of fatigue crack in tension compression fatigue of annealed S45C,” *Transaction of JSME Part A* **50**, 1926–1935 (1984).
- [49] Y. Akiniwa, K. Tanaka, and N. Taniguchi, “片振圧縮繰返し下における低炭素鋼切欠材での微小疲労き裂の伝ばと停留,” *日本機械学会論文集 A 編* **53**, 1768–1774 (1987).
- [50] A. Ince and G. Glinka, “A modification of Morrow and Smith–Watson–Topper mean stress correction models,” *Fatigue and Fracture of Engineering Materials and Structures* **34**, 854–867 (2011).
- [51] K. Kasaba, T. Sano, S. Kudo, T. Shoji, K. Katagiri, and T. Sato, “Fatigue crack growth under compressive loading,” *Journal of Nuclear Materials* **258-263**, 2059–2063 (1998).
- [52] Z. Y. Jiang, D. Wei, and A. K. Tieu, “Analysis of cold rolling of ultra thin strip,” *Journal of Materials Processing Technology* **209**, 4584–4589 (2009).
- [53] M. A. Tolcha, H. Altenbach, and G. S. Tibba, “Modeling fatigue crack and spalling for rolling die under hot milling,” *Fatigue and Fracture of Engineering Materials and Structures* **42**, 2611–2624 (2019).
- [54] Y. Ohkomori, C. Sakae, and Y. Murakami, “Analysis of Mode II Crack Growth Behavior in Spalling Failure of Backup Roll,” *Journal of the Society of Materials Science Japan* **50**, 249–254 (2001).

## References

---

- [55] T. Sakai, B. Lian, M. Takeda, K. Shiozawa, N. Oguma, Y. Ochi, M. Nakajima, and T. Nakamura, “Two simplified methods for fatigue crack growth prediction under compression-compression cyclic loading,” *Marine Structures* **58**, 367–381 (2018).
- [56] T. Hidaka, N. A. Noda, Y. Sano, N. Kai, and H. Fujimoto, “Fatigue Strength Improvement by Replacing Welded Joints with Ductile Cast Iron Joints,” *ISIJ International* **59**, 1860–1869 (2019).
- [57] T. Hidaka, N. A. Noda, Y. Sano, N. Kai, and H. Fujimoto, “Lowest Fatigue Limit Estimation of Ductile Cast Iron Joints by Considering Maximum Defect Size Toward Replacing Welded Joints,” *ISIJ International* **60**, 1006–1015 (2020).
- [58] Y. Murakami, *Metal Fatigue: Effect of small defects and nonmetallic inclusions* (Elsevier Science, Kidlington, Oxford, UK, 2002).

# A Appendix

## A.1 Effect of material data on the residual stress

Figure (A–1) shows the different material data in collaboration with JFE steel company where the material data shows the slightly different compare to Figure (2–3).

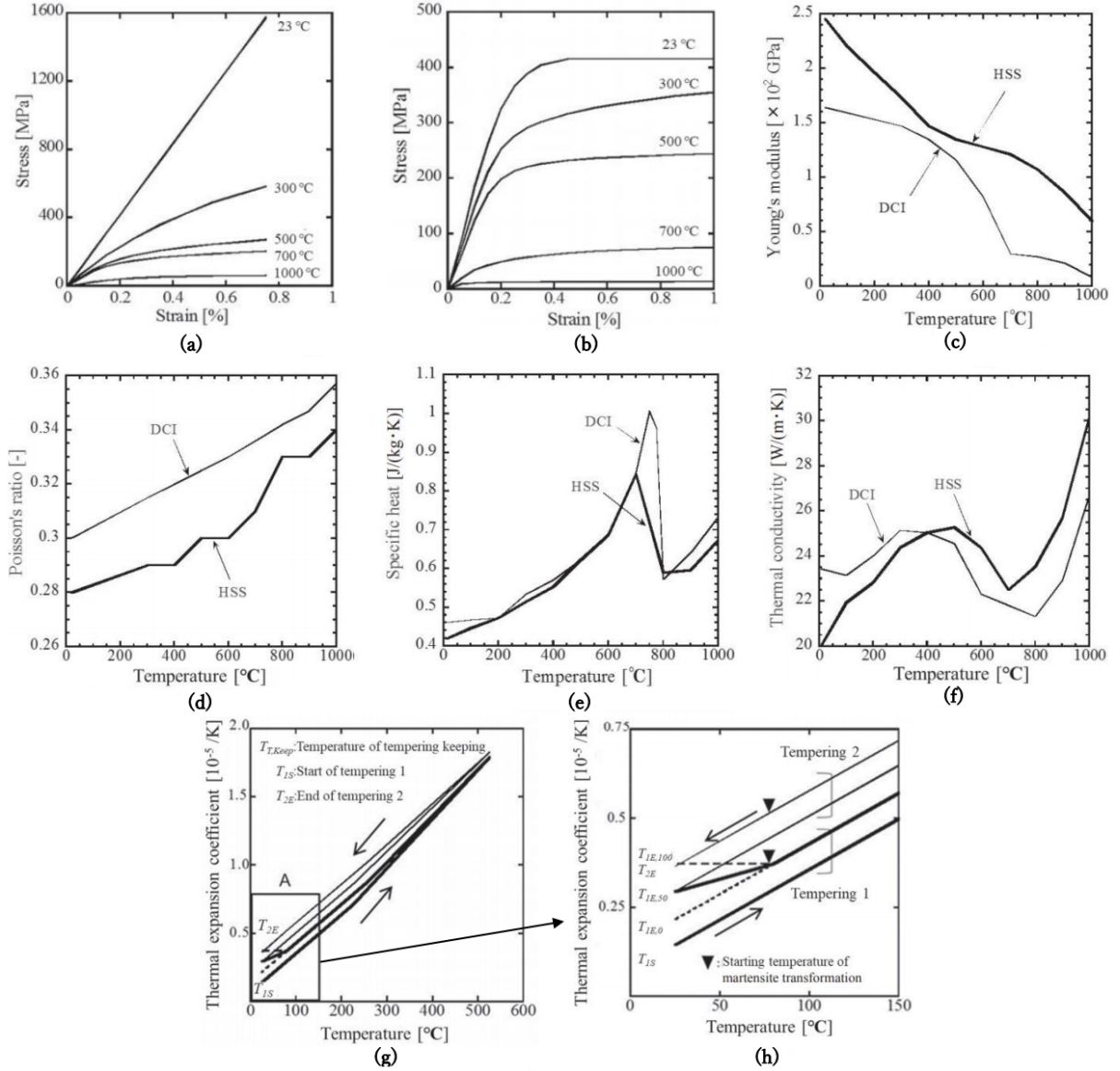


Figure (A–1): (a) Young's modulus; (b) specific heat; (c) thermal conductivity; (d) thermal expansion coefficient during quenching; (e) Poisson's ratio; (f) stress-strain for HSS; (g) stress-strain for DCI

This is because the collaboration research was focused on the transformation effect of

## A. Appendix

the outer layer HSS. Therefore, some material datas are slightly different.

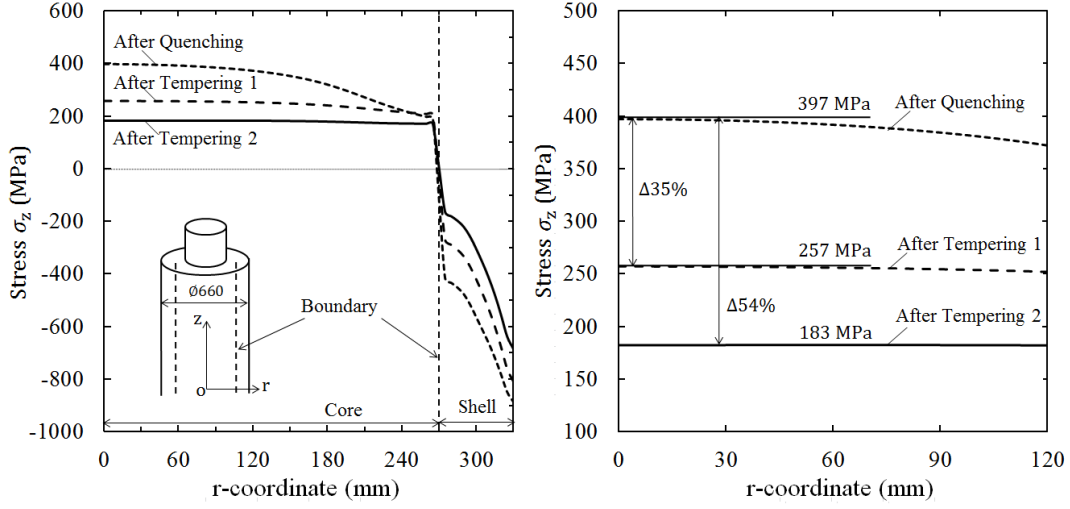


Figure (A-2): Results of residual stress based on Figure (3-3); (a) Residual stress  $\sigma_z$  after uniform heating quenching; (b) Details of maximum stress range

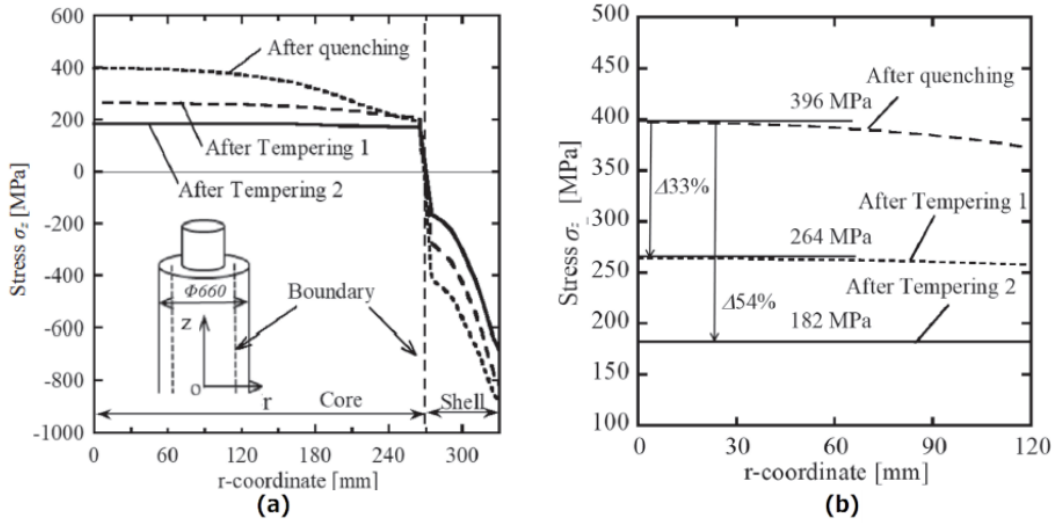


Figure (A-3): Results of residual stress based on the corrected material data; (a) Residual stress  $\sigma_z$  after uniform heating quenching; (b) Details of maximum stress range

In the quench analysis in Chapter 2, the material database J-MatPro (<https://www.usi-asia.com/jmatpro/>) was used to clarify the effects of the material properties. In this research, joint research is also in progress, and there was a proposal to slightly change the material properties. Therefore, in the tempering analysis in Chapter 3, the analysis

## A. Appendix

data was changed and the analysis was performed. For this uniform heating quenching, comparing Figure (A-2) and Figure (A-3), it was confirmed that the difference between the two was within 3% at the maximum, and almost the same results were obtained.

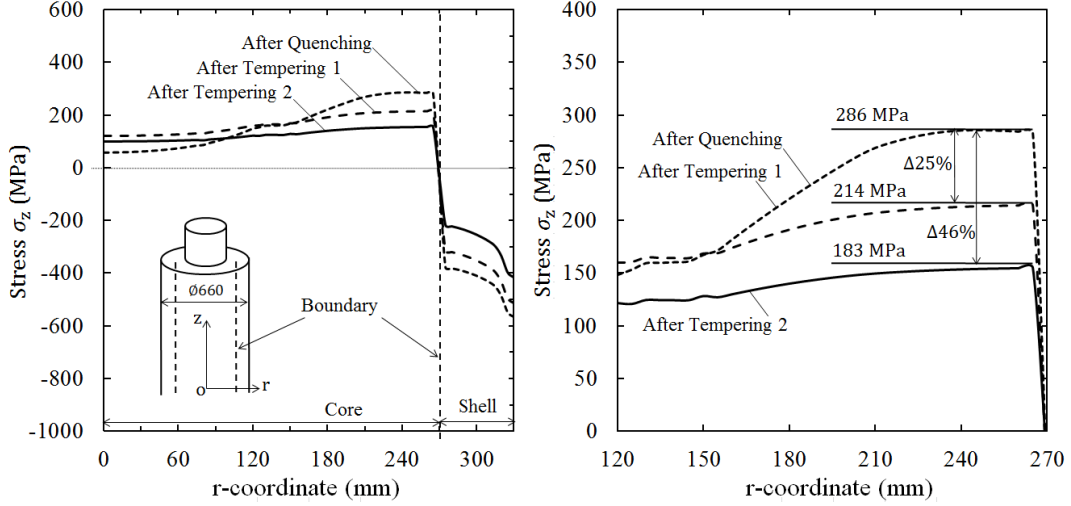


Figure (A-4): Results of residual stress based on Figure (3-4); (a) Residual stress  $\sigma_z$  after non-uniform heating quenching; (b) Details of maximum stress range

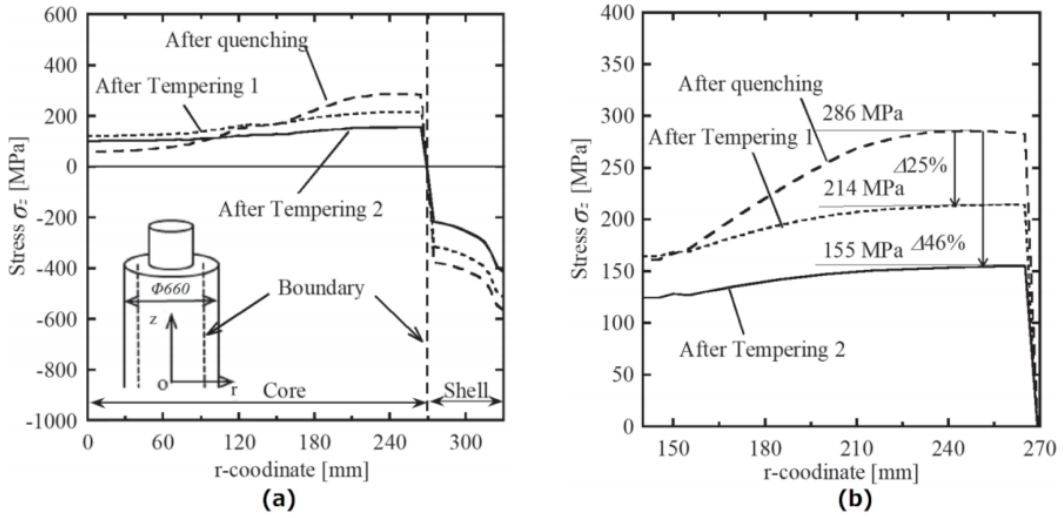


Figure (A-5): Results of residual stress based on the corrected material data; (a) Residual stress  $\sigma_z$  after non-uniform heating quenching; (b) Details of maximum stress range

For this non-uniform heating quenching, comparing Figure (A-4) and Figure (A-5), it was confirmed that the difference between the two was within 1% at the maximum, and

almost the same results were obtained.

## A.2 Stress reduction effect due to the transformation effect

The stress reduction effect in the tempering process is mainly affected by the transformation of the outer layer material and the creep effect of the inner layer material. Here, in order to evaluate the stress reduction effect due to creep alone, martensite during cooling in the first treatment of tempering after quenching is performed. The analysis was performed with the site transformation as 0%. Figure (A-6) shows the stress distribution diagram after quenching and after first tempering for both uniform and non-uniform heating.

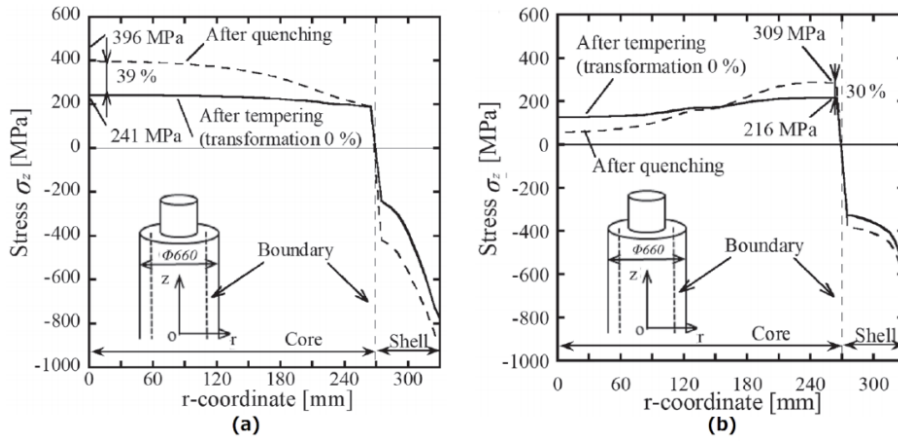


Figure (A-6): Effect of transformation during tempering process after uniform heating quenching

In uniform heating (Figure (A-6)a), the maximum stress point near the center decreased from 396 MPa to 241 MPa. On the other hand, a comparison between after quenching and after first tempering including creep and transformation of 50% showed that the stress decreased from 396 MPa to 217 MPa (see Figure (3-3)), indicating that the stress increased by 24 MPa ( $=241 \text{ MPa} - 217 \text{ MPa}$ ) due to transformation.

In non-uniform heating (Figure (A-6)b), the maximum stress point near the center decreased from 309 MPa to 216 MPa. On the other hand, a comparison between after

## A. Appendix

---

quenching and after first tempering including creep and transformation of 50% showed that the stress decreased from 309 MPa to 226 MPa (see Figure (3–4)), indicating that the stress decreased by 10 MPa ( $=226 \text{ MPa} - 216 \text{ MPa}$ ) due to transformation.

Table (A-1) summarizes the effects of creep and transformation on stress. Since the effect of transformation effect is small, it is important to consider the creep effects in the analysis.

Table (A-1): Stress reduction in tempering

	Creep + Transformation	Creep	Transformation
After Uniform heating	-45%	-39%	-6%
After non-uniform heating	-27%	-30%	+3%

### A.3 Effect of Manufacturing Process on Residual Stress in Bimetallic Solid Roll and Bimetallic Sleeve Roll

This future study aims to study the difference of the residual stress generated between the current bimetallic solid roll and the bimetallic sleeve roll constructed by shrink-fitting. Figure (A–7) shows the types of manufacturing process. Method 1 is turning inside of the solid roll after heat treatment. Method 2 is heat treatment after turning inside of the solid roll. The results show that Method 2 is better than Method 1 since the tensile residual stress can be reduced at the inside of the sleeve. After shrink- fitting of the shaft, the residual stress is compared with the one of the solid roll.

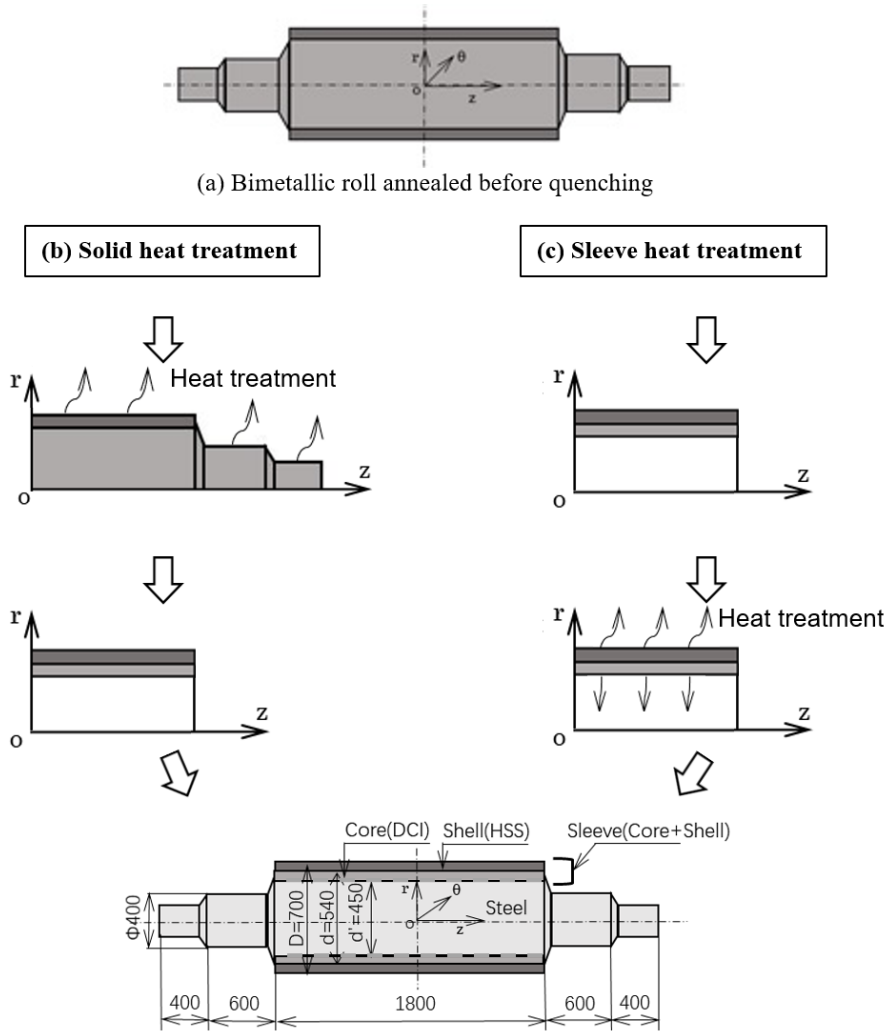


Figure (A-7): Bimetallic sleeve roll having shrink-fitted shaft manufactured by solid heat treatment and sleeve heat treatment



## **B List of publication**

1. Y. Sano, N.A. Noda, Y. Takase, R. Torigoe, Y. Sanada, K. Tsuboi, M.R. Aridi, L. Lan. Effect of Tempering Treatment Upon the Residual Stress of Bimetallic Roll. IOP Conference Series: Material Science and Engineering 2018; 372(No.012019): 1-6. <https://doi.org/10.1088/1757-899X/372/1/012019>
2. N.A. Noda, Y. Sano, M.R. Aridi, K. Tsuboi, N. Oda. Residual stress differences between uniform and non-uniform heating treatment of bimetallic roll: Effect of creep behavior on residual stress. Metals 2018; 8: 952. <https://doi.org/10.3390/met8110952>
3. N.A. Noda, M.R. Aridi, R. Torigoe, K. Tsuboi, Y. Sano. Reduction of residual stress in bimetallic work roll by tempering. Journal of the JSTP 2020; 61: 183-189. <https://doi.org/10.9773/sosei.61.183>
4. N.A. Noda, M.R. Aridi, Y. Sano. Tempering effect on residual stress in bimetallic roll. International Journal of Modern Physics B 2021; 35(14-16), 2140044. <https://doi.org/10.1142/S0217979221400440>
5. N.A. Noda, M.R. Aridi, R. Abdul Rafar, S. Zifeng, Y. Sano, K. Takata, Y. Takase. Effect of Manufacturing Process on Residual Stress in Bimetallic Solid Roll and Bimetallic Sleeve Roll. Journal of Japan Society for Design Engineering 2021. <https://doi.org/10.14953/jjsde.2021.2921>
6. M.R. Aridi, N.A. Noda, Y. Sano, K. Takata, S. Zifeng. Effect of the Residual Stress to the Fatigue Failure of the Bimetallic Work Roll in 4-High Rolling Mill. In: Parinov I.A., Chang S.H., Kim Y.H., Noda N.A. (eds) Physics and Mechanics of New Materials and Their Applications. PHENMA 2021. Springer Proceedings in Materials, vol 10. Springer, Cham pp 389-393. [https://doi.org/10.1007/978-3-030-76481-4\\_33](https://doi.org/10.1007/978-3-030-76481-4_33)
7. M.R. Aridi, N.A. Noda, Y. Sano, K. Takata, S. Zifeng. Fatigue Failure Analysis for Bimetallic Work Roll in Four-High Rolling Mill. Steel Research International 2022; 93(2), 2100313. <https://doi.org/10.1002/srin.202100313>
8. M.R. Aridi, N.A. Noda, Y. Sano, K. Takata, S. Zifeng. Fatigue failure risk evaluation

## B. List of publication

---

based on stress amplitude versus mean stress diagram under compressive stress field when bimetallic roll is used in 4-high rolling mill. *Fatigue & Fracture of Engineering Materials & Structures* 2022; 45(4), 1065-1087. <https://doi.org/10.1111/ffe.13651>

Conference paper:

1. A Study on Tempering Effect on the Residual Stress of Bimetallic Roll for Uniform and Non-Uniform Heating 日本材料学会九州支部第5回学術講演会, pp.5-6 (2018年12月)
2. Three-Dimensional Rolling Stress Analysis in Bimetallic Roll When the Work Roll is Used in Four-High Rolling Mill 日本材料学会九州支部第7回学術講演会, pp.25-26 (2020年11月)
3. Effect of the Residual Stress to the Fatigue Failure of the Bimetallic Work Roll in 4-High Rolling Mill. 2020 International Conference on "Physics and Mechanics of New Materials and Their Applications" (PHENMA 2020), March 26-29, 2021